INFRARED SPECTROSCOPY OF CONJUGATED ORGANIC MOLECULES UNDER HIGH PRESSURE

By

KIRILL KHAMIDOVICH ZHURAVLEV

A dissertation submitted in partial fulfillment
of the requirements for the degree of

Doctor of Philosophy

WASHINGTON STATE UNIVERSITY
Department of Physics

MAY 2004

To the Faculty of Washington State University:

The members of the Committee appointed to examine the dissertation of Kirill Khamidovich Zhuravlev find it satisfactory and recommend that it be accepted.

_____

Chair

_____

_____

Acknowledgements

I would like to thank my advisor, Dr. Matthew D. McCluskey, for suggesting this project and for his constant support and assistance through the course of this work. His help and guidance can not be overestimated. I would also like to thank Dr. Zbignew Dreger for his help with fluorescence system and Dr. Eugene Haller for providing us with germanium detectors. Brooke Bafus work on taking p-quaterphenyl spectra was very supportive and Slade Jokela's help with the vapor deposition system is extremely highly appreciated.

I personally want to thank my beloved wife Valentina for her understanding and constant help and love, which created a supportive and warm atmosphere in our home, and also for bringing our two sons, Michael and Nicholas, into the world.

INFRARED SPECTROSCOPY OF CONJUGATED ORGANIC MOLECULES UNDER HIGH PRESSURE

Abstract

By Kirill Khamidovich Zhuravlev, Ph.D.

Washington State University

May 2004

Chair: M. D. McCluskey

Conjugated organic molecules are important components in solid-state optoelectronic devices and laser dyes. Changes in the conformations of these molecules affect the optical emission wavelengths. In order to probe the conformation of conjugated molecules, infrared (IR) spectroscopy was performed on organic solids under high hydrostatic pressures.

We investigated polyphenyl molecules, such as biphenyl, p-terphenyl, and p-quaterphenyl. It was shown that polyphenyl molecules experience a phase transition in which molecules change their conformation from a twisted to a planar structure. This transition manifests itself in dramatic changes in the IR spectra. Beyond a critical pressure, specific IR-active modes abruptly become IR-inactive.

IR spectra have been obtained with a Bomem DA8 Fourier-Transform IR spectrometer in the 500-5000 cm^{-1} spectral range. Those spectra clearly showed that when the pressure increases above the critical value some IR-peaks completely

disappear from the spectrum. The critical pressure was found to range from 0.2 GPa for biphenyl to 0.9 GPa for p-quaterphenyl molecule.

Numerical analysis of conjugated molecules has been done using *ab initio* calculations. Using the local density approximation, calculations of molecular structure, vibrational frequencies, and IR intensities were performed. The results of these numerical simulations confirmed the experimental observations and allowed us to resolve a controversy about the p-terphenyl structure in the twisted conformation. They also demonstrated that high-pressure IR spectroscopy can be a very sensitive tool in probing molecular structure.

In order to investigate the effect of pressure, as dimensions approach the nano-scale, IR spectroscopy was performed on nm-thick organic films. The special technique called surface-enhanced infrared absorption spectroscopy (SEIRA) has been applied to the investigation of a thin film (30 nm) of p-nitrothiophenol under high pressure. The phenomenon of absorption enhancement in the presence of thin metal film has been used to obtain the absorption spectra of thin layer of p-nitrothiophenol.

Table of contents

List of Tables:

List of figures:

1. Objectives of this work

The application of high pressure is widely used in physical experiments to study the properties of condensed-matter systems. It is known that pressure can change solid-state structures and induce various phase transitions in materials. Novel structures can be synthesized using high pressure, which are important for both technological applications and fundamental research.

The objective of this work was to investigate the behavior of organic solids under high hydrostatic pressure. Among all organic solids we chose conjugated molecules, which have wide applications in organic light-emitting devices and laser dyes. Those molecules are known to undergo phase transitions when either temperature or pressure rises above critical values.

Specific objectives included studying the optical properties of polyphenyl (biphenyl, p-terphenyl, and p-quaterphenyl) solids, numerical simulations of molecular structures, and investigation of thin films of p-nitrothiophenol (p-NTP), when the solid becomes quasi-two-dimensional. We obtained infrared (IR) spectra of those solids and thin films using Fourier-transform infrared spectrometry and we used diamond-anvil cells to generate high pressures up to 10 GPa. By obtaining the vibrational spectra as a function of pressure, phase transitions were observed.

An essential part of this work was the comparison between the calculations and the experimental data. Toward that end, we performed *ab initio* calculations of molecular structure and vibrational properties of the molecules under investigation and compared those results with experiment. In the case of biphenyl, for which the structure is well

known, the comparison between theory and experiment provided a validation of our approach. For p-terphenyl, the combined theoretical and experimental techniques yielded information about its molecular structure.

2. Organization of thesis

Section 3 reviews the theory behind phase transitions and models for quantum chemistry. Hartree-Fock, Thomas-Fermi, and density-functional theory are considered for modeling molecular structures. The basics of numerical calculations are presented. Landau theory and scaling hypotheses, along with the notion of imcommensurate phases, are described.

Section 4 reviews applications and methods of investigation of organic solids, along with some results on polyphenyl molecules.

Section 5 describes the high-pressure apparatus and Fourier-Transform IR (FT-IR) spectroscopy technique. Some attention is given to *in situ* pressure measurements, infrared detectors, and comparative advantages of FT-IR with respect to grating spectrometers.

Section 6 shows the results obtained in this work on polyphenyl solids and a thin film of p-NTP. Experimental observations are supported by subsequent numerical simulations. Using a combined experimental and computational approach, the controversy about the structure of low-pressure phase of p-terphenyl is resolved. Extra emphasis is given to surface-enhanced infrared and Raman techniques. Surface-enhanced IR absorption (SEIRA) was successfully applied to the study of a p-NTP thin film.

3. Theoretical background

In this section, theoretical issues pertaining to quantum chemistry, group theory, and phase transitions are discussed. *Ab initio* calculation techniques and density functional theory (DFT), using the local density approximation, are described. These calculations are essential to interpret the experimental results, as discussed in Sec. 6. As it will be discussed in that Section, we observed second-order phase transitions under high pressure. The theory of phase transitions will therefore be reviewed here. Moreover, it is known that biphenyl has two types of low-pressure phases and those phases are incommensurate. Although our experimental technique is not sensitive to the transition between two incommensurate phases, for the sake of completeness, the theoretical background behind incommensurability in solids is reviewed in this Section.

3.1 Methods of quantum chemistry.

3.1.1. Self-consistent field theory.

In 1926 E. Schroedinger introduced his famous equation[1], which has become the cornerstone of nonrelativistic quantum mechanics. The Schroedinger equation determines the energies of a quantum system and the corresponding wavefunctions:

$$\hat{H}\Psi = E\Psi \qquad (1)$$

where $\hat{H}$ is the Hamiltonian operator, E is the energy, and Ψ is the wavefunction. Though it looks very simple, this equation is extremely difficult to solve for all but a very

limited number of cases. In general, it is necessary to use approximations that enable one to derive solutions to the Schroedinger equation.

In the general case, the Hamiltonian operator for an atom is given by:

$$\hat{H} = -\sum_i \left(\frac{1}{2}\Delta_i + \frac{Z}{r_i} \right) + \frac{1}{2}\sum_{i \neq j} \frac{1}{\left| \vec{r}_i - \vec{r}_j \right|}, \qquad (2)$$

where atomic units are used throughout this chapter, Z is the charge of the atomic nucleus, and $\vec{r}_i$ is the radius-vector of the i^{th} electron. The first two terms describe the kinetic and potential energy of electrons in the field of the atomic nucleus, whereas the last term describes the electron-electron interaction. It is this term that makes the equation so hard to solve. Only the hydrogen atom can be solved exactly using the Schroedinger equation—even for the helium atom one must use some approximations. The first successful approach to solve the problem of atomic structure was made by Hartree[2]. The Hartree method was later extended by Fock[3] to take into account the Pauli exclusion principle.

The Hartree approach is based on the variational principle, which states that for the true ground-state wavefunction, the energy of the system is at its minimum. Thus from the variational principle one can write for an arbitrary wavefunction Ψ, such that $|\Psi|^2 = 1$, that the following inequality holds:

$$E_0 \leq \langle \Psi | \hat{H} | \Psi \rangle, \qquad (3)$$

where E_0 is the ground-state energy. The equality occurs only for the true ground-state wavefunction. Thus we can take a wavefunction, substitute it in (1), and find the minimum with respect to wavefunction variation $|\delta\Psi\rangle$. This procedure results in the following equation:

$$\langle \Psi | \hat{H} | \delta\Psi \rangle - \langle \Psi | E | \delta\Psi \rangle = 0 \quad . \qquad (4)$$

Since Eq. (4) must be true for any arbitrary variation in wavefunction, one can write

$$\langle \Psi | \hat{H} - \langle \Psi | E = 0 \quad . \qquad (5)$$

In the Hartree method the wavefunction, which is the trial solution of Eq. (1), is written as the product of one-electron wavefuctions:

$$\Psi = \psi_1(\vec{r}_1)\psi_2(\vec{r}_2)\cdots\psi_N(\vec{r}_N) \quad , \qquad (6)$$

where N is the number of electrons. Let us take the helium atom as an example[4]. For the ground state we choose:

$$\psi(\vec{r}_1, \vec{r}_2) = \frac{Z_{eff}^3}{\pi} e^{-Z_{eff} r_1} \frac{Z_{eff}^3}{\pi} e^{-Z_{eff} r_2} \quad , \qquad (7)$$

where Z_{eff} is the effective charge of the atomic nucleus due to screening by the electrons. Substituting Eq. (7) into Eq. (1) yields the energy as a function of Z_{eff}. Minimizing that expression with respect to Z_{eff} yields the value of the effective charge Z_{eff} and the ground-state energy E. For the helium atom, the ground-state energy is given by:

$$E = Z_{eff}^2 - 2ZZ_{eff} + \frac{5}{8} Z_{eff} \quad . \qquad (8)$$

The minimum occurs at Z_{eff}=Z-5/16, which yields E=-2.85 a.u. (the experimental value is -2.90).

The Hartree method does not take into account the exchange interaction between electrons. This interaction is a result of the Pauli exclusion principle, which states that no two fermions (e.g., electrons) can occupy the same quantum state. The Pauli principle is accounted for in the Hartree-Fock (HF) approximation. This approach uses multielectron wavefunctions in the form of a so-called Slater determinant:

$$\Psi = \frac{1}{\sqrt{N!}} \begin{vmatrix} \psi_1(\vec{r}_1,\sigma_1) & \psi_1(\vec{r}_2,\sigma_2) & \cdot & \cdot & \psi_1(\vec{r}_N,\sigma_N) \\ \psi_2(\vec{r}_1,\sigma_1) & \cdot & \cdot & \cdot & \cdot \\ \cdot & \cdot & \cdot & \cdot & \cdot \\ \cdot & \cdot & \cdot & \cdot & \cdot \\ \psi_N(\vec{r}_1,\sigma_1) & \cdot & \cdot & \cdot & \psi_N(\vec{r}_N,\sigma_N) \end{vmatrix}, \qquad (9)$$

where σ_i denotes the spin variable of the i^{th} electron. This wavefunction is constructed to satisfy the Pauli principle. The HF method often gives very good results for atomic ground-state energies.

Unfortunately, self-consistent HF equations also require much computational effort to be solved, especially in the case of heavy atoms. In this case, there is another approach that yields atomic parameters with fairly good accuracy. It is called the Thomas-Fermi model.

3.1.2. Thomas-Fermi theory.

For heavy atoms one can use a quasiclassical approach and think of electrons as a "gas" with a number density $n(\vec{r})$. The density of the electron gas is related to its Fermi wave vector by[4]:

$$n = \frac{p_F^3}{3\pi^2}. \qquad (10)$$

In an electrostatic field, the energy of an electron can be represented as

$$E = \frac{p^2}{2} - \varphi \quad , \qquad (11)$$

where φ is the potential. It is clear that E must be less than zero, otherwise the electron would not be bound. Therefore one can write:

$$\frac{p_F^2}{2} = \varphi - \varphi_0 \quad , \tag{12}$$

where $-\varphi_0$ is the maximum value of electron total energy. Substituting Eq. (12) into Eq. (10) yields:

$$n = \frac{1}{3\pi^2}\left[2(\varphi - \varphi_0)\right]^{3/2} \quad . \tag{13}$$

For a neutral atom, n=0 at the atom's boundary. From Gauss's Law, $\varphi = 0$ outside any centrosymmetric charge distribution. Hence, it follows that $\varphi_0 = 0$. From the Poisson equation, $\Delta\varphi = 4\pi n$, we obtain the following equation:

$$\Delta\varphi = \frac{8\sqrt{2}}{3\pi}\varphi^{3/2} . \tag{14}$$

This is the central equation in the Thomas-Fermi theory. It is valid only at distances which satisfy the following criteria:

$$1/Z < r < 1 \quad . \tag{15}$$

Therefore, Thomas-Fermi theory works well only for heavy atoms, where Z is sufficiently large.

3.1.3. Density-functional theory.

Density-functional theory (DFT) unites the Hartree-Fock method and Thomas-Fermi theory. It has proved to be a very powerful tool for *ab initio* calculations.

In 1964 Hohenberg and Kohn[5] proved that the ground state density of a system of electrons uniquely determines the external potential which acts upon these electrons. A

proof by contradiction is outlined here. Suppose we have two distinct potentials $v(\vec{r})$ and $v'(\vec{r})$, such that $v(\vec{r}) - v'(\vec{r}) \neq \text{const}$. If we assume that both potentials give rise to the same electron density $n(\vec{r})$, then we can write, using the minimum property of the ground state $|\Psi\rangle$:

$$\begin{aligned} E = \langle \Psi | H | \Psi \rangle < \langle \Psi' | H | \Psi' \rangle = \langle \Psi' | H' | \Psi' \rangle + \\ \langle \Psi' | v(\vec{r}) - v'(\vec{r}) | \Psi' \rangle = E' + n(\vec{r})(v(\vec{r}) - v'(\vec{r})) \end{aligned} , \qquad (16)$$

where $|\Psi'\rangle$ is the ground state wavefunction for Hamiltonian H'.

Analogously we can obtain:

$$\begin{aligned} E' = \langle \Psi' | H' | \Psi' \rangle < \langle \Psi | H' | \Psi \rangle = \langle \Psi | H | \Psi \rangle + \\ \langle \Psi | v'(\vec{r}) - v(\vec{r}) | \Psi \rangle = E + n(\vec{r})(v'(\vec{r}) - v(\vec{r})) \end{aligned} . \qquad (17)$$

By adding Eq. (16) and Eq. (17), it follows that $E + E' < E' + E$, which is impossible. This proves the central theorem of density functional theory.

For the electrons in an external potential $v(\vec{r})$ the ground state energy can be written as[6,7]

$$E = \int v(\vec{r}) n(\vec{r}) d\vec{r} + \frac{1}{2} \int \frac{n(\vec{r}) n(\vec{r}')}{|\vec{r} - \vec{r}'|} d\vec{r} d\vec{r}' + G[n] \quad , \qquad (18)$$

where G is a functional of density, the exact form of which is unknown:

$$G[n] \equiv T_s[n] + E_{xc}[n] \quad , \qquad (19)$$

where $E_{xc}[n]$ is the exchange-correlation functional.

Then, using the fact that $\int \delta n(\vec{r}) d\vec{r} = 0$, one can obtain the following system of equations:

$$\varphi(\vec{r}) = v(\vec{r}) + \int \frac{n(\vec{r}')}{|\vec{r} - \vec{r}'|} d\vec{r}' \qquad (20)$$

$$\mu_{xc}(n) \equiv d(E_{xc}[\tilde{n}(\vec{r})])/d\tilde{n}(\vec{r})\big|_{\tilde{n}(\vec{r})=n(\vec{r})} \tag{21}$$

$$\left\{-\frac{1}{2}\nabla^2 + [\varphi(\vec{r}) + \mu_{xc}(n(\vec{r}))]\right\}\psi_i(\vec{r}) = \varepsilon_i\psi_i(\vec{r}) \tag{22}$$

$$n(\vec{r}) = \sum_{i=1}^{N}|\psi_i(\vec{r})|^2 \tag{23}$$

The system (20)-(23) must be solved self-consistently. The energy is given by:

$$\begin{aligned} E = &\sum_{i=1}^{N}\varepsilon_i - \frac{1}{2}\iint\frac{n(\vec{r})n(\vec{r}')}{|\vec{r}-\vec{r}'|}d\vec{r}d\vec{r}' \\ &+ E_{xc}[n(\vec{r})] - \int n(\vec{r})\mu_{xc}(n(\vec{r}))d\vec{r} \end{aligned} \tag{24}$$

It is necessary to emphasize that the energies ε_i and wavefunctions $\psi_i(\vec{r})$ do not have any physical meaning by themselves. Only the electron density [Eq. (23)] and the energy of the system [Eq. (24)] have physical meaning[6,7].

Since the exact form of the functional $E_{xc}(n(\vec{r}))$ is unknown, an approximate form must be used. Since the introduction of DFT, several approximations have been developed. The most prominent and famous is the *local density approximation* (LDA), which represents the exchange-correlation functional as:

$$E_{xc}[n] \approx E_{xc}^{LDA} = \int e_{xc}(n(\vec{r}))n(\vec{r})d\vec{r} \tag{25}$$

where $e_{xc}(n)$ is the exchange-correlation energy per particle in a uniform electron gas[7].

This approximation in many cases turns out to work very well for determining molecular structures. It also gives fairly good accuracy for ionization energies of atoms and dissociation energies of molecules. Nevertheless, it fails in determining band gaps in solids, heavy fermion systems, and other systems with strong electron-electron interactions.

3.1.4. Molecular structure determination.

When two or more atoms come close together, their electronic clouds overlap and, in certain cases, form a bond between the atoms. The Hamiltonian for this system includes terms describing the interaction of nuclei with each other, as well as electrons with not only their parent nuclei but also with all other nuclei in the molecule.

$$\hat{H}\left(\vec{\mathbf{R}}_1,\ldots,\vec{\mathbf{R}}_N;\vec{\mathbf{r}}_1,\ldots,\vec{\mathbf{r}}_M\right)=-\sum_{i=1}^{N}\frac{1}{2M_i}\Delta_{\vec{\mathbf{R}}_i}-\frac{1}{2}\sum_{i=1}^{M}\Delta_{\vec{\mathbf{r}}_i}+ \frac{1}{2}\sum_{i\neq j}\frac{Z_iZ_j}{\left|\vec{\mathbf{R}}_i-\vec{\mathbf{R}}_j\right|}-\sum_{i=1}^{N}\sum_{j=1}^{M}\frac{Z_i}{\left|\vec{\mathbf{R}}_i-\vec{\mathbf{r}}_j\right|}+\frac{1}{2}\sum_{i\neq j}\frac{1}{\left|\vec{\mathbf{r}}_i-\vec{\mathbf{r}}_j\right|} \tag{26}$$

Here M is the total number of electrons; N is the number of nuclei; Z_i is the charge and M_i is the mass of the i^{th} nucleus; $\vec{\mathbf{R}}_i$ and $\vec{\mathbf{r}}_j$ are radius-vectors of the i^{th} nucleus and j^{th} electron, respectively.

We can significantly simplify the operator in Eq. (26), using the fact that the mass of a nucleus is over a thousand times larger than the mass of an electron. Thus one can neglect the kinetic energy of the nuclei, which is the first term in Eq. (26). All the nuclei are assumed to be fixed in space, and the potential energy of their interaction with each other is just an additive constant to the Hamiltonian, which can be added to the total energy of the system. The Hamiltonian of the system is then given by:

$$\hat{H}\left(\vec{\mathbf{R}}_1,\ldots,\vec{\mathbf{R}}_N;\vec{\mathbf{r}}_1,\ldots,\vec{\mathbf{r}}_M\right)=-\frac{1}{2}\sum_{i=1}^{M}\Delta_{\vec{\mathbf{r}}_i}-\sum_{i=1}^{N}\sum_{j=1}^{M}\frac{Z_i}{\left|\vec{\mathbf{R}}_i-\vec{\mathbf{r}}_j\right|}+\frac{1}{2}\sum_{i\neq j}\frac{1}{\left|\vec{\mathbf{r}}_i-\vec{\mathbf{r}}_j\right|} \tag{27}$$

This approximation is called the Born-Oppenheimer approximation. We are left with a Hamiltonian operator for the electronic coordinates only. The solution to the

corresponding Schroedinger equation yields the electronic wavefunction, $\Psi\left(\vec{\mathbf{r}}_1,\ldots,\vec{\mathbf{r}}_M;\{\vec{\mathbf{R}}_i\}\right)$, and the energy of the system, $E\left(\{\vec{\mathbf{R}}_i\}\right)$, which depend parametrically on the internuclear distances. The minimum of the energy with respect to the variation of internuclear distances determines a possible stable structure of the molecule, and the global minimum corresponds to the ground-state energy of the molecule. The nuclear motion is then considered as if all the nuclei moved in the potential $U\left(\mathbf{R}_1,\ldots,\mathbf{R}_N\right)=E\left(\{\mathbf{R}_i\}\right)$. Energy levels for such a potential correspond to vibrational levels of the molecule. A discussion of molecular vibrations will be given in the following sections.

3.1.5. Group theory.

The set of elements A is called a *group* if there is an operation, which we will call *multiplication*, defined on this set such that all the elements of the set obey the following postulates[8]:

1. For every two elements, a and b from A, the element c=ab belongs to the set A.
2. The associative law of multiplication holds: abc=(ab)c=a(bc).
3. There is an element e in A, such that ae=ea=a. This element is called the unity element.
4. For every a in A, there is an element, called a^{-1}, such that $aa^{-1}=a^{-1}a=e$. This element is called the inverse of a.

The multiplication operation does not necessarily mean ordinary multiplication. It can be a combination of operations; for example, two differentiations. Examples of groups include the set of all integers with respect to addition, the set of all rational numbers with respect to ordinary multiplication, and the set of n×n invertible matrices with respect to matrix multiplication.

The importance of group theory to physics and chemistry is hard to overestimate. Applying group-theoretical analysis, one can determine the vibrations that give rise to infrared (IR) active modes and Raman active modes in the molecular spectra, determine the degeneracy of molecular energy levels, and so on.

When dealing with a particular molecule, one can perform a number of operations on it; namely, rotation about given axis, reflection about a given plane, inversion, or a combination of rotation and inversion. It is clear that only rotations by the angle $2\pi/n$, where n is an integer, form a group of rotations*. The axis of rotation is called the axis of n^{th} order and is denoted as $\mathbf{C_n}$. If the symmetry operations involve a rotation plus inversion operation, then the axis is denoted as $\mathbf{S_n}$. The main axis of rotation is the axis of the highest order. The plane of reflection is marked as $\boldsymbol{\sigma}$ and is given the subscript **v** or **h**, depending on whether the plane contains the main axis of rotation or is perpendicular to it, respectively. Thus if the plane contains the main axis, it is $\boldsymbol{\sigma_v}$, and if the plane is perpendicular to it, it is the $\boldsymbol{\sigma_h}$ plane. The inversion operation is denoted by the symbol **i**.

* If electrons are considered, the rotations by $4\pi/n$ form a group of rotations, due to electron spin.

It is straightforward to verify that all the operations described above leave at least one point of the molecule unmoved in space. Therefore such a group of operations is called a *point group*. In the following sections, several specific examples are described.

3.1.6. Examples of point groups.

Water.

The water molecule (H_2O) is a planar molecule, with the H-O-H angle equal to 105°. The operations that leave the molecule unchanged are:

- Rotation about the axis passing through the oxygen atom and bisecting the H-O-H angle by 180°;
- Reflection about the plane containing this axis and the molecule itself;
- Reflection about the plane, perpendicular to the plane of the molecule and containing the axis of rotation.

The point group to which the water molecule belongs is C_{2v}, because it has the axis of rotation of the second order and two planes of reflection that contain this axis, which is designated by the subscript **v** in the name of the group. The molecule is shown in Fig. 1.

Hydrogen peroxide.

The hydrogen peroxide molecule (H_2O_2) in the *cis*-form belongs to the C_{2v} point group as well. In its *trans*-form it has the following symmetry elements:

- The center of inversion;
- The axis of rotation of the second order, which is perpendicular to the molecule plane;
- The plane of reflection that coincides with the plane of the molecule.

Because the plane of reflection is perpendicular to the main axis of rotation, the point group of this molecule is C_{2h}. Again, the subscript **h** denotes the fact that the main axis and the plane of symmetry are orthogonal. The molecule is shown in Fig. 2.

Benzene.

The benzene molecule (C_6H_6) has the following symmetry elements:

- The main axis of 6^{th} order, perpendicular to the molecule plane;
- The plane of reflection, which coincides with the molecule plane;
- The center of inversion;
- 6 planes of reflection containing the main axis of symmetry and being perpendicular to the molecule plane;
- 6 axes of rotation of the second order, which are the lines of intersection of the plane of the molecule and 6 planes of reflection.

Because of these second-order rotational axes, the group is labeled by the symbol D. Finally, the point group of the benzene molecule is D_{6h}. The molecule is shown in Fig. 3.

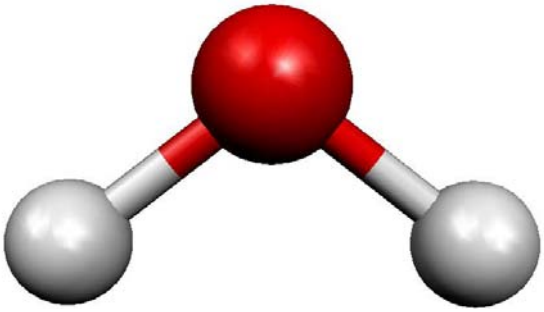

Figure 1. Water molecule.

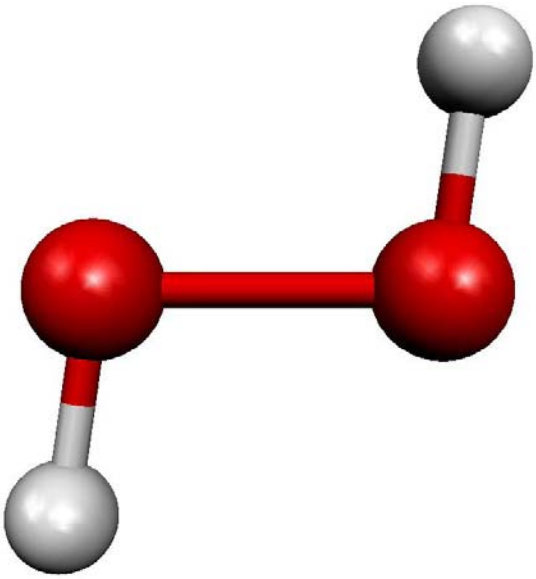

Figure 2. Hydrogen peroxide molecule.

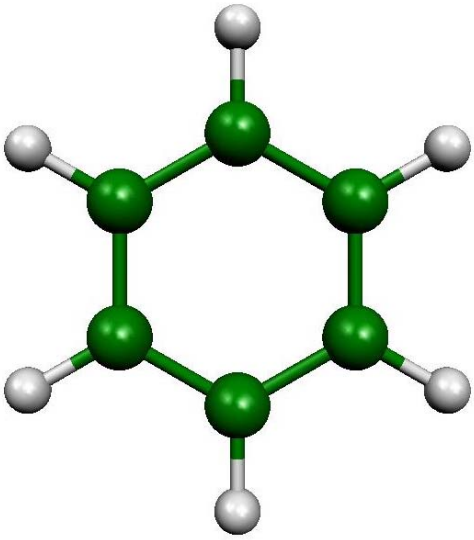

Figure 3. Benzene molecule.

3.1.7. Mathematical background.

In order to describe a symmetry operation, denoted as $\mathbf{R}$, we can use the coordinate system in real space and represent any operation as a transformation of the radius-vector $\vec{\mathbf{r}}$. It is well known that the transformation of any vector into another vector can be performed by a matrix T. Every symmetry operation can therefore be described by a matrix, reducing the group theory to the algebra of matrices. Such a set of matrices is said to form a *representation* of the group. We will use the symbol Γ to denote a particular representation. There are many possible representations of the group. If one set of matrices $\{B\}$ can be obtained from another $\{A\}$ by the rule

$$\{B\} = Q^{-1}\{A\}Q \quad , \qquad (28)$$

then these two representations are said to be *equivalent*. Equation (28) states that there is an invertible matrix Q such that for any matrix from the set $\{A\}$ there is a matrix in the set $\{B\}$ that can be obtained by a unitary transformation. If the matrices of the given representation can be simultaneously broken into block-diagonal form, the representation is called *reducible*. Otherwise it is called *irreducible*, and these are the representations that are of interest to us.

The trace of a matrix of a given operation is called the *character* of this operation. It is denoted by the symbol χ, so that $\chi(\mathbf{R})$ is the character of the operation **R**. The set of all characters for a particular representation is called the character of the representation. In the case of irreducible representations of a point group, characters form a *table of characters*, which completely describes the group. The Great Orthogonality Theorem

holds for such a table of characters. We provide its formulation without proof here, which can be found elsewhere[8].

Great Orthogonality Theorem:

If Γ^{μ} and Γ^{ν} are two non-equivalent irreducible representations with matrices $D^{\mu}(\mathbf{R})$ and $D^{\nu}(\mathbf{R})$ of dimensions n_{μ} and n_{ν}, respectively, then the matrix elements are related by the equation

$$\sum_{\mathbf{R}} D^{\mu}_{ik}(\mathbf{R}) D^{\nu}_{mj}(\mathbf{R}^{-1}) = \left(g/n_{\mu}\right)\delta_{\mu\nu}\delta_{ij}\delta_{km} \qquad (29)$$

where g is the order of the group and the sum is over all the operations **R**. With the help of this theorem, it is possible to expand any reducible representation into a sum of irreducible representations. This theorem has many applications, and in the next section it is used to solve the problem of molecular vibrations.

3.1.8. Application of group theory to molecular vibrations.

For a molecule consisting of N atoms, there are 3N possible atomic displacements. Some of these displacements, however, will involve motion in which no bond length or bond angle changes. Those displacements correspond to translation along, and rotation about, three non-coplanar axes. The Hamiltonian of the system can be written as:

$$H\left(x_1, x_2, \ldots, x_{3N}\right) = \sum_{i=1}^{3N} \frac{p_i^2}{2M_i} + W\left(x_1, x_2, \ldots, x_{3N}\right) \quad , \qquad (30)$$

where W is the potential energy of the N nuclei. The potential can be expanded around the equilibrium as follows:

$$W(x_1, x_2, \ldots, x_{3N}) = W_0 + \sum_{i=1}^{3N} \frac{\partial W}{\partial x_i}\left(x_i - x_{i_0}\right) + \frac{1}{2}\sum_{i=1}^{3N}\sum_{j=1}^{3N} \frac{\partial^2 W}{\partial x_i \partial x_j}\left(x_i - x_{i_0}\right)\left(x_j - x_{j_0}\right) + \cdots \quad (31)$$

The constant factor W_0 can be set to zero. In addition, at equilibrium, all first derivatives vanish. Thus we obtain the Hamiltonian:

$$W(x_1, x_2, \ldots, x_{3N}) = \sum_{i=1}^{3N} \frac{p_i^2}{2M_i} + \frac{1}{2}\sum_{i=1}^{3N}\sum_{j=1}^{3N} \frac{\partial^2 W}{\partial x_i \partial x_j}\left(x_i - x_{i_0}\right)\left(x_j - x_{j_0}\right) + \cdots \quad (32)$$

Restricting the expansion to the quadratic terms, we obtain the harmonic approximation. Second derivatives of the potential energy are called *harmonic force constants*. Replacing $x_i - x_{i_0}$ by q_i, displacement from equilibrium for the i^{th} coordinate, yields:

$$H(q_1, q_2, \ldots, q_{3N}) = \sum_{i=1}^{3N} \frac{p_i^2}{2M_i} + \frac{1}{2}\sum_{i=1}^{3N}\sum_{j=1}^{3N} B_{ij} q_i q_j \quad , \quad (33)$$

where $B_{ij} = \frac{\partial^2 W}{\partial x_i \partial x_j}$. One can find a linear transformation of coordinates q_i that diagonalizes the matrix $\|B_{ij}\|$. The Hamiltonian is then expressed as:

$$H(\xi_1, \xi_2, \ldots, \xi_{3N}) = \sum_{i=1}^{3N} \frac{p_i^2}{2M_i} + \frac{1}{2}\sum_{i=1}^{3N} k_i \xi_i^2 \quad , \quad (34)$$

where ξ_i are the new coordinates, called *normal coordinates*. The coefficients k_i are ordinary force constants for the harmonic oscillator. Since six modes correspond to translational and rotational motion, exactly six coefficients k_i will be equal to zero. Excluding those coefficients from consideration, we can write the Hamiltonian for the vibrational problem:

$$H(\xi_1,\xi_2,\ldots,\xi_{3N-6}) = \sum_{i=1}^{3N-6} \frac{p_i^2}{2M_i} + \frac{1}{2}\sum_{i=1}^{3N-6} k_i \xi_i^2 \qquad (35)$$

Since any symmetry operation leaves the molecule unchanged, the Hamiltonian is preserved under symmetry operations. It is known that every normal coordinate belongs to an irreducible representation of the group. The corresponding harmonic-oscillator wavefunctions (1st excited state) belong to the same representation. A group-theoretical analysis is used to determine the modes which are IR- or Raman active.

Example: H_2O.

As an example, consider the water molecule. It belongs to the C_{2v} point group. The table of characters is given as follows[8]:

C_{2v}	E	$C_2(z)$	σ_{xz}	σ_{yz}
A_1	1	1	1	1
A_2	1	1	-1	-1
B_1	1	-1	1	-1
B_2	1	-1	-1	1
Γ_{site}	3	1	1	3
$\Gamma_{\vec{R}}$	3	-1	1	1
Γ_{3N}	9	-1	1	3

In order to obtain the representation for 3N atomic displacements, Γ_{3N}, we must take the direct product of two representations: for the radius-vector $\vec{\mathbf{R}}$, $\Gamma_{\vec{R}}$, and for the

atomic sites Γ_{site}. The representation for the radius-vector is, in turn, the direct product of the representations of x-, y-, and z-components. In our case these are A_2, B_1, and B_2 representations. The character of a given transformation for the Γ_{site} representation is equal to the number of atoms that remain stationary under this transformation. The results for two representations (radius-vector and sites) are listed in table of characters. The last line represents the characters for the representation with atomic displacements as the basis, where $\Gamma_{3N} = \Gamma_{\vec{R}} \otimes \Gamma_{site}$. Using the Great Orthogonality Theorem we can expand Γ_{3N}:

$$\Gamma_{3N} = 3A_1 \oplus \quad A_2 \oplus \quad 2B_1 \oplus \quad 3B_2 \qquad (36)$$

As was mentioned before, there are six modes which are rotational or translational modes. We must exclude those from Eq. (36). Three translations correspond to A_1, B_1, and B_2 representations respectively. Three rotations correspond to A_2, B_1, and B_2 representations. Subtracting those six modes from Eq. (36) yields:

$$\Gamma_{3N} = 2A_1 \oplus B_2 \qquad (37)$$

Considering the water molecule qualitatively, there are symmetric modes, with hydrogen atoms moving along the O-H bonds for one mode and with H-O-H angle oscillating around its equilibrium value (Fig. 4) for the other mode. In addition there is one asymmetric mode, where the hydrogen atoms move along the bonds, out of phase with the oxygen atom (Fig. 4). The two symmetric modes belong to the A_1 representation and the asymmetric one belongs to the B_2 representation.

Now we may ask the question: which modes are IR-active and which are not? IR-activity means that if we shine light onto the system, the mode absorbs energy and becomes excited. The transmitted light intensity at the frequency corresponding to this

mode decreases. For a mode to be IR-active, it must have a nonzero dipole moment induced (Appendix A). For the water molecule, the answer is evident from Figure 1. The two symmetric modes produce a dipole moment along the z-axis (which is also the main axis of symmetry), and the asymmetric mode produces a dipole moment in the plane of the molecule perpendicular to the main axis. Thus, for the water molecule, all three modes should be IR-active. In fact, it is known from experiments that this is the case.

Group theory can be used to unambiguously determine the IR activity of vibrational modes. In order for the mode to become excited, there must be a nonzero probability for the transition from the ground state to this particular excited state. The transition rate is given by:

$$P_{0a} \propto \left| \int \psi_0(\tau) \vec{\mathbf{d}} \psi_a(\tau) d\tau \right|^2 \quad , \tag{38}$$

where ψ_0 and ψ_a are wavefunctions of the ground state and the excited state, respectively, and $\vec{\mathbf{d}}$ is the dipole moment. The set of all arguments, on which the wavefunctions depend, is labeled τ.

The integral in Eq. (38) will be zero if the integrand is an odd function. The wavefunction of the ground state always belongs to the totally symmetric representation (A_1 in the case of the water molecule). Thus integral in (38) is zero unless ψ_a belongs to the same representation as the dipole moment. The dipole moment has the same symmetry as the radius-vector $\vec{\mathbf{R}}$. In the case of the water molecule,

$$\Gamma_{\vec{\mathbf{R}}} = A_1 \oplus B_1 \oplus B_2$$

Hence, ψ_a must belong to the A_1, B_1, or B_2 representation. From Eq. (37), it is apparent that all three modes are IR-active.

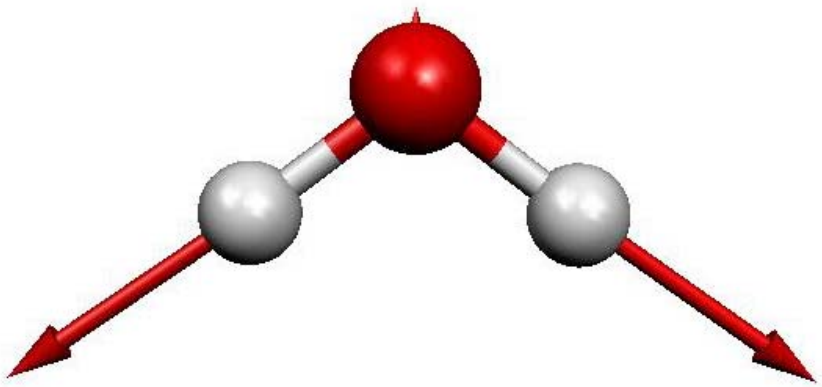

Symmetric stretch mode

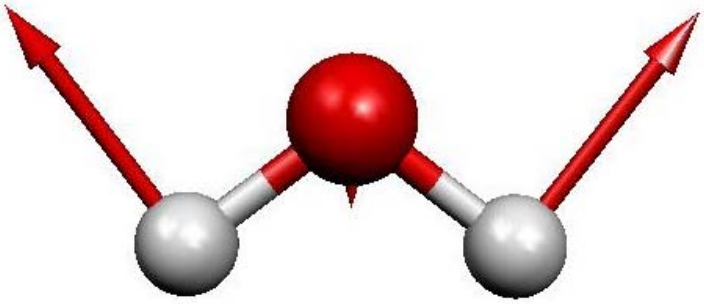

Symmetric wagging mode

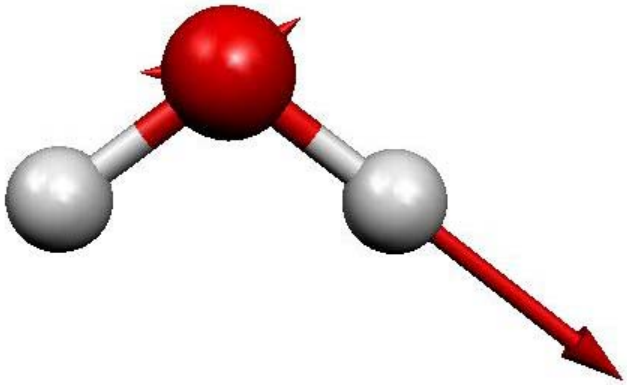

Asymmetric stretch mode

Figure 4. Vibrational normal modes of the water molecule.

3.2. Numerical calculations.

As it was seen in the previous sections, in order to determine a molecular structure we must solve the Schroedinger equation with a Hamiltonian given by Eq. (27). The computational resources required to solve this equation grow rapidly with the number of electrons. In order to apply any of the available numerical methods, we must limit the number of electrons taken into account. It is known that usually only the outer electrons are involved in bond formation. To first order, the inner-shell electrons can be ignored. This approximation greatly reduces the number of basis wavefunctions involved in the calculation.

In any numerical method of solving the Schroedinger equation, the one-electron wavefunctions are expanded in terms of certain basis functions, which are usually chosen to be orthonormal. This significantly reduces the computational cost of solving all the equations.

Currently there are commercially available software packages which perform the task of calculating molecular structures. In this work, the Gaussian98 program (Ref. 9) has been used. It has many built-in methods, including Hartree-Fock and DFT, and uses a variety of basis sets. All the basis sets include Gaussian-type functions; i.e., functions that look like[9]:

$$g(\alpha,\vec{\mathbf{r}}) = c x^n y^m z^l e^{-\alpha r^2} \quad , \qquad (39)$$

where x, y, and z are components of the radius-vector $\vec{\mathbf{r}}$ and c is the normalization constant. All such functions are normalized to unity:

$$\int_{\text{all space}} g^2 = 1 \qquad (40)$$

The list of different basis sets used by Gaussian program is given in Table I:

Table I. Description of the basis sets used by GAUSSIAN program.

Basis set [Applicable atoms]	**Description**	**# Basis Functions**	
		1st row atoms	**hydrogen atoms**
STO-3G [H-Xe]	Minimal basis set: use for more qualitative results on very large systems.	5	1
3-21G [H-Xe]	Split valence: 2 sets of functions in the valence region provide a more accurate representation of orbitals.	9	2
6-31G(d), 6-31G* [H-Cl]	Adds polarization functions to heavy atoms. (This basis set uses the 6-component type d-functions.)	15	2
6-31G(d,p), 6-31G** [H-Cl]	Adds polarization functions to the hydrogens too.	15	5
6-31+G(d) [H-Cl]	Adds diffuse functions: important for systems with lone pairs, anions, excited states.	19	2
6-31+G(d,p) [H-Cl]	Adds p-functions to hydrogens as well.	19	5
6-311+G(d,p) [H-Br]	Triple zeta: adds extra valence functions (3 sizes of s and p functions) to 6-31+G(d).Diffuse functions can be added to the hydrogen atoms via a second +.	22	6
6-311+G(2d,p) [H-Br]	Puts 2d functions on heavy atoms (plus diffuse functions), and 1p function on hydrogens.	27	6
6-311+G(2df,2p) [H-Br]	Puts 2d functions and 1f function on heavy atoms (plus diffuse functions), and 2p functions on the hydrogen atoms.	34	9
6-311+G(3df,2pd) [H-Br]	Puts 3d functions and 1f function on heavy atoms, and 2p functions and 1d function on hydrogens, as well as diffuse functions on both.	39	15

3.3. Theory of phase transitions.

In the present work, we observed second-order phase transitions in conjugated organic solids under high pressure. It is therefore necessary to discuss the theory behind those phenomena. It is also known that biphenyl has two low-pressure phases which are incommensurate. Although our experimental methods are not sensitive to incommensurate-incommensurate phase transitions, the issues related to incommensurate phases are briefly discussed.

3.3.1 General properties of phase transitions.

When two or more macroscopically distinguishable substances are located in a given system, it is said that the system consists of several *phases.* Examples of such systems include ice-water (solid-liquid system), mercury-water (two immiscible liquids), and water-air (liquid-gas system) mixtures. In all multiphase systems, different phases are separated by interfaces such that they are macroscopically distinct. When a chemically homogeneous material melts, evaporates, or undergoes some other structural transformation, it is said to undergo a *phase transition*.

During any phase transition, the thermodynamic potential per unit volume remains continuous with variations in temperature and pressure. Therefore, the condition for the phase transition to occur is such that specific thermodynamic potentials of two phases, Ψ_1 and Ψ_2, are equal[10]:

$$\Psi_1(P,T) = \Psi_2(P,T) \quad , \quad (41)$$

where P is pressure and T is temperature. Eq. (41) determines not just one point but rather a phase-transition line on the P-T diagram. For each point on this line, the two phases are in equilibrium with each other and can coexist in the system. On the side where $\Psi_1 > \Psi_2$, phase 2 is more stable, and on the other side, phase 1 is more stable.

If there are more than two phases for a given substance, there is a possibility of the coexistence of more than two phases. In this case the following condition must be satisfied:

$$\begin{aligned} &\Psi_1(P,T) = \Psi_2(P,T); \Psi_2(P,T) = \Psi_3(P,T); \cdots; \\ &\Psi_{n-1}(P,T) = \Psi_n(P,T); \Psi_n(P,T) = \Psi_1(P,T) \end{aligned} \tag{42}$$

where n is the total number of phases. From this equation it is clearly seen that three phases can coexist only at one point on P-T diagram. This point is called the *triple point*. It is also evident that for more than three phases, Eq. (42) can be satisfied only by accident. This means that, in general, more than three phases of the same material cannot coexist simultaneously.

As stated earlier, the specific thermodynamic potential for the material remains continuous throughout phase transformations. Its derivatives, however, can be discontinuous. Usually, phase transitions are divided into two types: first-order phase transitions and second-order phase transitions, depending on the properties of the first- and second-order derivatives of the thermodynamic potential.

3.3.2. First-order phase transitions.

In first-order phase transitions, the first derivatives of the thermodynamic potential Ψ are discontinuous. From the definition of Ψ, it is known that $\frac{\partial \Psi}{\partial T} = -s$ and $\frac{\partial \Psi}{\partial P} = v$, where s and v are the specific entropy and volume, respectively. Thus, either the specific entropy or specific volume of the substance, or both, exhibits a discontinuity upon the phase transition. The change in specific entropy is associated with the latent heat of the phase transition. It is this heat that is required to melt ice or boil a teapot. From the expansion of $\Psi(P,T)$ near the phase equilibrium, and condition (41), the following relationship can be derived:

$$\frac{dP}{dT} = \frac{s_2 - s_1}{v_2 - v_1} = \frac{q}{T(v_2 - v_1)} \quad , \tag{43}$$

where q is the heat required to transform phase 2 into phase 1. Eq. (43), known as the Clapeyron equation, defines the slope of the coexistence curve on the P-T diagram.

3.3.3. Second-order phase transitions.

Another type of phase transition is characterized by discontinuities in the second-order derivatives of the thermodynamic potential, while the first-order derivatives remain continuous. This means that during a second-order phase transition, the specific volume of the substance does not change, and no heat is added to or withdrawn from the system. At the same time, quantities such as the specific heat, bulk modulus, and thermal

expansion coefficient are discontinuous. Examples include the ferromagnetic-paramagnetic phase transition, Bose-Einstein condensation, and the conductor-superconductor transition.

In the case of ferromagnetic systems, such as iron or nickel, the material has a nonzero magnetic moment in the ferromagnetic phase. When the substance is heated above a certain temperature T_c, the magnetic moment becomes zero. This temperature is called the Curie temperature or critical temperature. The appearance of spontaneous magnetization below the critical temperature is the result of a second-order phase transition.

It is immediately evident that the paramagnetic phase and ferromagnetic phase possess different symmetries. In the paramagnetic phase, for an isotropic medium, the system is invariant under any rotation in space. In the ferromagnetic phase, the magnetic moment marks the preferred direction in space and the system is invariant only under rotations about this direction. The symmetry is therefore reduced. The phenomenon of symmetry reduction is a feature of all second-order phase transitions. In such a phase transition, the symmetry is said to be spontaneously broken.

Since one of the phases has lower symmetry, it requires more parameters to be described than the highly symmetric phase. The extra parameter that is necessary for such a description is called the *order parameter*. The order parameter is zero in the highly symmetric phase and becomes nonzero upon the phase transition. In the case of the ferromagnetic transition, it is magnetization that serves as the order parameter. The order parameter is measurable in the experiment and is the extensive thermodynamic variable.

Usually, the order parameter is associated with some intensive variable, which is conjugate to it. In the present example, the intensive variable is the magnetic field.

3.3.4. Landau theory of second-order phase transitions.

During second-order phase transitions, the thermodynamic potential is a continuous function of the intensive variables and so are its first-order derivatives. In the low-symmetry phase, the order parameter is nonzero and becomes zero upon the phase transition. It is natural to assume that near the phase transition point, the order parameter is the only parameter that is important. The thermodynamic potential can be expanded in powers of the order parameter[10,11]:

$$\Psi(\eta) = \Psi_0 - \eta H + a_0\eta^2 + a_1\eta^3 + a_2\eta^4 + \cdots + \frac{c}{2}|\nabla\eta|^2 + \cdots \qquad (44)$$

where η is the order parameter and H is the conjugated field. The last term in Eq. (44) is added in order to take into account the spatial variations in the order parameter. The importance of this term will be clarified in the sections that follow.

If the system properties are symmetric under reversal of η, then $a_1=0$. It is also assumed that $a_0 = r_0 t$, where $t = \frac{T - T_c}{T_c}$. Thus, in the absence of an external field, the thermodynamic potential above T_c has its minimum at $\eta=0$, whereas below the T_c there is a nontrivial value of the order parameter corresponding to the minimum in Ψ.

Landau theory deals only with quantities that are of macroscopic nature. It also ignores all fluctuations. In the simplest case, one can assume that the order parameter is

independent of position and restrict the series to the quartic terms. Then Eq. (44) reduces to:

$$\Psi(\eta) = \Psi_0 - \eta H + r_0 t\eta^2 + a_2\eta^4 \quad . \tag{45}$$

In order for the thermodynamic potential to be at a minimum, the following two conditions must be satisfied:

$$\left.\frac{\partial\Psi}{\partial\eta}\right| = 0$$
$$\left.\frac{\partial^2\Psi}{\partial\eta^2}\right| \geq 0 \quad . \tag{46}$$

Substituting Eq. (45) into these two conditions yields:

$$\begin{aligned} &2r_0 t\eta_0 + 4a_2\eta_0^3 - H = 0 \\ &2r_0 t + 12a_2\eta_0^2 \geq 0 \end{aligned} \quad . \tag{47}$$

In the absence of an external field (H=0), for the case t>0, the only real solution is $\eta_0 = 0$. When t<0, the solution is given by:

$$\eta_0 = \sqrt{r_0 / 2a_2}\sqrt{|t|} \quad . \tag{48}$$

The generalized susceptibility χ is determined as $\chi = -\frac{\partial^2\Psi}{\partial H^2} = \left.\frac{\partial\eta}{\partial H}\right|_{\eta=\eta_0}$. From Eqs. (47) and (48) one can obtain:

$$\chi = \begin{cases} \dfrac{1}{2r_0 t} & t > 0 \\ -\dfrac{1}{4r_0 t} & t < 0 \end{cases} \tag{49}$$

This is known as the Curie-Weiss law.

The last result we are interested in is the dependence of the order parameter on the external field. From Eq. (47), the order parameter at t=0 is

$$\eta_0 = \sqrt[3]{H/4a_2} \quad . \tag{50}$$

The specific heat is given by:

$$C = \begin{cases} 0, & t > 0 \\ 3r_0^2 k T_c^2 / 8a_2, & t < 0 \end{cases} \tag{51}$$

It is apparent that at the critical temperature, second-order derivatives of the thermodynamic potential are discontinuous. Moreover, the susceptibility diverges as $1/t$. Since this derivation was done without specifying the nature of H and η, these results can be generalized for every second-order phase transition considered within the framework of Landau theory.

It turns out that it is fluctuations that lead to the occurrence of the phase transition. As was mentioned before, Landau theory does not take into account such fluctuations. Nonetheless, the general idea about the divergence in second-order derivatives of the thermodynamic potential remains valid. The dependence of thermodynamic quantities upon value of t can be expressed as follows:

$$\begin{aligned} C &\propto |t|^{-\alpha} \\ \eta &\propto |t|^{\beta} \\ \chi &\propto |t|^{-\gamma} \\ \eta &\propto H^{1/\delta} \quad (t = 0) \\ \xi &\propto |t|^{-\nu} \end{aligned} \quad . \tag{52}$$

The parameters α, β, γ, δ, and ν are called *critical exponents*, and ξ is the *correlation length*. The critical exponents show great degree of universality, being the same for quite

different systems. In renormalization group theory, all phenomena are divided into universality classes depending on the values of the critical exponents.

In the present example the critical exponents are given by:

$$\alpha = 0;\ \beta = 1/2;\ \gamma = 1;\ \nu = 1/2;\ \delta = 3$$

3.2.5. Correlation function.

In the present section, the correlation function is related to the correlation length. A correlation function can be evaluated in the framework of Landau theory using the fluctuation-dissipation theorem (FDT). The correlation function is defined as:

$$g(\vec{\mathbf{r}},\vec{\mathbf{r}}') = \left\langle \left[\eta(\vec{\mathbf{r}}) - \langle\eta(\vec{\mathbf{r}})\rangle\right]\left[\eta(\vec{\mathbf{r}}') - \langle\eta(\vec{\mathbf{r}}')\rangle\right]\right\rangle \tag{53}$$

The fluctuation-dissipation theorem[11] states that:

$$\delta\langle\eta(\vec{\mathbf{r}})\rangle = \frac{1}{k_B T}\int d\vec{\mathbf{r}}' g(\vec{\mathbf{r}},\vec{\mathbf{r}}')\delta H(\vec{\mathbf{r}}') \tag{54}$$

if $\eta(\vec{\mathbf{r}})$ and $H(\vec{\mathbf{r}})$ are conjugate parameters. Using the most general form of expansion given in Eq. (44), we obtain the following equation for correlation function:

$$\left[2r_0 t + 12a_2\langle\eta(\vec{\mathbf{r}})\rangle^2 - c\nabla^2\right]g(\vec{\mathbf{r}},\vec{\mathbf{r}}') = k_B T\delta(\vec{\mathbf{r}} - \vec{\mathbf{r}}') \tag{55}$$

In the absence of an external field, the average value of the order parameter is given by Eq. (48) for t<0 and is zero for t>0. The solution for Eq. (55) in three dimensions is given by:

$$g(\vec{\mathbf{r}},\vec{\mathbf{r}}') = \frac{\exp\left(-|\vec{\mathbf{r}} - \vec{\mathbf{r}}'|/\xi\right)}{|\vec{\mathbf{r}} - \vec{\mathbf{r}}'|}\frac{k_B T}{4\pi c} \quad , \tag{56}$$

where ξ takes the form:

$$\xi = \begin{cases} (r_0 t)^{-1/2} & t > 0 \\ (-2r_0 t)^{-1/2} & t < 0 \end{cases} . \qquad (57)$$

Generally the correlation function is written in the so-called Ornstein-Zernike form[12]:

$$g(\vec{r}, \vec{r}\,') \propto \frac{\exp\left(-|\vec{r} - \vec{r}\,'|/\xi\right)}{|\vec{r} - \vec{r}\,'|^{p}} , \qquad (58)$$

where $p = d - 2 + \zeta$; d is the dimensionality of the system. Parameter ζ is another critical exponent and in three dimensions $\zeta = 0$.

3.2.6. Scaling hypothesis.

Since the nature of the order parameter in Landau theory was not specified, it must give the same critical exponents for *all* second-order phase transitions. This property is called *universality*. At the same time, it is now widely accepted that the fluctuations near the critical point provide the main mechanism for the second-order phase transitions, which Landau theory does not take into account. As the system approaches the critical point, the fluctuations grow larger and approach a macroscopic size. The hypothesis was made that in the vicinity of the critical point, the only relevant parameter is the correlation length, which describes the size of the fluctuations[13]. Then it follows that only two of the critical exponents are independent. The other exponents can be expressed in terms of these two, and such expressions are called "scaling laws":

$$\begin{aligned} &2 - \alpha = \nu d && \text{Fisher law} \\ &\gamma = \nu(2 - \zeta) && \text{Josephson law} \\ &\alpha + 2\beta + \gamma = 2 && \text{Rushbrooke law} \\ &\gamma = \beta(\delta - 1) && \text{Widom law} \end{aligned} \qquad (59)$$

At the critical point, the correlation length diverges and there is no characteristic distance relevant to the system. Suppose we take our system and divide it into cells in such a way that the size of a cell is much less than the correlation length near the critical point but much greater than the interparticle distance. In other words, $a \langle\langle L \langle\langle \xi$, where a is the interparticle distance and L is the cell size. Since the correlation length is the only important parameter, we can average all microscopic variables over any cell and obtain the same pattern as we had for original system. In other words, if we enlarge a given cell to the size of the system, it would resemble the whole system. The value $b = L/a$ is then called the *rescaling factor*. The parameters t and H are the only two that can change upon rescaling. We may write the transformation rule for these two variables:

$$\begin{aligned} \tilde{H} &= b^x H \\ \tilde{t} &= b^y t \end{aligned} \qquad (60)$$

All critical exponents can be expressed in terms of x and y. For the correlation length it immediately follows that $\nu = 1/y$. From Eq. (58) it follows that the correlation function scales as $b^{2-d-\zeta}$. Since the correlation function has the same dimension as η^2, we can conclude that η scales as $b^{(2-d-\zeta)/2}$. At the same time, since the order parameter is given by $\eta = \frac{\partial \varphi}{\partial H}$, it scales as b^{x-d}. Combining these two facts together, we obtain: $\zeta = 2 + d - 2x$. Now, using these expressions for ν and ζ, we can obtain all other critical exponents. Altogether, we obtain:

$$
\begin{aligned}
\nu &= 1/y \\
\alpha &= 2 - d/y \\
\beta &= \frac{d-x}{y} \\
\gamma &= \frac{2x-d}{y} \\
\delta &= \frac{x}{d-x} \\
\zeta &= 2 + d - 2x
\end{aligned}
\qquad . \qquad (61)
$$

It turns out that these scaling laws are also not, in general, correct. In this derivation, we completely ignored the microscopic picture and considered only averaged parameters without specific details about microscopic interactions. The theory that derives critical exponents from more basic principles and sets limits for the applicability of the scaling hypothesis is called *renormalization group theory* (RGT). A detailed description of RGT can be found in Ref. 14.

3.4. Incommensurate phases in dielectrics.

3.4.1. Phenomenological theory of incommensurate phases.

In the present work, we have observed phase transitions in organic molecular solids. Some of the phases are *incommensurate*. A comprehensive review of both theoretical and experimental work on dielectrics exhibiting incommensurate phase behavior can be found elsewhere[15]. In this work we present a brief overview of the general aspects of incommensurability, discussed in Ref. 15.

It is now generally accepted that an incommensurate phase is characterized by a lack of translational periodicity in at least one direction. However, this phase has three-dimensional long-range order, contrary to amorphous substances. In practice this means that the ratio of the periodicity of some order parameter (e.g., polarization or chemical composition) to the lattice periodicity is not a rational number. Incommensurate phases exhibit several interesting phenomena—nonlinear multi-soliton lattice-type ground state, phason excitation, devil's staircase, solid-state chaos, etc.—that are not found in translationally periodic systems.

In the simplest case the thermodynamic potential can be written as:

$$\Psi = \Psi_0 + \frac{A't}{2}\eta^2 + \frac{B}{4}\eta^4 + \frac{C}{2}\left(\frac{d\eta}{dx}\right)^2 + \frac{D}{2}\left(\frac{d^2\eta}{dx^2}\right)^2 \qquad (62)$$

The incommensurate modulation is in the x-direction. In Fourier form Eq. (62) becomes:

$$\begin{aligned}\tilde{\Psi} &= \tilde{\Psi}_0 + \frac{1}{2}\sum_k \left(A't + Ck^2 + Dk^4\right)\eta_k \eta_{-k} \\ &+ \frac{1}{4}B \sum_{k_1,k_2,k_3} \eta_{k_1}\eta_{k_2}\eta_{k_3}\eta_{-k_1-k_2-k_3}\end{aligned} \qquad (63)$$

At the transition to the incommensurate phase, the function $\tilde{A}(k) = A't + Ck^2 + Dk^4$ vanishes. Its minimum is located at the point $k_0^2 = -\frac{C}{2D}$. Thus the temperature of the incommensurate phase transition is defined by:

$$\tilde{A}(k_0) = 0 \quad , \qquad (64)$$

which yields

$$T_i = T_c\left(1 + \frac{C^2}{4DA'}\right) \quad . \qquad (65)$$

Other extrema for the functional (63) exist at k=0. They correspond to either the normal (highly symmetric) phase or commensurate low-symmetric phase. In the commensurate phase, $\eta(x) = \text{const}$ and Eq. (63) becomes:

$$\tilde{\Psi} = \tilde{\Psi}_0 - \frac{A'^2 t^2}{4B} \tag{66}$$

At the same time in the incommensurate phase we have (keeping only terms containing $\eta_{k_0}\eta_{-k_0}$):

$$\begin{aligned} \tilde{\Psi} &= \tilde{\Psi}_0 + A(k_0)\eta_{k_0}\eta_{-k_0} + \frac{3}{2}B\left(\eta_{k_0}\eta_{-k_0}\right)^2 \\ \tilde{\Psi}^{I}_{min} &= \tilde{\Psi}_0 - \left.\frac{A'^2 t^2}{6B}\right|_{T=T_i} \end{aligned} \tag{67}$$

When the thermodynamic potentials become equal, the system "locks" itself in the commensurate phase. The temperature of such "lock-in" transition is:

$$T_l = T_c\left[1 - \frac{C^2\left(\sqrt{6}+2\right)}{4DA'}\right] \tag{68}$$

In the example considered above, we have a one-component order parameter. Let us consider the more general case of the transition from one crystal lattice type into another. Our discussion now will follow that in Ref. 10. The crystal can be characterized by the electron density $\rho(\vec{r})$, which changes upon the phase transition. The symmetry of the crystal poses some restrictions on the function $\rho(\vec{r})$; namely, $\rho(\vec{r})$ should remain invariant under all symmetry transformations of the crystal space group. Thus we can always represent the density as a linear combination of the functions $\phi_i^{(n)}$:

$$\rho = \sum_n \sum_i \eta_i^{(n)} \phi_i^{(n)} \quad , \tag{69}$$

where n denotes the number of the irreducible representation, i is the number of the function in the basis for that representation.

The unit representation leaves all the functions invariant under all transformations and represents, therefore, the high-symmetry phase. Eq. (69) can be written as:

$$\rho = \rho_0 + \delta\rho = \rho_0 + \sum_n{}' \sum_i \eta_i^{(n)} \phi_i^{(n)} \quad , \tag{70}$$

where the prime indicates that the unit representation is excluded from the sum. At the transition point all the coefficients η_i must be zero. Therefore, the thermodynamic potential can be expanded near the phase transition point in powers of η_i. Since the thermodynamic potential must not depend on the coordinate system, it has to contain only the combination of η_i, which is invariant under group symmetry transformations. The linear invariant does not exist, therefore, to lowest order, this expansion is given by

$$\Psi = \Psi_0 + \sum_n{}' A^{(n)}(P,T) \sum_i \left(\eta_i^{(n)}\right)^2 \quad . \tag{71}$$

At the transition point, all $A^{(n)}$ values must be nonnegative in order for the potential to be minimal. At the same time, at least one of the $A^{(n)}$ values must change sign upon moving through the critical point, otherwise there would be no transition. For simplicity we can assume that only one coefficient $A^{(n)}$, corresponding to n^{th} irreducible representation, changes sign. The coefficients η_i, belonging to the same representation, also become nonzero. This means that the symmetry reduces upon the transition, so that the group of symmetry of the crystal below the transition point is the subgroup of the group of symmetry above the critical point. Since only n^{th} representation is important, the superscript n can be omitted and coefficients λ_i can be introduced as follows:

$$\eta^2 = \sum_i \eta_i^2; \quad \eta_i = \eta\lambda_i \tag{72}$$

where η is the "order parameter", analogous to the one introduced earlier [see Eq. (44)]. It gives the quantitative measure of the deviation from the high-symmetry phase. The set of coefficients λ_i represents the structure and the symmetry of the distorted (usually low-symmetry) phase. The expansion of the thermodynamic potential can be represented as follows:

$$\Psi = \Psi_0 + A(P,T)\eta^2 + \eta^4 \sum_j C_j(P,T) f_j^{(4)}(\lambda_i) + \cdots \tag{73}$$

where $f_j^{(4)}(\lambda_i)$ is the invariant of the fourth order that can be constructed from the coefficients λ_i. The sum over j extends over all possible invariants of the fourth order. At the transition point, the coefficient A must be zero. The set of all η_i plays the role of the order parameter in this theory.

In the case of two-dimensional order parameter, we must also include in Eq. (73) the invariants constructed from the derivatives of η_i. The expansion must contain terms proportional to $|\nabla\eta_i|^2$, as well as terms of the form $\eta_i \frac{\partial\eta_k}{\partial x} - \eta_k \frac{\partial\eta_i}{\partial x}$ for certain symmetry groups. The requirement on these antisymmetric combinations is that one can not construct vector components from those quantities. The term, containing those antisymmetric combinations is called the *Lifshitz invariant*. The presence of the Lifshitz invariant introduces spatial inhomogeneity and this is what is now called the incommensurate phase. With the Lifshitz invariant, the consideration and all general results remain the same.

3.4.2. Microscopic theory of incommensurate phase.

It has long been realized that in a system, where different interactions between atoms favor different configurations, an incommensurate phase may be expected to form. One of the microscopic models with competing interactions is the ϕ^4 model. In this model the potential can be written as:

$$V = \sum_n \left[\frac{A}{2}(u_n - u_{n-1})^2 + \frac{B}{4}(u_n - u_{n-1})^4 + \frac{C}{2}(u_n - u_{n-2})^2 + \frac{D}{2}(u_n - u_{n-3})^2 + P(u_n - u_{n-1}) \right], \quad (74)$$

where u_n denotes the displacement of the n^{th} atom in a linear chain with spacing a. Thus the position of this atom is $n \cdot a + u_n$. In the case of negative A, Eq. (74) describes a double-well potential. The interactions up to third-neighbor are taken into account by the third and the fourth terms. The last term accounts for the influence of pressure.

We can redefine the Hamiltonian by replacing u_n by $\sqrt{|C|/B}\,u_n$ and V by $B|C|^2 V$. In the new Hamiltonian, B=1 and $\tilde{C} = C/|C| = \pm 1$.

$$\tilde{V} = \sum_n \left[\frac{\tilde{A}}{2}(u_n - u_{n-1})^2 + \frac{1}{4}(u_n - u_{n-1})^4 + \frac{\tilde{C}}{2}(u_n - u_{n-2})^2 + \frac{\tilde{D}}{2}(u_n - u_{n-3})^2 + \tilde{P}(u_n - u_{n-1}) \right], \quad (75)$$

where $\tilde{A} = A/|C|$, $\tilde{D} = D/|C|$, and $\tilde{P} = P/|C|$.

Replacing u_n-u_{n-1} by x_n, we can obtain the following equilibrium condition for the system:

$$\left(\tilde{A}+2\tilde{C}+3\tilde{D}\right)x_n+x_n^3+\left(\tilde{C}+2\tilde{D}\right)\left(x_{n-1}+x_{n+1}\right)+\tilde{D}\left(x_{n-2}+x_{n+2}\right)=\text{const} \tag{76}$$

Apart from the trivial solution ($x_n=0$) one can obtain two more solutions:

$$x_n=l,\qquad l^2=-\left(\tilde{A}+4\tilde{C}+9\tilde{D}\right) \tag{77}$$

and

$$x_n=(-1)^n l,\qquad l^2=-\left(\tilde{A}+\tilde{D}\right) \tag{78}$$

The stability of all possible equilibrium configurations depends on the sign of the second derivative. The stability condition implies that the eigenvalues of the matrix

$$\Omega_{nm}=\left.\frac{\partial^2 V}{\partial x_n \partial x_m}\right|_{x=x^0}$$

at the equilibrium configuration x^0 are non-negative. For the trivial solution, the eigenvalue equation is given by:

$$m\omega^2=\sin^2\left(\frac{1}{2}k\right)\left[A+4C\cos^2\left(\frac{1}{2}k\right)+D\left(4\cos^2\left(\frac{1}{2}k\right)-1\right)^2\right] \tag{79}$$

It is clear that for arbitrary values of parameters, the right-hand side of Eq. (79) can become negative. In that case, the trivial solution loses stability, which means that the system transforms into another stable state. The critical wave vector for such a transformation is given by:

$$\cos(k_c a)=-\frac{C+2D}{4D} \tag{80}$$

For C=1, D must be greater than 1/2, and for C=-1, D is greater than 1/6. The new ground state, with period $2\pi/k_c$ is stabilized by the nonlinear terms in Eq. (74).

Another popular model, which also exhibits features of incommensurability, is the Frenkel-Kontorova model. In this model the linear chain of atoms is set in a periodic background potential and the atom-atom interaction is harmonic.

$$V_{FK} = \sum_n \left[\frac{1}{2}\left(x_n - x_{n-1} - d\right)^2 + \frac{\lambda}{2}\left(1 - \cos\left(\frac{2\pi x_n}{a} + \nu\right)\right)\right] \qquad (81)$$

A detailed discussion of this model can be found elsewhere[16,17,18].

4. Conjugated molecules.

In this Section we review the fundamental properties and applications of organic conjugated molecules. Since the conjugated molecules which we investigated are used in organic laser dyes and light-emitting devices, in the first subchapter particular emphasis will be placed on the functioning of those devices and physical principles behind their operation. In subsequent subsections we review some of the results of research on those molecules.

4.1. Organic laser dyes and light-emitting devices (OLED).

4.1.1. Organic dyes.

Organic laser dyes, used as the active medium for tunable lasers, contain organic molecules that absorb over a broad range of the spectrum and exhibit strong luminescence[19]. A schematic diagram of energy levels of an organic dye molecule is presented in Fig. 5. Electronic states with total spin equal to zero are called singlet states and those with a total spin of one are called triplet states. S_0-S_2 are the singlet states and T_1 and T_2 are triplet states. The electronic states have fine vibrational-rotational structure. An excitation populates the S_1 states and, after nonradiative relaxation to the bottom level, the excited molecules spontaneously emit a photon and decay to a state in S_0. Some electrons, however, are excited to higher electronic states or decay to T_1 states, from

which they can again be excited to T_2 states. These absorption processes quench the laser radiation.

Since the organic molecules absorb and emit over a wide range of wavelengths, they are extremely useful for tunable lasers, in which the lasing wavelength can be changed continuously. This is done by inserting a wave selective device, such as a grating or prism, into the laser resonator. It is immediately evident that any change of the energy levels can result in a dramatic change in the performance of these molecules as laser dyes. Such changes can be caused by inducing transitions between possible molecular conformations.

4.1.2. Organic light-emitting devices (OLEDs).

Another rapidly growing application of organic compounds is organic light-emitting devices (OLEDs)[20]. In a light-emitting device, the active layer is sandwiched between two electrodes, an anode that injects holes and a cathode that injects electrons. An electron and a hole meet in the active layer, and an exciton is formed. This exciton decays radiatively and light is emitted. This phenomenon is known as electroluminescence, since an applied electric field is used to introduce charges into the active layer. One of the electrodes (usually the anode) is made transparent to allow the light to escape the device (Fig. 6). The wavelength of the emitted light is determined by the energy difference between the highest occupied molecular orbital (HOMO) and the lowest unoccupied molecular orbital (LUMO) of the active layer.

The first materials used in light-emitting devices were inorganic compounds such as gallium arsenide. Recently, certain organic compounds have emerged as candidates for optoelectronic applications. These molecules have delocalized π-orbitals which enable them to transport charge. In order to serve as an active layer in an LED, the molecule must also have significant overlap between its π-orbitals and those of neighboring molecules. This overlap allows the charge to be transported in three dimensions. Suitable compounds include poly(phenylene-vinylene) or PPV, tris(8-hydroxyquinolinato)aluminium or Alq_3, pentacene, and regioregular poly(3-hexylthiophene)[21]. The difference between HOMO and LUMO energy levels in these molecules is analogous to the band gap in conventional semiconductors.

In order to increase performance, the active layer is typically split into two layers. One material is used as the hole transport layer and the other is used as the electron transport layer. The electrodes are chosen to have a low work function for the anode and a high work function for the cathode. The respective work functions should match the electron affinity and ionization potential for active layers[22].

The internal quantum efficiency of the LED is defined as the ratio of the number of photons produced to the number of electrons flowing in the external circuit:

$$\eta_{int} = \gamma r_{st} q \quad , \tag{82}$$

where γ is the ratio of the number of exciton formation events to the number of electrons flowing in the external circuit, r_{st} is the fraction of excitons formed as singlets, and q is the efficiency of radiative decay of those excitons. It is therefore necessary to achieve a good balance between electron and hole currents, efficient capture of electrons and holes in the emissive layer, and efficient radiative decay of singlet excitons.

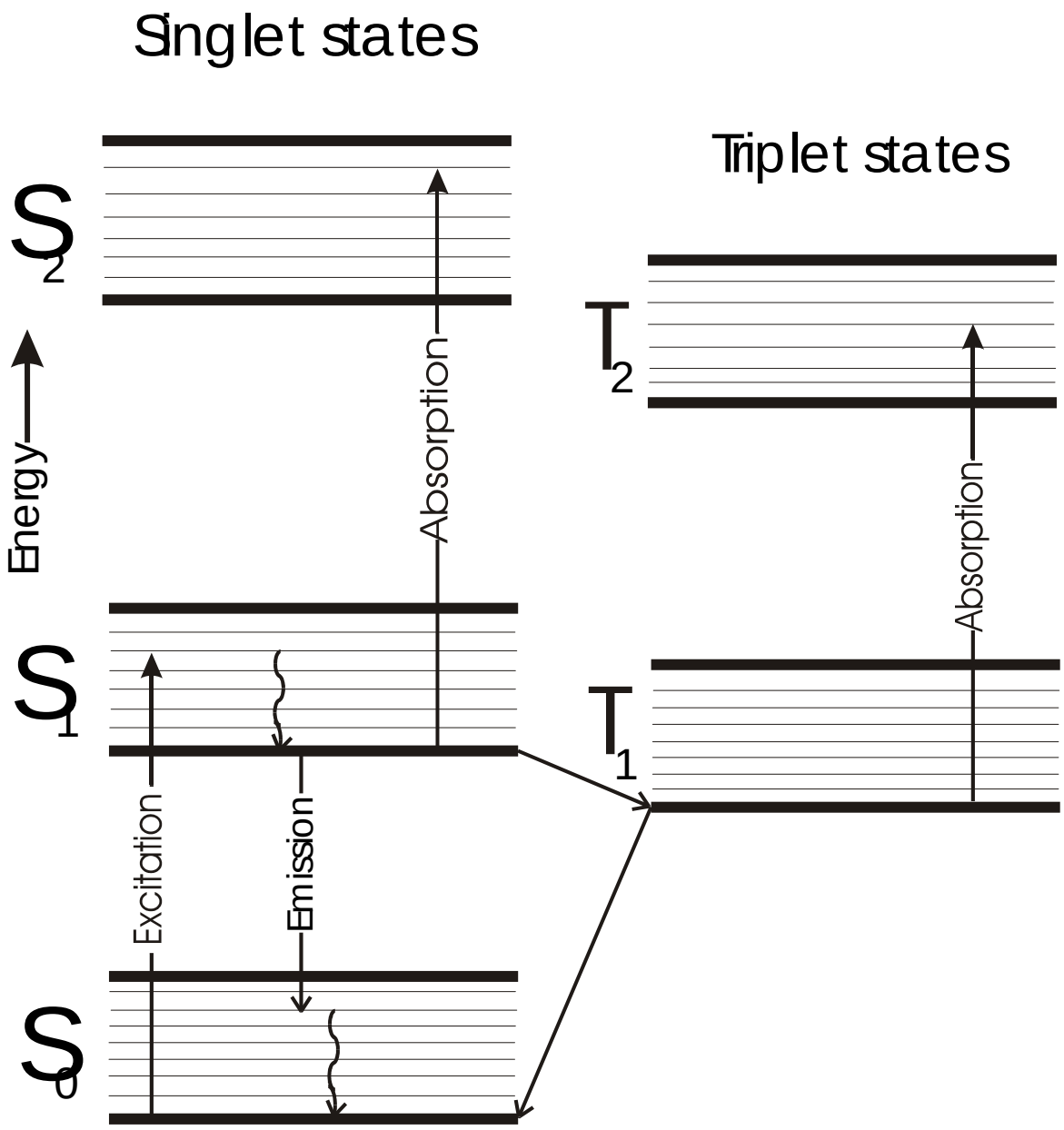

Figure 5. Schematic representation of the energy levels and electronic transitions of an organic molecule used in laser dyes.

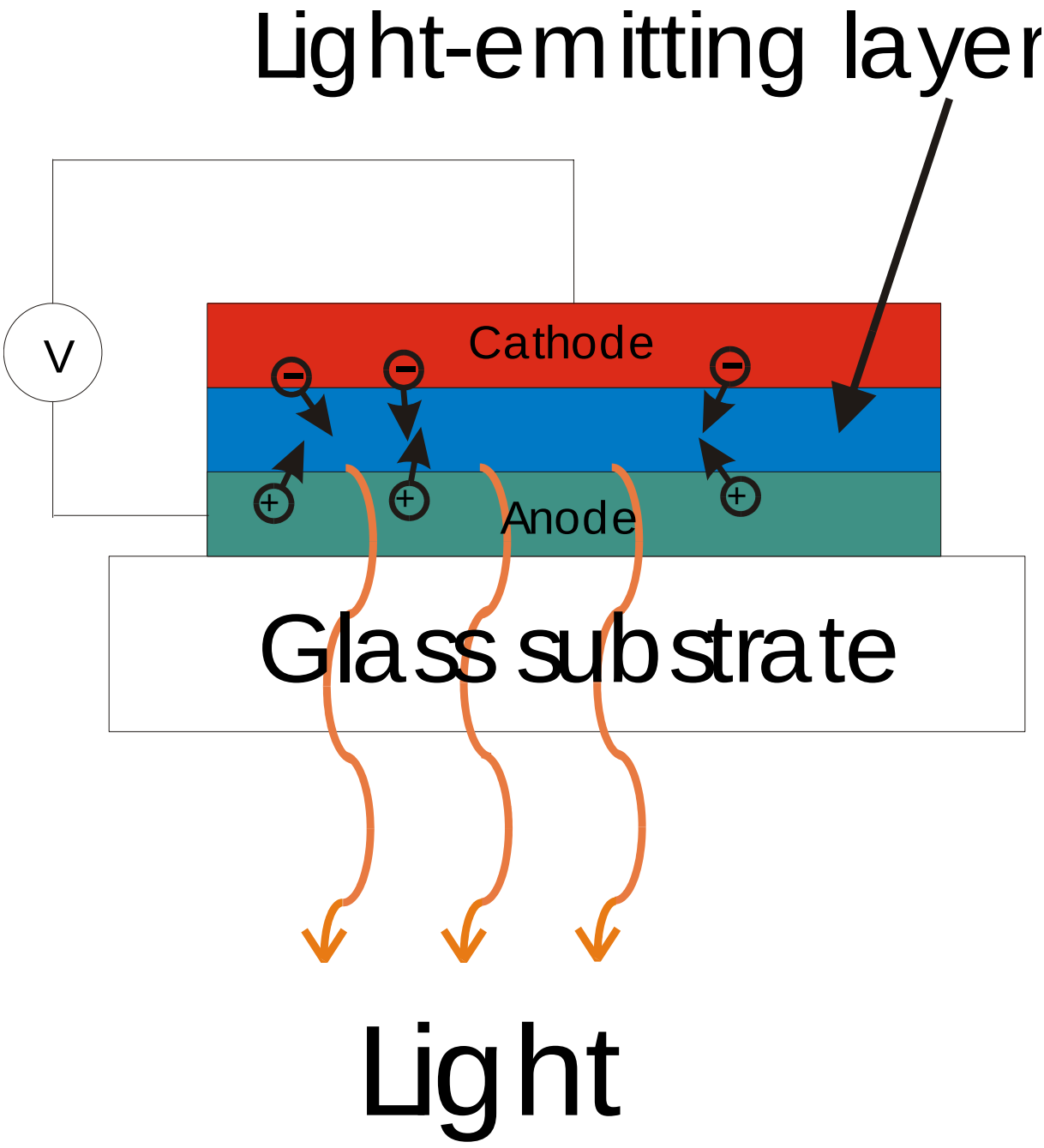

Figure 6. Design of the light-emitting device (LED).

One of the attractive features of OLED is that the color of emission can be controlled by altering the chemical structure of the polymer film. Different side groups can work to shift the emission both to the red and to the blue part of the visible spectrum.

The electrical characteristics of the single-layer devices are hard to model. The typical current density-voltage characteristic resembles that of a diode. For PPV with Al and indium-tin oxide (ITO) electrodes, for example, the majority of the current is expected to be due to the holes. The formula relating current density J and voltage V is given by:

$$J = J_0\left[\exp\left(\frac{qV}{nkT}\right) - 1\right] \quad , \tag{83}$$

q is the carrier charge here. This formula, however, works best at voltages between 1 and 2 V and with n ranging from 1.8 to 2.4, compared to n=1 in the ideal case.

The OLEDs, especially multilayer devices, are quite complicated optical systems. Their optical output is determined by many factors, including interference effects between light taking different optical paths within the device. In the simplest model of LED with isotropically oriented emitting dipoles the total amount of light produced, F_{total}, is related to the light output per unit solid angle in the forward direction, L_0, as follows:

$$F_{total} = 2\pi n^2 L_0 \tag{84}$$

In the other limiting case, when all the dipoles are aligned within the plane of the film, the emission is more preferably in the forward direction:

$$F_{total} = \pi n^2 L_0 \tag{85}$$

It should be mentioned that the presence of interfaces affect not only the angular distribution of the light emitted, but also the radiative lifetime. For a more detailed

analysis the reader is referred to the references given in the review by Greenham and Friend (Ref. 20).

The simplest model for organic diodes includes the charge transport equations coupled with Poisson's equation:

$$\left.\begin{aligned} \frac{\partial n}{\partial t} - \frac{1}{e}\frac{\partial J_n}{\partial x} &= G - R \\ \frac{\partial p}{\partial t} + \frac{1}{e}\frac{\partial J_p}{\partial x} &= G - R \\ \frac{\partial E}{\partial x} &= \frac{4\pi e}{\varepsilon}(p - n) \end{aligned}\right\} \tag{86}$$

where the current densities are written in the form:

$$\left.\begin{aligned} J_n &= e\mu_n\left(nE + \frac{kT}{e}\frac{\partial n}{\partial x}\right) \\ J_p &= e\mu_p\left(pE - \frac{kT}{e}\frac{\partial p}{\partial x}\right) \end{aligned}\right\} \tag{87}$$

In these equations n(p) is the electron (hole) density, J_n (J_p) is the electron (hole) current density, μ_n (μ_p) is the electron (hole) mobility, G (R) is the carrier generation (recombination) rate, E is the electric field, e is the magnitude of the electron charge, ε is the static dielectric constant, and T is the temperature. The model is one-dimensional because of the geometry of the device. The carrier mobilities are, in general, field dependent. Their dependence is described by the Poole-Frenkel form[23]:

$$\mu = \mu_0 \exp\left(\sqrt{\frac{E}{E_0}}\right) \tag{88}$$

The electron-hole recombination is bimolecular, i.e. $R = \gamma(np)$. For the recombination coefficient, a Langevin form is often used:

$$\gamma = \frac{4\pi e \mu_m}{\varepsilon}$$

where μ_m is the larger of two mobilities. The generation rate is determined from the detailed balance equation, $G = \gamma(n_e p_e)$, where $(n_e p_e)$ is the product of equilibrium electron and hole concentrations. For a more detailed discussion the reader is referred to the Ref. 23 and references therein.

4.2. Conjugated molecules and their investigation.

4.2.1. Introduction.

As was mentioned in the previous section, molecules which have π-bonds in addition to σ-bonds exhibit the ability to transport charge. Those molecules have delocalized electrons due to the overlap of π-orbitals and are useful in applications such as OLEDs[24]. Such molecules are called *conjugated molecules*. The overlap of π-orbitals significantly affects their optical properties. If the overlap increases (for example, due to application of pressure), the bandgap is red-shifted.

In their final form, the conjugated polymer molecules tend to be rigid molecules, insoluble in common organic solvents. Therefore it is difficult to synthesize those molecules directly, because the product will precipitate from the solution while its molecular weight is still small. The final product is then difficult to form into the thin film needed for the electronic devices. A number of methods have been developed to overcome these problems. The most common one is a "precursor route" method, where a

soluble "precursor" polymer is prepared and processed to form a thin film. After this step, further processing converts this film into the final polymer film.

The real polymers contain various defects, which break conjugation. These defects highly affect the electronic properties of a conjugated polymer and, in turn, are strongly dependent on the synthetic route and processing technique. The average number of repeated units between conjugation-breaking defects is called the conjugation length.

Polyphenyls are one type of conjugated molecules. They consist of two or more phenyl rings connected to each other via single C-C bonds. It was recognized long ago (Ref. 27) that the rings in these molecules are free to rotate around the C-C bond. There are several possible conformations that these molecules may have. One is the planar conformation, where all the rings are in the same plane. Other conformations involve all possible ring twists around the C-C bonds. For the simplest molecule of that type, biphenyl, there is only one twisted conformation, with the planes of the rings being at some nonzero angle with respect to each other. For p-terphenyl, p-quaterphenyl, and other molecules with larger numbers of rings, there exist several possible twisted conformations.

Now it is widely accepted that the conformation of any polyphenyl molecule is a result of the balance between the electrostatic repulsion of hydrogen atoms, which tends to twist the rings, and the interaction between π-electrons, which tends to planarize the molecule[25,26]. In the solid state there is also an intermolecular packing force, which favors the planar conformation. The outcome of the competition between these forces determines the molecular structure.

The first experimental evidence that biphenyl molecules are twisted in the gas phase was obtained in 1949[27]. Since then, many investigations have been undertaken to analyze not only biphenyl, but also higher-order polyphenyl molecules.

4.2.2. Biphenyl.

The biphenyl molecule ($C_{12}H_{10}$) consists of two phenyl rings connected by a single C-C bond. In the gas phase, it is twisted, with the angle between ring planes approximately 40°[27]. In the crystal phase, the molecule was determined to be planar[28] at room temperature. When the temperature is lowered, the structural transition to phase II occurs at T=40 K, and the molecule becomes twisted[29]. Another phase transition, to phase III, occurs at T=17 K. These phase transitions were studied by neutron diffraction[30], neutron scattering[31], Brillouin scattering[32], X-ray[33], nuclear magnetic resonance (NMR)[34], electron paramagnetic resonance(EPR)[35], and Raman scattering[36]. The schematic phase diagram is shown in Fig. 7.

The two twisted phases of biphenyl are said to be incommensurate, which means that the twist angle is modulated along the crystal structure. The change in the twist angle can be expressed as follows[31]:

$$\phi(\mathbf{r}) = A_1 \cos(\mathbf{q}_{s_1} \cdot \mathbf{r} + \Phi_1) + A_2 \cos(\mathbf{q}_{s_2} \cdot \mathbf{r} + \Phi_2) \qquad (89)$$

where $\mathbf{q}_{s_1}$ and $\mathbf{q}_{s_2}$ are modulation vectors, A_1 and A_2 are amplitudes, and Φ_1 and Φ_2 are phases. The modulation vectors are related to the reciprocal lattice vectors ($\mathbf{a}^*$, $\mathbf{b}^*$, $\mathbf{c}^*$) by:

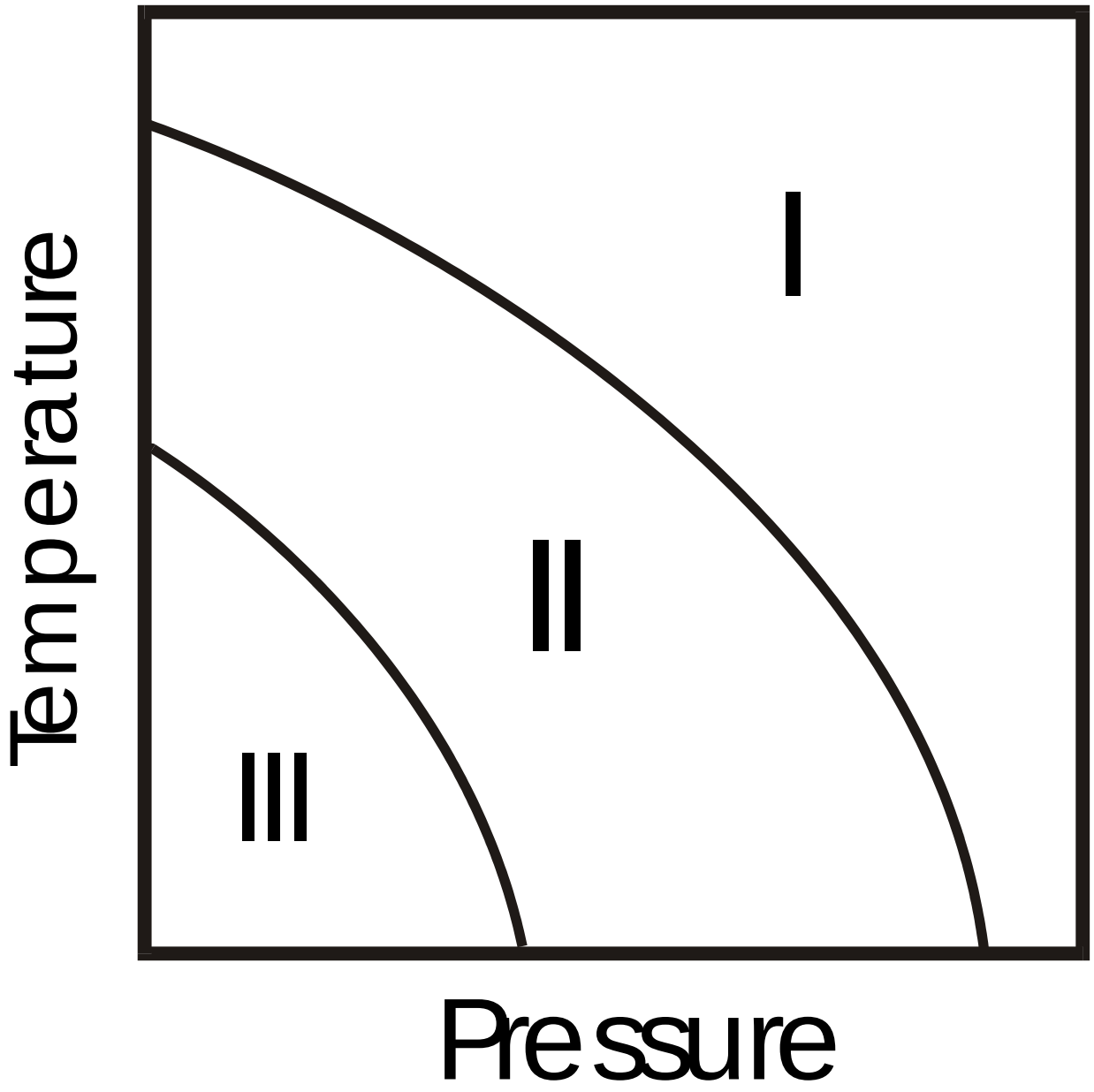

Figure. 7. Schematic phase diagram of biphenyl.

$$\left.\begin{aligned} \mathbf{q}_{s_1} &= \delta_a \mathbf{a}^* + \frac{1-\delta_b}{2}\mathbf{b}^* - \delta_c \mathbf{c}^* \\ \mathbf{q}_{s_2} &= -\delta_a \mathbf{a}^* + \frac{1-\delta_b}{2}\mathbf{b}^* + \delta_c \mathbf{c}^* \end{aligned}\right\} \qquad (90)$$

for phase II. In phase III, $\delta_a = \delta_c = 0$ so that the two modulation vectors coincide with each other[32,37].

Biphenyl has been studied very extensively over the past twenty-five years. The phase transition is governed by a double-well potential, which is a result of the balance between different forces, which was described earlier (Fig. 8). At low pressure the intramolecular potential is stronger and the total potential has two minima. When pressure increases, the crystal packing force prevails and the two minima merge to give rise to a parabolic type of potential. The phase transition is of displacive type and is characterized by a soft mode (see, for example, Ref. 38). A number of models have been developed to describe the phase transition and incommensurability of the twisted phases of biphenyl. In Ref. 39 the phase transition was induced by the coupling between the soft torsional mode and acoustic phonon. A similar model was developed in Ref. 40, but the effect of pressure was also included. In both cases the intra-molecular potential was represented as:

$$V_{intra} = -\frac{A}{2}\varphi^2 + \frac{B}{4}\varphi^4 \quad , \qquad (91)$$

where A and B are constants and φ is the twist angle of one ring (the total twist is 2φ). The intermolecular potential tends to planarize molecules and can be written as:

$$V_{inter} = \sum_i L\varphi_i^2 + \sum_{i \neq j} K_{ij}\varphi_i\varphi_j \quad , \qquad (92)$$

where i and j indicate lattice sites. The total potential is given by:

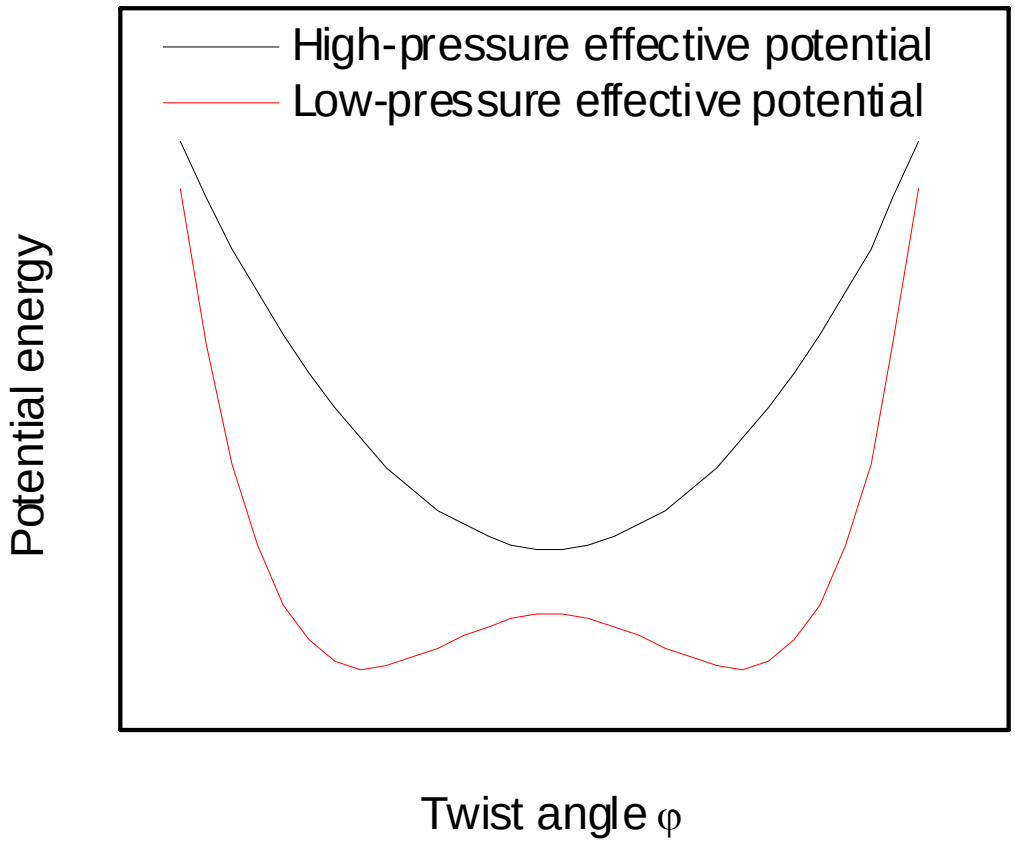

Figure 8. Effective molecular potential at low and high pressures.

$$V_{tot} = \sum_i -\frac{A'}{2}\varphi_i^2 + \frac{B}{4}\varphi_i^4 + \sum_{i\neq j} K_{ij}\varphi_i\varphi_j \quad , \qquad (93)$$

where $A' = A - 2L$. The last term describes the coupling between different molecules. The summations extend over all molecules in the crystal. This model is similar to the ϕ^4-model, which was described earlier, and it allows for the incommensurate ground state to exist.

A further simplification arises when one assumes a quasi-one-dimensional modulation along one of the axes, namely $\mathbf{b}^*$. The potential then looks similar to that in Eq. (74):

$$V_{tot} = \sum_m \frac{1}{4}B\varphi_m^4 - \frac{1}{2}A'\varphi_m^2 + \frac{1}{2}K_0\varphi_m^2 + 2K_1\varphi_m\varphi_{m+1} + K_2\varphi_m\varphi_{m+2} \qquad (94)$$

Using this potential, the transition temperature was determined by mean-field theory for both biphenyl and p-terphenyl[41].

In Ref. 42, the Williams type of atom-atom potential[43] was used to model the molecular dymanics of biphenyl. The developed structure, however, is different from the X-ray experimental results. Recently a number of *ab initio* calculations have been performed in order to determine the torsional barriers and other properties of biphenyl[44,45,46].

4.2.3. P-terphenyl.

The p-terphenyl molecule is similar to biphenyl. P-terphenyl undergoes a structural phase transition at 193 K, below which point the molecule becomes non-planar. In the planar conformation it has D_{2h} symmetry. Since this molecule contains three

phenyl rings, there are several possible models for the non-planar structure. In Ref. 47, it was shown by x-ray diffraction that the central ring becomes twisted, with twist angles of 16 and 25° with respect to external ones. This molecule possesses C_{2h} symmetry. As with biphenyl, p-terphenyl has an incommensurate phase, such that twist angle is modulated throughout the crystal. Unlike biphenyl, however, the p-terphenyl molecule preserves its center of symmetry upon the phase transition. The rotational disorder in the incommensurate phase was explained by considering non-bonded interactions[48], using the Williams-type of potential[49]. The temperature-induced phase transition was studied by fluorescence emission[50], Raman scattering[51,52,53], Brillouin scattering[54], NMR[55], EPR[56], and by infrared (IR) spectroscopy[57]. It was shown in Refs. 52 and 57 that certain Raman and IR peaks disappear upon the phase transition, when the temperature is raised above the critical point.

A number of theoretical investigations have been carried out to determine the structure of the p-terphenyl molecule. In Ref. 58 semi-empirical calculations, using the INDO-type method[59], have shown that the p-terphenyl molecule has two nearly isoenergetic isomers of D_2 and C_{2h} symmetries, with D_2 being slightly more stable than C_{2h}. Akiyama[60] has determined, using similar methods, that p-terphenyl in solution has C_2 symmetry. In Ref. 64, p-terphenyl was studied in a carbon disulfide solution, and the analysis of infrared band intensities led the authors to conclude that the conformation in solution has D_2 symmetry. This conclusion contradicted the theoretical results of Akiyama (Ref. 60). A conformational analysis of various isomers of p-terphenyl by photoelectron spectroscopy has also been performed[61,62]. It was found that p-terphenyl in

the gas phase has twisted conformation, with twist angle of about 42°, whereas in the solid state at room temperature it is planar.

It is evident that hydrostatic pressure provides an excellent tool for studying phase transitions, especially those which involve a balance between inter- and intramolecular forces. Pressure shifts this balance by increasing the intermolecular forces. At low temperatures and pressures, the polyphenyl molecule is in its twisted conformation. As pressure increases, it goes through a phase transition and becomes planar. The influence of pressure on the conformation of p-terphenyl has been studied by Raman scattering[63], infrared absorption[64], and optical absorption[65]. The observed changes in the spectra clearly indicated the presence of a phase transition.

4.2.4. P-quaterphenyl.

The p-quaterphenyl molecule resembles biphenyl and p-terphenyl in its behavior. This compound is planar at room temperature and undergoes a phase transition at T=243 K, when the molecule becomes twisted. Similarly, the molecule planarizes when the pressure is increased. Analogously to biphenyl, this molecule loses its center of inversion symmetry upon the phase transition. The symmetry group in the low-pressure and low-temperature phase is D_2. Quaterphenyl was also investigated by different techniques mentioned earlier for biphenyl and p-terphenyl, but not as extensively[96,52,66].

5. Experimental methods.

In this Section we review devices used in high-pressure research and Fourier-transform infrared spectroscopy, methods of achieving high pressure, pressure monitoring, infrared spectroscopy techniques, and advantages of Fourier-transform spectroscopy compared to other spectroscopic methods.

5.1. High-pressure apparatus.

5.1.1. Diamond-anvil cells.

The experimental task to achieve very high pressures has been a major challenge for scientists. The invention of the diamond anvil cell (DAC) provided an extremely powerful tool for reaching pressures in the megabar region (1 megabar=10^6 atm=10^3 kbar=100 GPa). The first DAC is attributed to the work of Lawson and Tang[67], who used a diamond to achieve high pressures for x-ray diffraction studies. A decade later, two other versions of DACs appeared independently[68,69] and the DAC has been widely used in high-pressure physics ever since.

Here I present a review of DACs and their applications to high-pressure research, following the review given by Jayaraman[70].

There are several types of DACs, among which five major types are distinguished. They are the National Bureau of Standards cell, Bassett cell, Mao-Bell cell, Syassen-Holzapfer cell, and Merrill Bassett cell. These cells are shown in Fig. 9-13 [70].

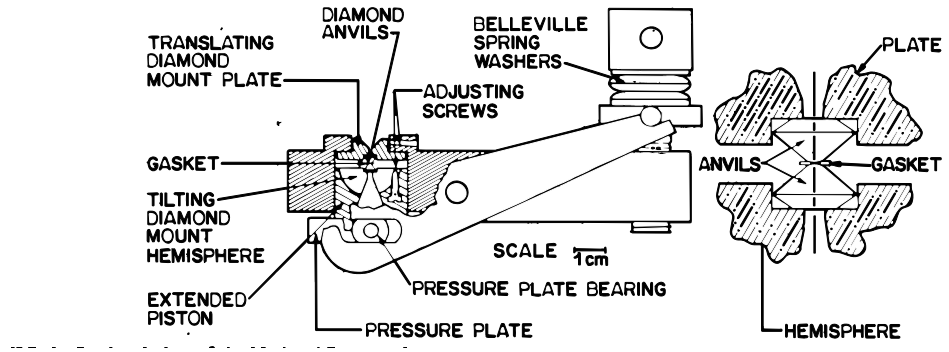

Figure 9. Schematic picture of the National Bureau of Standards (NBS) diamond-anvil cell (DAC) design[71].

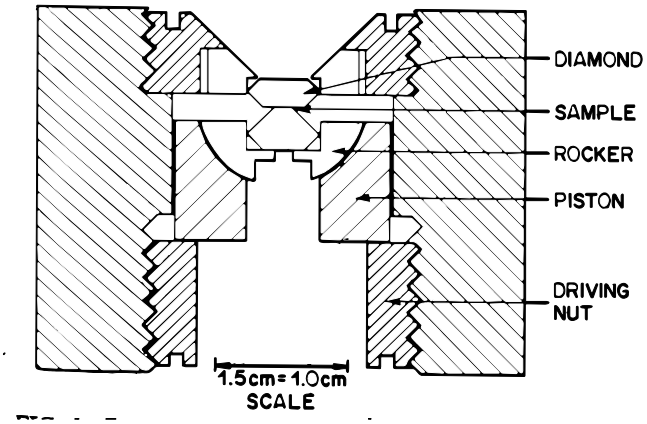

Figure 10. Schematic picture of the Bassett diamond-anvil cell (DAC) design[72].

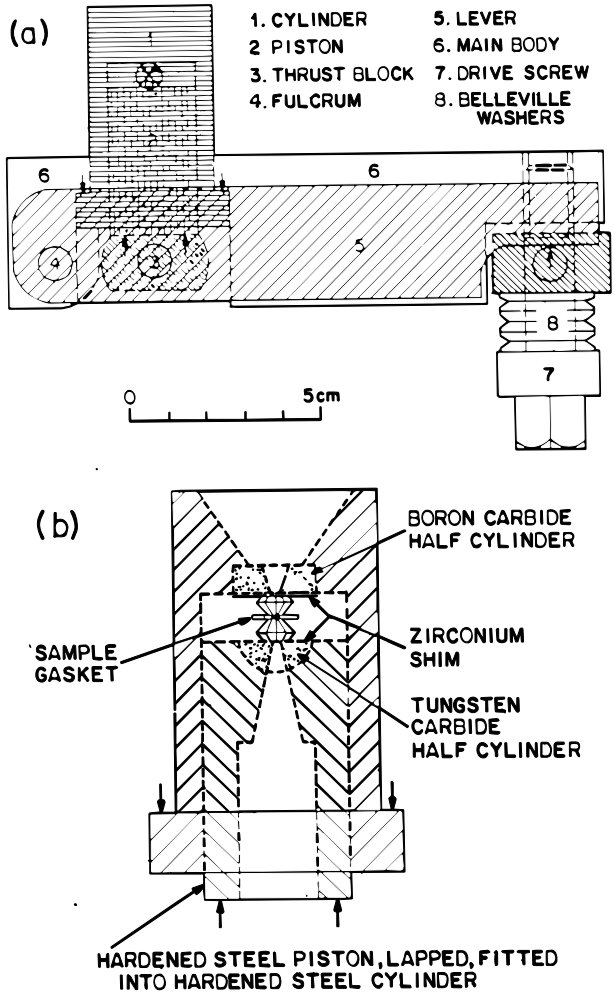

Figure 11. Schematic picture of the Mao-Bell diamond-anvil cell (DAC) design [73].

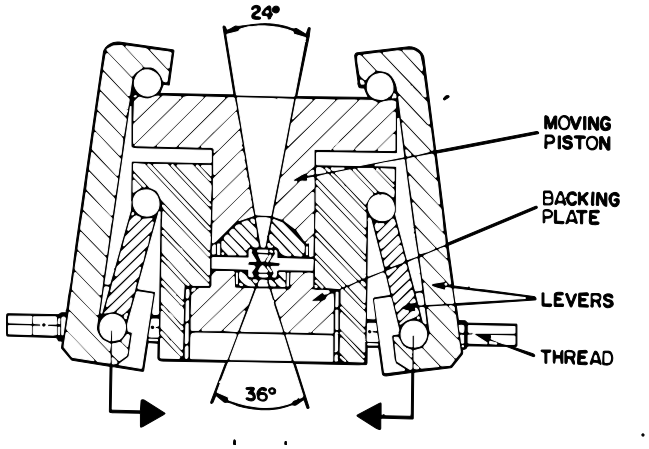

Figure 12. Schematic picture of the Syassen-Holzapfer diamond-anvil cell (DAC) design [74].

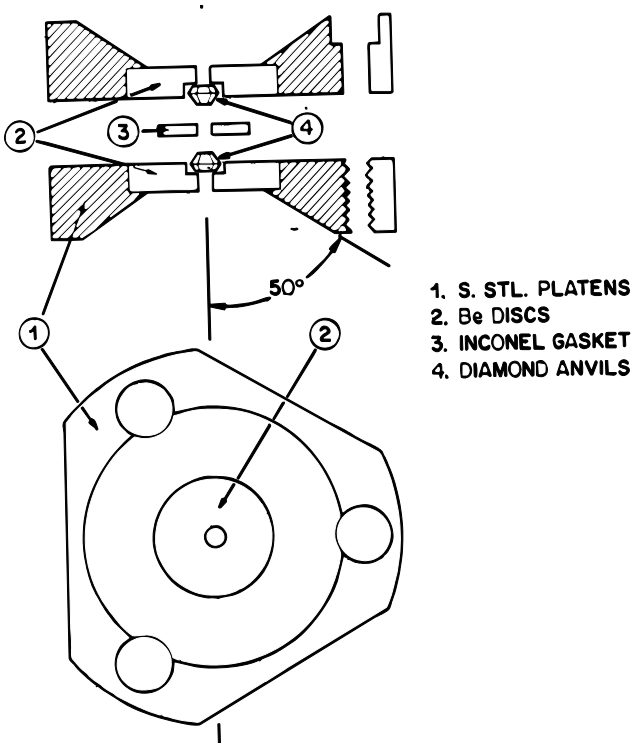

Figure 13. Schematic picture of the Merill-Bassett diamond-anvil cell (DAC) design [75].

All these cells use diamonds as anvils. The sample is placed between two flat surfaces of the diamonds and the force is applied to push the diamonds together. Since the areas of the diamond surfaces are small, a DAC is usually capable of achieving a pressure of hundreds of kbar. The Mao-Bell cell is superior to the other types of cells, being able to reach pressures up to several megabar. The diamonds have a typical size of 1/8 to ½ carat with an anvil flat (culet) diameter ranging from 0.3 to 0.7 mm. The diamonds are shaped in the forms of octagons or polygons with as many as 16 sides. The surface opposite to the culet is of 2 to 5 mm in diameter. Generally, larger diamonds are preferred for larger pressures.

The metal gasket for the DAC was first introduced in 1965 (Ref. 76). The gasket is preindented by the culets to a thickness of 0.05 to 0.2 mm. A hole is then drilled in the center of the indentation and the sample of interest is put in the hole, together with a ruby chip for pressure calibration. A pressure-transmitting fluid is also placed in the hole to provide hydrostatic pressure. In addition to confining the sample, the gasket provides support to the diamonds. Beveling of the edges of the anvils is required for megabar pressures.

Pressure calibration in the DAC is made via the ruby fluorescence method[77,78]. This calibration technique uses the ruby fluorescence lines, which at atmospheric pressure are at 692.7 and 694.2 nm. These lines shift linearly with pressure up to 200 kbar[79]. For higher pressures, a correction is required due to the nonlinearity of the shifts. The following formula has been proposed for the pressure determination[80]:

$$P = 3808\left[\left(\Delta\lambda/\lambda + 1\right)^5 - 1\right] \quad , \qquad (95)$$

where P is in kbar and $\Delta\lambda/\lambda$ is the fractional shift in wavelength. Ruby fluorescence has been the preferred pressure calibration method for the past twenty five years.

Many fluids are suitable for providing hydrostatic pressure. The range of pressures at which the liquid has hydrostatic behavior varies from 90 kbar for argon to more than 600 kbar for helium and hydrogen. In Table II, data for several pressure-transmitting liquids are summarized.

Diamond-anvil cells have long been used for spectroscopy. The transparency of diamond, over a wide spectral range, makes it a very useful material for high-pressure spectroscopy. However, the culet size of the diamonds is small, and the gasketing reduces the working space even further. As a result, one has to deal with tiny apertures of about 0.3 mm in diameter. This drastically reduces the signal from the detector. In general, the researcher has to focus the light onto the sample and bring the detector as close to the sample as possible.

In the present experiments, a piston-cylinder DAC was used. The alignment system consists of three screws to adjust the orientation for the diamond mounted on the hemispherical backing plate. Three other screws are used to adjust the translational alignment of the other diamond. The pressure is provided by tightening six Allen screws placed at the corners of a regular hexagon, as viewed along the axis of the cell. The piston has a polished cone that helps to focus the light onto the sample. The detector is located at the opposite side of the top diamond. The whole assembly is attached to the sample holder and the parabolical mirror is used to focus the light onto the sample (Fig. 14).

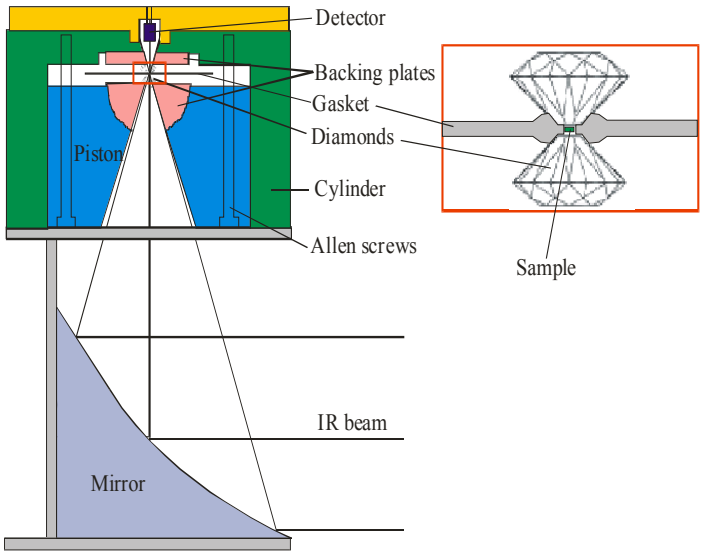

Figure 14. Schematic representation of the low-temperature high-pressure IR-spectroscopy device.

Table II. Some pressure media and their pressure ranges (Ref. 70).

Medium	Freezing pressure at RT (kbar)	Pressure range of hydrostatic behavior (kbar)	Comments
Methanol:ethanol 4:1	104	~200	Easy filling
Methanol:ethanol: Water 16:3:1	145	~200	″
He	118	>600	Cryogenic or high-pressure filling
Ne	47	160	″
Ar	12	90	″
Xe	--	300	Cooling below 165 K needed
H_2	57	>600	Cryogenic or high-pressure filling
D_2	53 ± 2	--	″
N_2	24	130	Cryogenic filling
O_2	59	--	″

The sample holder is placed into the cryostat, where the low-temperature measurements are performed. The DAC can also be used for room temperature measurements.

5.1.2. Diamond-anvil cell alignment.

After the diamonds are placed on their base plates, they must be aligned in order to provide high pressure without cracking. The first condition for alignment is parallelism, in which the culet surfaces are parallel to each other. This is accomplished by adjusting screws for the hemispherical base plate. During these fine adjustments, interference fringes are observed in the microscope. The goal is to make the fringes as broad as possible, in which case the culet surfaces are almost parallel to each other. After this task was completed, translational alignment is performed. Again, looking into the microscope allows one to monitor the two culet surfaces. After the diamonds are aligned, the Allen screws are tightened slightly to make the fringes completely disappear. This procedure ensures nearly perfect parallelism of the culet planes. Three reference points are marked on the piston and their heights are measured with an indicator, to an accuracy of 2 μm. The relative heights of these points must be maintained throughout the experiment.

5.1.3. Diamond-anvil cell loading.

We used a circular piston-cylinder type DAC, similar to the cell described in Ref. 81, with type I diamonds with culet diameters of 700 μm. A stainless steel gasket of 250 μm thickness was pre-indented to 100 μm. A hole of 340 μm in diameter was drilled in the center of the indentation, using a carbide drill. A sample was placed in the hole and the whole cell was assembled and immersed in liquid nitrogen. Compressed helium gas was bubbled into the liquid nitrogen to suppress boiling. Liquid nitrogen seeped into the hole in the gasket. Then the Allen screws were tightened to apply force to the diamonds and pressure to the nitrogen and the sample. The cell was then taken out of the liquid nitrogen and warmed up to room temperature. The condition of the sample was checked with the microscope. The relative height of three reference points, mentioned in the previous section, was measured and adjustments are made, if necessary, to maintain alignment. Subsequent pressure adjustments were made by either loosening or tightening one or more of the Allen screws.

5.1.4. Low-temperature measurements.

After the loading was completed, the cell was mounted onto the sample holder and put into a Janis continuous-flow liquid-helium cryostat with wedged zinc selenide windows. The temperature was maintained at approximately 8 K. The pressure was determined by measuring the vibrational frequency of CO_2 in the nitrogen matrix. Its

pressure dependence was determined in Ref. 82. Thus it serves as good *in situ* pressure calibration in the range from 0 to 7 GPa.

5.1.5. Fluorescence measurement system.

As was mentioned before, one of the most common methods to determine the pressure in a DAC is to measure the shift of the ruby fluorescence lines. Our fluorescence measurement system consists of a monochromator, a charge-coupled device (CCD) array detector, a controller, and a computer. Green laser light (532 nm) from a laser pointer is the excitation source for the ruby fluorescence. The detection system uses a liquid nitrogen (LN) cooled CCD detector and Acton SpectraPro 300i monochromator/spectrograph. It has three gratings, which cover a broad range of the spectrum from visible to near-infrared. In order to suppress the signal from the laser light, a red filter is placed in front of the spectrograph slit. The controller is programmed by the computer and determines the setup for spectra acquisition. The detector must be cooled to LN temperature. In order to maintain the appropriate temperature, a 1.7 liter Dewar is mounted on the back side of the CCD matrix. When filled with liquid nitrogen, the Dewar maintains the necessary temperature for approximately 30 hours. The commercially available software WinSpec32 is installed onto the computer and is used to save and analyze all the data obtained.

5.2. Fourier transform infrared spectroscopy (FT-IR).

5.2.1. Basic theory of FT-IR.

Fourier-transform infrared spectroscopy (FT-IR) is an important technique used in biology, chemistry, and physics. The discussion in this section follows the review given by Griffiths[83]. The basis for FT-IR spectroscopy is the Michelson interferometer (Fig. 15). A broadband beam of radiation from the source impinges on the beam splitter, where it is partially reflected to the fixed mirror and partially transmitted to the movable mirror. The two beams are reflected back to the source and onto the detector. When the two mirrors are at the same distance from the beam splitter, the path difference between the two beams is zero and they interfere constructively.

When one of the mirrors is moved, a path difference δ is introduced, and there is a nonzero phase shift between the two beams. The intensity of the beam at the detector is given by the following expression:

$$I(\delta) = 0.5I(\lambda)\left[1 + \cos\left(2\pi \delta/\lambda\right)\right] = 0.5I(k)\left[1 + \cos(2\pi k\delta)\right] \quad , \quad (96)$$

where λ is the wavelength and k is the wave number, $k = \frac{1}{\lambda}$. The cosinusoidal part of Eq. (96) is the *interferogram*, and will be of interest in this discussion. The spectrometer obtains the value $I(\delta)$. The real intensity as a function of wave number, I(k), is obtained via *Fourier transformation* of $I(\delta)$. This transformation is given by:

$$I(k) = \int_{-\infty}^{+\infty} I(\delta)\cos(2\pi k\delta)\cdot d\delta \quad . \quad (97)$$

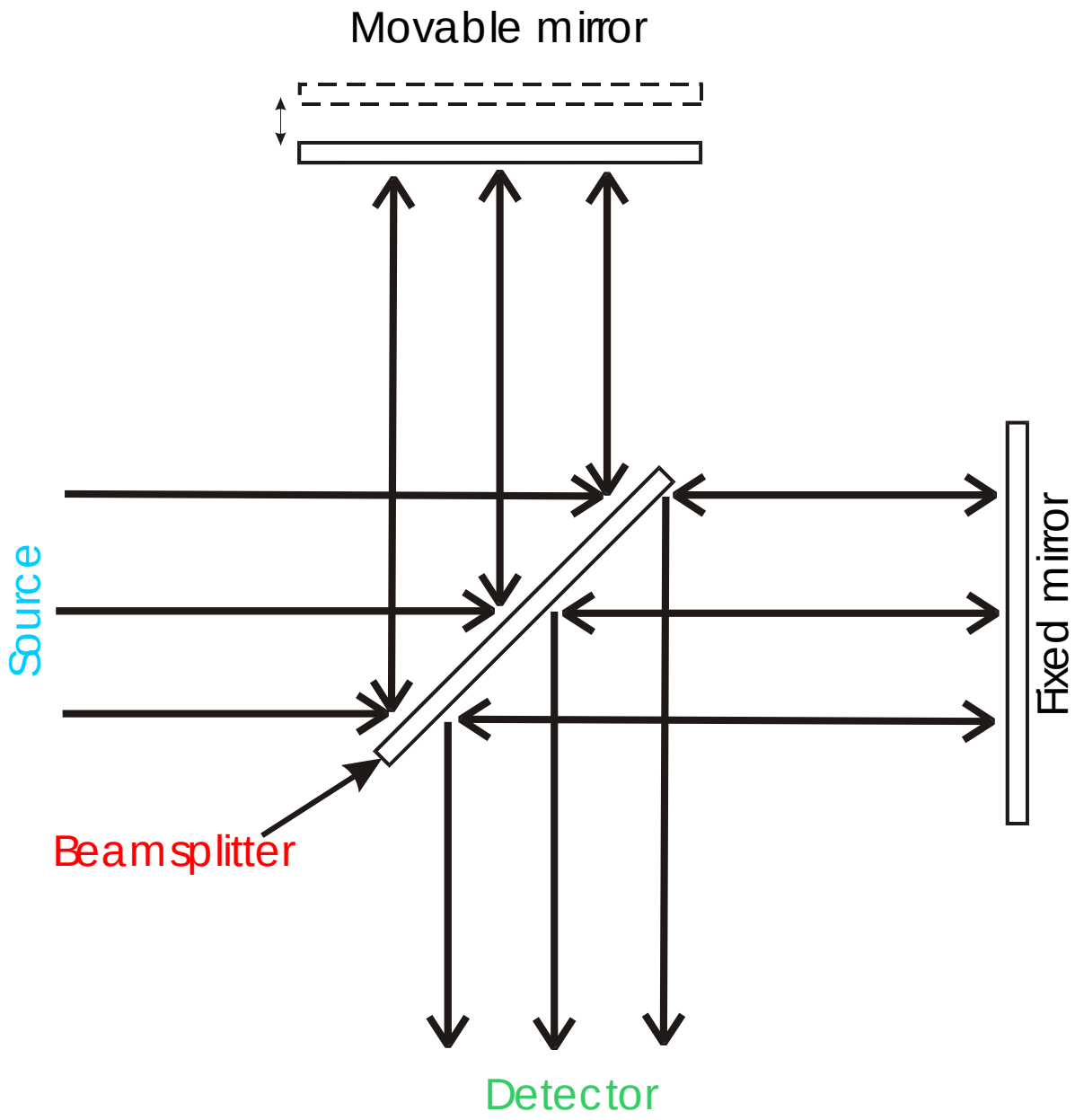

Figure 15. Michelson interferometer.

For real systems, we must introduce two corrections. The first takes into account the efficiency of beamsplitter, amplification characteristics, and detector response. Experimentally, we obtain *not* the true I(k), but some other function B(k), due to these factors. The second correction accounts for the fact that the path length difference is limited by a maximum value Δ. Thus the spectrum obtained will be given by:

$$G(k) = \int_{-\infty}^{+\infty} I(\delta) D(\delta) \cos(2\pi k \delta) \cdot d\delta \quad , \tag{98}$$

where $D(\delta)$ is the truncation function, which is zero for all $|\delta| > \Delta$. The shape of this function can be quite arbitrary, the simplest being the boxcar function, which is equal to one for all $|\delta| < \Delta$.

The function G(k) can be viewed as the convolution of the true spectrum, B(k), and the Fourier-transform of the truncation function, $D(\delta)$:

$$G(k) = \int_{-\infty}^{+\infty} B(k') f(k - k') \cdot dk' \quad , \tag{99}$$

where f(k) is given by:

$$f(k) = \int_{-\Delta}^{\Delta} D(\delta) \cos(2\pi k \delta) \cdot d\delta \quad . \tag{100}$$

The function f(k) is called the *instrument line shape* (ILS). For the boxcar truncation function and monochromatic spectral line of wavenumber k_1, we obtain for G(k):

$$G(k) = 2\Delta \cdot B(k_1) \cdot \frac{\sin[2\pi(k_1 - k)\Delta]}{2\pi(k_1 - k)\Delta} \quad . \tag{101}$$

It turns out that the spectral resolution can be affected by the choice of the function $D(\delta)$. There are many types of truncation functions, and for some of them the

side oscillations in the interferogram are suppressed. This suppression is called *apodization* and the appropriate $D(\delta)$ is called the *apodization function*. A more detailed discussion of this problem can be found elsewhere[84].

Other factors affecting the performance of Fourier transform spectrometers are the beam divergence, mirror misalignment, and poor mirror drive. The first factor sets the limit for the achievable resolution, Δk, to be

$$\Delta k = k_{max}\alpha^2 \quad , \tag{102}$$

where α is the divergence angle and k_{max} is the maximum wave number in the spectrum. A detailed derivation of Eq. (102) can be found in Ref. 83.

For an ideal spectrometer, the ratio of the intensity at zero path difference to the intensity at large path difference is two. Therefore, the parameter R,

$$R = \frac{I(0) - I(\infty)}{I(\infty)} \tag{103}$$

is equal to 1. For a real spectrometer, the value of R gives a measure of how well the interferometer is aligned.

A poor mirror drive can lead to a loss in resolution. If the mirror is tilted by an angle β, then the difference in retardation, $\Delta\delta$, is:

$$\Delta\delta = 2D\tan\beta \approx 2D\beta \tag{104}$$

for small β, where D is the beam diameter. A loss in resolution occurs when $\Delta\delta > 0.1\lambda$. Then the tilt angle must satisfy the following inequality:

$$\beta \le \frac{1}{20Dk_{max}} \quad . \tag{105}$$

For D=5 cm and k_{max}=5000 cm^{-1} the angle β must be less than 2 μrad. The critical angle may be increased by aperturing the beam, but only at the cost of a decrease in beam intensity.

To obtain a spectrum, an inverse Fourier transform must be performed [Eq.(97)]. Cooley and Tukey[85] developed a fast Fourier transform (FFT) algorithm, which uses a low number of operations. Another important issue is the phase correction, due to optical, electronic, and sampling effects. There are several methods to address the problem of phase correction, most famous of them being described by Mertz[86] and Forman[87].

5.2.2. Beer's Law.

While traveling through an absorbing medium, a beam of radiation decreases in intensity. The change in intensity is proportional to intensity itself:

$$\frac{dI}{dx} = -n\sigma I \quad , \tag{106}$$

where σ is the absorption cross section and n is the concentration of absorbing particles. Assuming that the concentration is uniform in space, we obtain Beer's law:

$$I = I_0 e^{-n\sigma d} \quad , \tag{107}$$

where d is the thickness of the sample. The beam intensity exponentially decreases with the thickness of the medium through which the beam travels.

Beer's law is valid for dilute solutions. Deviations may arise due to a non-uniform distribution of absorbing centers, stray light coming into the system, or nonlinear effects at high intensities. In general, the absorption cross section is frequency dependent. For example, a system absorbs light at the vibrational frequencies of the molecules

composing it. This absorption is seen in the spectrum as "dips" in the intensity measured by the detector.

5.2.3. Beamsplitters for FT-IR spectrometers.

One of the most important parts of the FT-IR spectrometer is the beamsplitter. Suppose that a beamsplitter has a reflectance R and a transmittance T. Neglecting any absorption of radiation in the beamsplitter, we can write:

$$R + T = 1 \qquad (108)$$

It can be shown that if the incident intensity is I, then the intensity of light going towards the detector is given by $(2RT)I$. Given Eq. (108), the value of 2RT reaches maximum at R=T=0.5, at which point it 2RT=0.5. This explains the appearance of the coefficient 0.5 in Eq. (96), where we implicitly assumed an ideal beamsplitter. To account for an imperfect beamsplitter, Eq. (96) can be rewritten as:

$$I(\delta) = 0.5\eta(k)I(k)[1 + \cos(2\pi k\delta)] \quad , \qquad (109)$$

where $\eta(k) = 4RT$. The function $\eta(k)$ is known as the *relative beamsplitter efficiency* and should be as close to unity as possible over the widest possible spectral range. Some materials that are used as beamsplitters include polyethylene terephthalate (Mylar), germanium, CsI, CsBr, and KBr. The two most commonly used materials are Mylar and KBr. The choice of beamsplitter is dictated by the spectral range of interest. Mylar is used in the far-infrared region, whereas in the mid-infrared region it is necessary to use KBr.

5.2.4. Infrared detectors.

Infrared detectors are usually divided into two major classes: thermal detectors and quantum detectors. Thermal detectors sense the change in the temperature of the absorbing material. Such a change can result in electromotive force (thermocouple), change in resistance (bolometer, thermistor), movement of a membrane caused by thermal expansion of a gas (pneumatic detector), which, in turn, causes the change in illumination of auxiliary cell (Golay detector). Thermal detectors are usually slow. The most sensitive are Golay detectors and pyroelectric bolometers. Thermal detectors are usually used in the far-infrared spectral region.

Quantum detectors use the property that photons can excite electrons in solids from the valence band into the conduction band. Some of these detectors use impurity atoms, which absorb photons with energies lower than the band gap. Examples include PbS, mercury cadmium telluride (MCT), germanium doped with copper, gallium or antimony, and InSb. Quantum detectors are much faster than thermal detectors. However, these detectors have a sharp cutoff at low wavenumbers, and their response is influenced by thermal noise. This leads to the requirement that these detectors need to be cooled. Some detectors, like MCT, operate at liquid nitrogen temperature (77 K). Others, like doped germanium, require liquid helium temperatures (4.2-12 K). Quantum detectors are used in the mid- to near-infrared spectral range.

5.3. Advantages of FT-IR spectrometers.

Besides the FT-IR spectrometers there are also various grating IR spectrometers. Their relative performance is very important to know when choosing among them for the particular experiment. There exist theoretical criteria to judge the relative efficiency of two spectrometers, which will be discussed below. Also practical results have been obtained and will be described as well.

5.3.1. Jacquinot's advantage.

An important parameter which characterizes the efficiency of a spectrometer is the throughput. The throughput is defined as the product of the beam area and its solid angle at any focus. For the Fourier spectrometer, the throughput is given by:

$$\Theta_F = 2\pi \frac{\Delta k}{k_{max}} A_F \quad , \qquad (110)$$

where A_F is the area of the mirrors that are illuminated. For the grating spectrometer the throughput is:

$$\Theta_G = \frac{h A_G \Delta k}{f a k^2} \quad , \qquad (111)$$

where h is the height of the slit, f is the focal length of the collimating mirror, a is the grating constant. The ratio of two throughputs, J, known as Jacquinot's advantage, is given by:

$$J = \frac{2\pi A_F f a k^2}{A_G h k_{max}} \quad . \qquad (112)$$

A calculation of J for several spectrometers showed that for all but very low wavenumbers, the FT-IR spectrometer is significantly better than a grating spectrometer (see, for example, Ref. [88]).

5.3.2. Fellgett's advantage.

The signal-to-noise ratio (SNR) for a Fourier spectrometer will be greater than the SNR for a grating spectrometer by a factor of $\sqrt{M}$, where M is the number of resolution elements, provided that all other parameters are the same. For example, for the mid-infrared spectrum taken in the range from 400 to 4000 cm^{-1} with a resolution of 1 cm^{-1}, Fellgett's advantage will be $\sqrt{3600} = 60$. In addition, the time advantage for an FTIR spectrometer is directly proportional to M.

Combining Jacquinot's and Fellgett's advantages, it can be shown that a Fourier spectrometer will be 2000-3000 times more sensitive than a grating spectrometer. In practice, however, a smaller advantage is observed. This is due to noise arising from other parts of the FTIR spectrometer, mainly the detector.

5.3.3. Fourier-transform infrared (FT-IR) spectrometry.

The DA8 Bomem FT-IR spectrometer was used in obtaining the data for this work. A Globar, which is a heated ceramic, was used as a broadband light source (200 to

10000 cm^{-1}). The beamsplitters used were KBr for the mid-infrared region (450 to 5000 cm^{-1}) and Mylar for far-infrared region (125 to 850 cm^{-1}). The pressure inside the FT-IR compartment is maintained at a level of ≤ 0.2 Torr and the Globar is cooled by the flow of chilled water. The moving mirror velocity can vary from 0.01 to 4 cm/s and the aperture ranges from 0.5 to 10 mm. Mirrors alignment is maintained with the help of a He-Ne laser. Monochromatic laser light creates an interferogram and several detectors sense it. If the mirrors are out of alignment, the interferograms for different detectors exhibit relative phase shift, which can be measured. This shift gives the signal for alignment transducers to correct the misalignment.

For room-temperature measurements, we used an MCT detector for mid-infrared spectra and a DTGS detector for the far-infrared. For low-temperature measurements, a Ge:Cu photoconductive detector was used. Its operation is limited to liquid helium temperatures. The spectrometer is connected via Ethernet cable to the computer with PCDA software for the data acquisition and the GRAMS software package to process and analyze the spectra.

6. Present work.

6.1. Organic conjugated molecules under pressure.

Although the investigation of polyphenyls has been quite extensive, there are relatively few reports on high-pressure research on these molecular solids. The conformation of p-terphenyl in its twisted conformation is still under question. In the following sections, the results of FTIR spectroscopy on biphenyl, p-terphenyl, and p-quaterphenyl under hydrostatic pressure are presented.

6.1.1. Biphenyl.

6.1.1.1. Experimental results.

In this section, high-pressure IR spectroscopy experiments on biphenyl are discussed. Some of these results have been published in Ref. 89.

Two samples were investigated. First, protreated biphenyl ($C_{12}H_{10}$), hereafter referred to simply as biphenyl, was measured. Second, deuterated biphenyl ($C_{12}D_{10}$), or biphenyl-d_{10}, was measured. In the latter sample, every hydrogen was replaced by a deuterium, with an isotopic purity of 98%[90]. The IR spectra for biphenyl are shown in Fig. 16 and spectra for deuterated biphenyl are shown in Fig. 17. Resolution was 2 cm^{-1}.

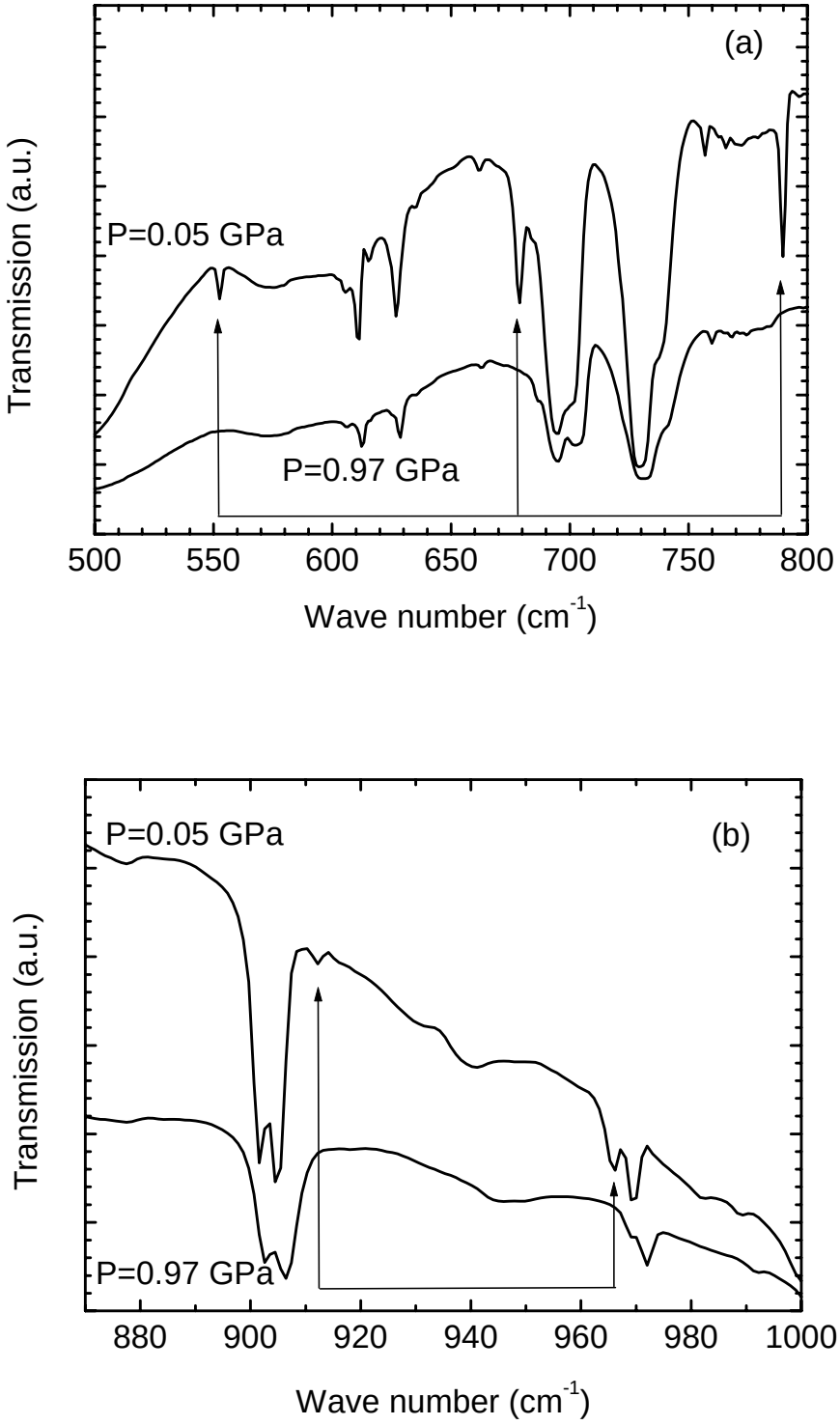

Figure 16. Biphenyl spectra at pressures below and above phase transition.

IR-modes, that disappear upon transition, are indicated by arrows.

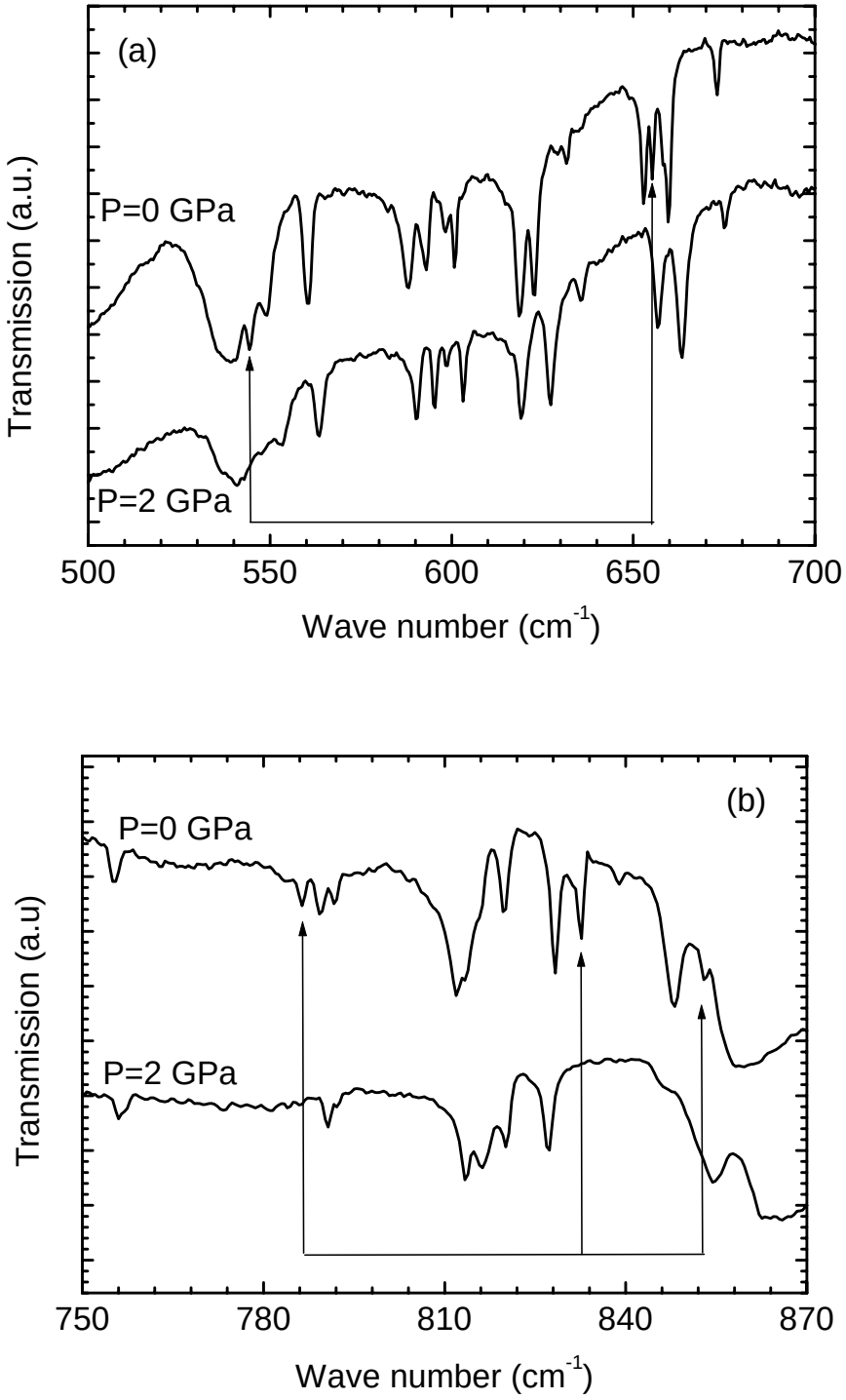

Figure 17. Deuterated biphenyl spectra at pressures below and above phase transition.

IR-modes, that disappear upon transition, are indicated by arrows.

By progressively increasing the pressure we found that certain peaks disappear when the pressure rises above certain value. Those peaks that disappear are indicated by arrows. The spectral range from 500 to 1100 cm^{-1} corresponds to out-of-plane motion of hydrogen atoms in which the atomic displacement is perpendicular to the plane of the appropriate ring. There are three peaks in the biphenyl spectrum in the range 500-800 cm^{-1} that disappear upon the phase transition [Fig. 16(a)]. The spectral range from 1100 to 1800 cm^{-1} includes in-plane hydrogen bending modes. Upon substitution with deuterium, hydrogen-related frequencies should decrease by some factor, which in an "ideal" case is $\sqrt{2}$. From Fig. 17(a) it is seen that there are two peaks, at 545 and 655 cm^{-1}, that disappear in deuterated biphenyl. Relative to the hydrogen peaks at 679 and 790 cm^{-1} [Fig. 16(a)], the deuterium peaks are shifted downward by a factor less than $\sqrt{2}$. The deviation from the ideal case is due to anharmonic effects as well as significant motion of the carbon atoms (see Appendix B). In the observed spectra the strongest peaks were found to be due to out-of-plane hydrogen motion.

The pressure-dependent shifts of several out-of-plane hydrogen bending modes are plotted for biphenyl in Fig. 18. In Fig. 19 we plotted the normalized intensities for two peaks that disappear after the phase transition, as a function of pressure. Uncertainties in data are smaller than the size of points in Fig. 18, 19. The intensity of the peak at approximately 836 cm^{-1} was chosen as a reference for the normalization. At a pressure between 0.07 and 0.4 GPa, the integrated absorbance of the peaks at 790 and 841 cm^{-1} drops to zero, to within experimental uncertainty. Our results are in agreement with those of Ref. 36, which reported a phase transition at 0.18 GPa.

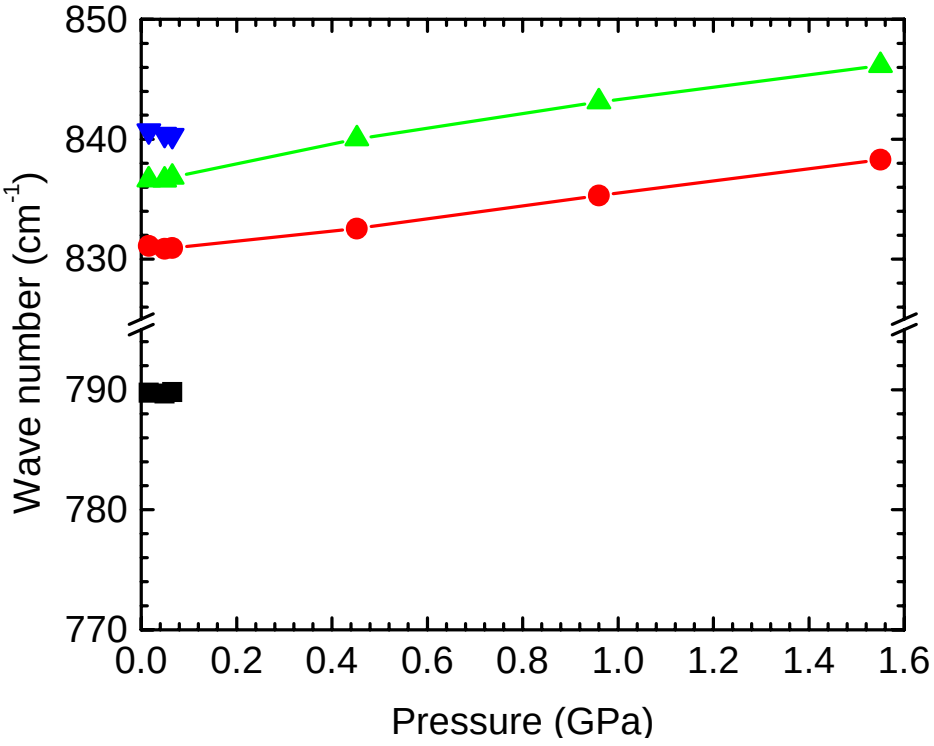

Figure 18. Frequency dependence of several IR-modes on the pressure for biphenyl.

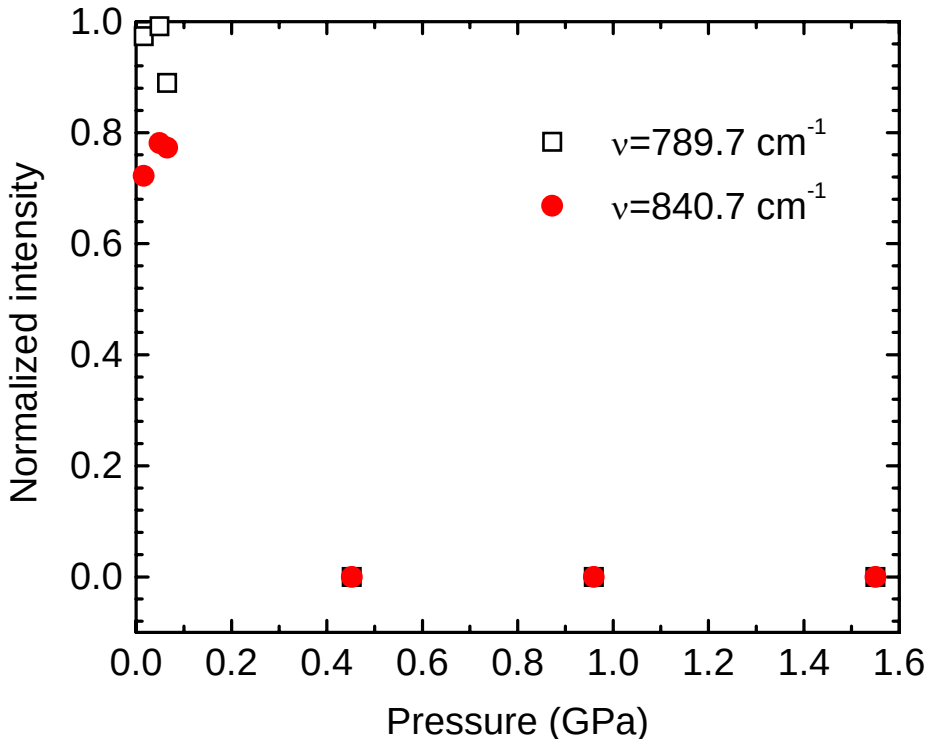

Figure 19. Normalized intensity dependence on the pressure for two IR-modes that become IR-inactive upon phase transition for the biphenyl molecule.

6.1.1.2. Group theory.

To explain the disappearance of IR activity for certain vibrational modes, we applied group theory to analyze the normal vibrational modes of the molecules. The z-axis in our analysis is directed along the main axis of the molecule, the x-axis is in the molecular plane for the planar conformation, and the y-axis is perpendicular to the plane. A schematic diagram of biphenyl in its twisted conformation is shown in Fig. 20.

The twisted conformation of biphenyl belongs to the D_2 point group. The vibrational modes can be classified as follows:

$$\Gamma = 15A \oplus 13B_1 \oplus 16B_2 \oplus 16B_3$$

Modes belonging to the B_1, B_2, or B_3 irreducible representations are IR-active, for a total of 45 IR-active modes. For the planar configuration, biphenyl belongs to the D_{2h} point group. The vibrational modes are given by:

$$\Gamma = 11A_g \oplus 4A_u \oplus 3B_{1g} \oplus 10B_{2g} \oplus 6B_{3g} \oplus 10B_{1u} \oplus 6B_{2u} \oplus 10B_{3u}$$

Modes belonging to the B_{1u}, B_{2u}, or B_{3u} irreducible representations are IR-active, for a total of 26 IR-active modes. Upon planarization, some of the B_1, B_2, and B_3 modes transform into B_{1g}, B_{2g}, and B_{3g} modes, which are IR-inactive. This disappearance of certain IR absorption peaks is in qualitative agreement with our experimental observations.

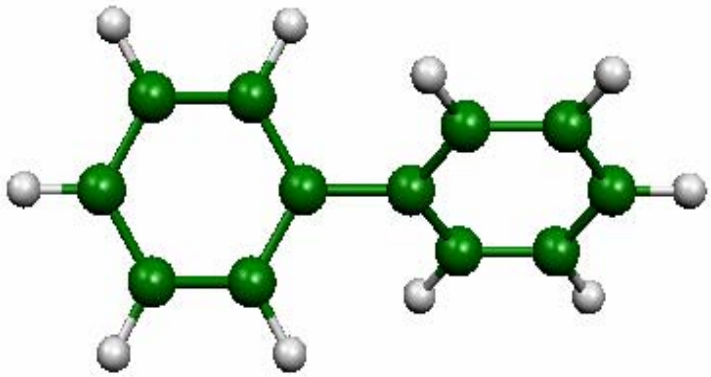

Figure 20. Biphenyl molecule structure in the twisted conformation.

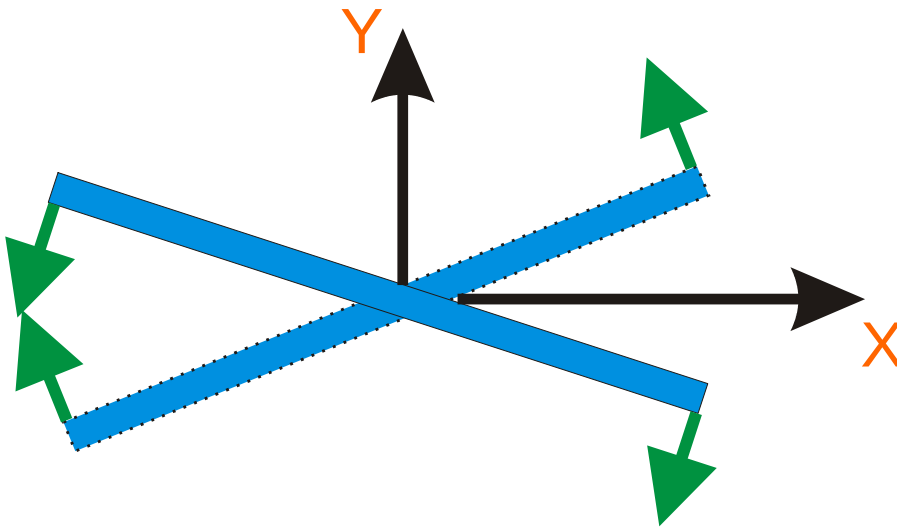

Figure 21. Schematic representation of the mechanism of IR-activity loss for one of the hydrogen out-of-plane modes for the biphenyl molecule.

In Fig. 21, one of the B_3 modes is shown schematically. The cross sections of the phenyl rings are represented as rectangles and the dipole moments, induced by the motion of hydrogen atoms, are shown by the arrows. In the twisted conformation, the mode has a net induced dipole moment in the x-direction. In the planar conformation, the dipoles exactly cancel, so that the mode is IR-inactive.

6.1.1.3. Numerical calculations.

Ab initio and DFT calculations are used extensively to model molecular and atomic systems. The biphenyl structure has been numerically calculated by previous researches[91,92]. In this work, calculations have been performed in order to simulate the IR spectra of biphenyl and deuterated biphenyl, using *Gaussian 98W* (Ref. 9). We used the density functional theory (DFT) Becke 3-parameter method[93] with the Lee-Yang-Parr correlation functional and the basis set 6-31G(d). The details about calculations and basis sets have been described previously.

For the twisted structure, the calculated dihedral angle between two phenyl rings is 38º for biphenyl and 35º for deuterated biphenyl. Electron diffraction experiments on biphenyl in the gas phase yielded a dihedral angle of 40º (Ref. 27), in good agreement with our calculations. Numerical optimization of the geometric structure of the molecules yields a configuration that belongs to the C_2 point group. This low symmetry is due to a distortion of the phenyl rings. However, the deviation from planarity in each phenyl ring is very small. To a good approximation, we can consider this molecule as belonging to the D_2 point group, and our previous group-theory analysis remains valid.

Table III. Vibrational modes in biphenyl ($C_{12}H_{10}$) that are IR active in the twisted conformation but IR inactive in the planar conformation.

Calculated				Experimental	
Frequency (cm^{-1})	Normalized intensity	Symmetry	Mode character	Frequency (cm^{-1})	Normalized intensity
559.9	0.2622	B_3	H out-of-plane	552.9	0.272
628.6	0.0006	B_2	C-H in-plane	ND[a]	ND[a]
714.7	1	B_3	H out-of-plane	679.3	0.745
796.9	0.88	B_3	"	789.7	1
860.9	0.086	B_1	"	840.7	0.720
938.5	0.15	B_3	"	912.1	0.041
968.7	0.1248	B_2	"	965.8	0.377
995.6	0.0096	B_2	"	ND[a]	ND[a]
1116.1	0.061	B_1	H in-plane	ND[a,b]	ND[a,b]
1192.9	0.0002	B_3	"	ND[a,b]	ND[a,b]

[a]ND = not discovered.

[b]Calculated frequency lies within diamond absorption band.

Table IV. Vibrational modes in deuterated biphenyl ($C_{12}D_{10}$) that are IR active in the twisted conformation but IR inactive in the planar conformation.

Calculated				Experimental	
Frequency (cm^{-1})	Normalized intensity	Symmetry	Mode character	Frequency (cm^{-1})	Normalized intensity
567.07	1	B_3	D out-of-plane	544.5	0.340
602.82	0.0018	B_2	D in-plane+ring distortion	ND[a]	ND[a]
668.63	0.14	B_3	D out-of-plane	655.3	0.752
670.04	0.1456	B_1	"	ND[a]	ND[a]
784.29	0.264	B_1	D out-of-plane+ring distortion	786.3	0.337
789.11	0.161	B_3	"	789.5	0.444
838.72	0.4535	B_3	D in-plane+ring distortion	832.5	1
844.02	0.0789	B_2	D in-plane	838.8	0.187
862.8	0.0301	B_2	"	853.0	0.188
1071.88	0.0005	B_2	"	ND[a]	ND[a]

[a]ND=not discovered

The vibrational spectra calculations were made with the symmetry restricted to the D_2 point group. The planar conformation of the molecule, belonging to the D_{2h} point group, turns out to be stable during the calculations. One of the calculated frequencies is imaginary, however, indicating that the planar configuration is not a minimum on the potential energy surface.

A correspondence was made between vibrational modes in the planar and twisted conformations by examining similarities in the character of motion, reduced mass, frequency, and IR intensity for any given pair of modes. Frequencies that are IR-active in the twisted conformation but IR-inactive in the planar conformation, as predicted by this computation for the twisted conformation of biphenyl, are listed in Table II together with the experimental results. The frequencies for vibrational modes in deuterated biphenyl are given in Table III. In biphenyl, we did not observe hydrogen in-plane modes because the frequencies of those modes lie within the diamond absorption band. In deuterated biphenyl, however, these modes are shifted downward in frequency and therefore become observable. In both tables the intensity normalization was carried out with respect to the highest-intensity peak. In order to illustrate the disappearance of IR-active peaks, the calculated intensity of two peaks at 715 and 797 cm^{-1} is plotted as a function of dihedral angle between the phenyl rings (Fig. 22). The outlying data point at 38º is probably due to the fact that all other angles correspond to non-optimal structures. The experimental intensities and frequencies approximately match the theoretical ones, with the exception of the experimental peak at 840.7 cm^{-1} for biphenyl. According to Fig. 17, there is a possibility that this peak simply merges with the peak at 836 cm^{-1}, and is not in fact a "disappearing peak."

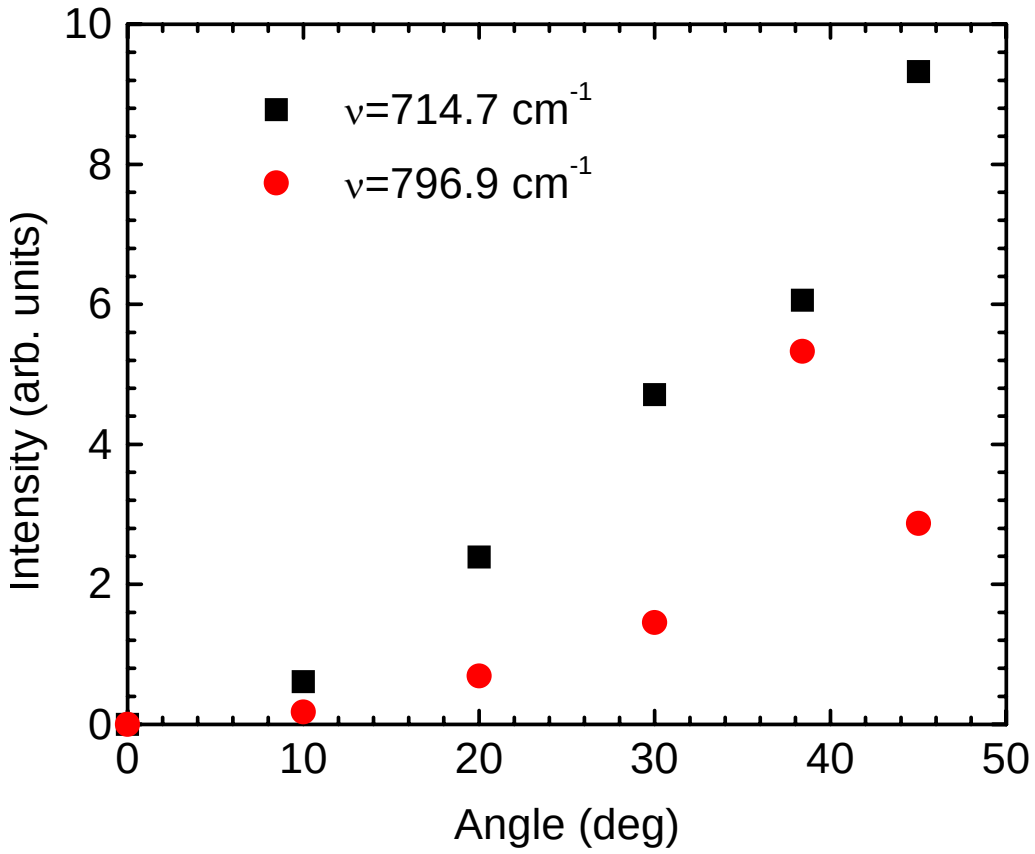

Figure 22. Calculated intensity dependence of two IR-modes on the twist angle between two phenyl rings in the biphenyl molecule.

In Tables III and IV the characters of the vibrational modes are described briefly. “H out-of-plane” corresponds to the hydrogen atoms moving perpendicular to the plane of a phenyl ring. “H in-plane” corresponds to the hydrogen atoms moving in the plane of a phenyl ring. “C-H in-plane” means that carbon atoms are moving significantly as well. The same descriptions apply for the deuterium atoms. “Ring distortion” indicates that carbon atoms are moving in or out of the phenyl-ring plane together, but asynchronously with the deuterium atoms. Calculations of the normal modes indicate the induced dipole moments are directed predominantly perpendicular to the z-axis. Exceptions to this rule include the calculated B_1 modes for biphenyl and deuterated biphenyl, at 1116.1 cm^{-1} (Table III) and 784.3 cm^{-1} (Table IV), respectively. In Fig. 23 we compare the experimental and theoretical frequencies for the IR-modes that become IR-inactive upon planarization of the molecule for both hydrogenated and deuterated biphenyl. The experimental and calculated frequencies match very well, as seen from Fig. 23. The uncertainty in our calculations is estimated to be within 5% error.

6.1.1.4. Conclusions.

In conclusion, it was found that biphenyl undergoes a phase transition, in which the molecules flatten under high pressure. This flattening results in the disappearance of certain IR peaks. The numerical and group-theory analysis matches the experimental data very well. The majority of vibrational modes that become IR-inactive upon planarization of the molecule, have their dipole moments induced in the direction perpendicular to the main axis of the twisted molecule.

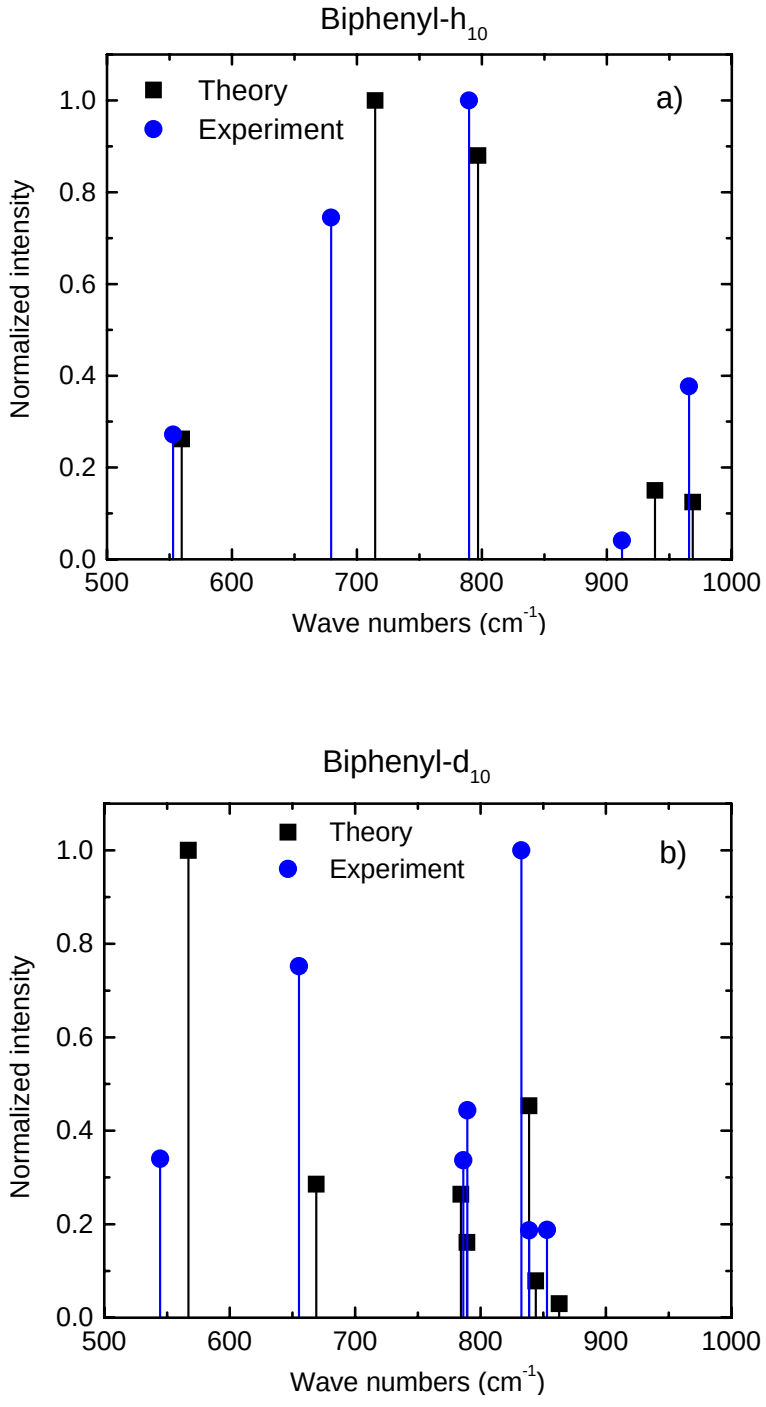

Figure 23. Comparison between experimental and calculated frequencies for biphenyl and deuterated biphenyl modes that become IR-inactive upon phase transition.

6.1.2. P-terphenyl.

6.1.2.1. Experimental results.

In this section, high-pressure IR spectroscopy experiments on p-terphenyl are discussed. Some of these results are also presented in Ref. 94.

In contrast to biphenyl, the conformation of p-terphenyl is not known with any degree of certainty. In its twisted conformation, the p-terphenyl molecule can be characterized by two angles of twist, associated with the two outer phenyl rings. If both angles are of the same sign and have the same value, then the molecule has C_{2h} symmetry. If the twist angles have different signs, then the symmetry group is D_2. If the twist angles have slightly different values, then the symmetry group is C_2. We will denote such low-symmetry configurations C_2' and C_2'', if molecule resembles that of C_{2h} or D_2 symmetry, respectively.

There is also a possibility of having one outer ring twisted whereas other rings remain in the same plane. In this case, the molecule also belongs to the C_2 group. These configurations are illustrated in Fig. 24.

As in the case of biphenyl, both hydrogenated p-terphenyl ($C_{18}H_{14}$), later referred to simply as p-terphenyl, and deuterated p-terphenyl ($C_{18}D_{14}$) were investigated. The IR spectra for p-terphenyl are shown in Fig. 25 and spectra for deuterated p-terphenyl are shown in Fig. 26. Spectra were taken with resolution 2 cm^{-1}. The displayed frequency range corresponds to hydrogen bending modes. These bending modes are in- and out-of-plane modes, as observed in biphenyl. When pressure is raised above a critical value, se-

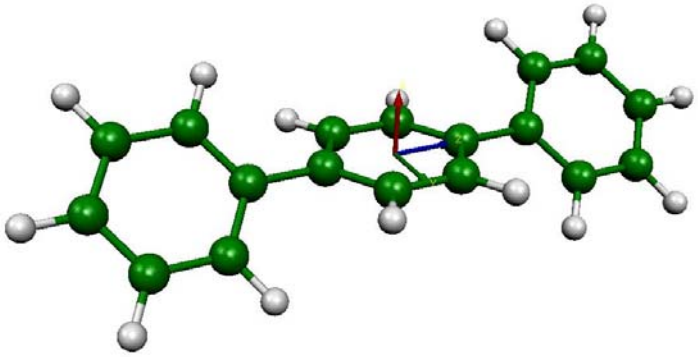

C_{2h}

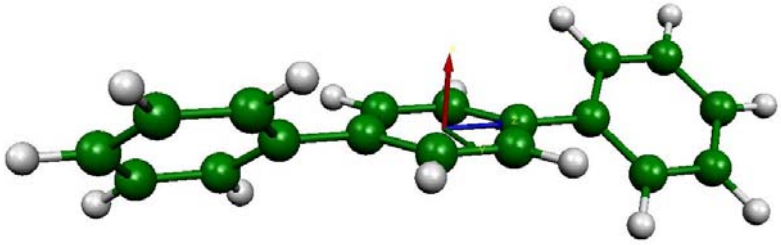

D_2

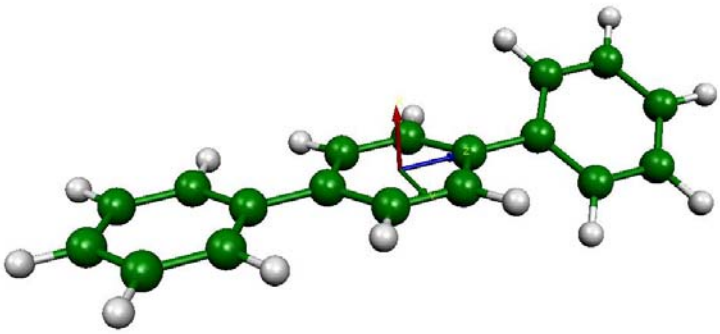

C_2

Figure 24. Three possible isomers of p-terphenyl molecule in the twisted conformation.

veral IR absorption peaks abruptly disappear from the spectrum. No hysteresis was observed in our experiments.

The pressure-dependent shifts of several out-of-plane hydrogen bending modes in p-terphenyl are plotted in Fig. 27. Again, uncertainties in data are within points' size. The frequencies shift discontinuously for certain peaks; namely, the peaks at 567, 573, and 912 cm^{-1}. This observation, together with the disappearance of other peaks, indicates the existence of a phase transition. The transition pressure lies between 0.2 and 0.6 GPa, consistent with previous studies (Ref. 65), which determined a phase transition at approximately 0.5 GPa.

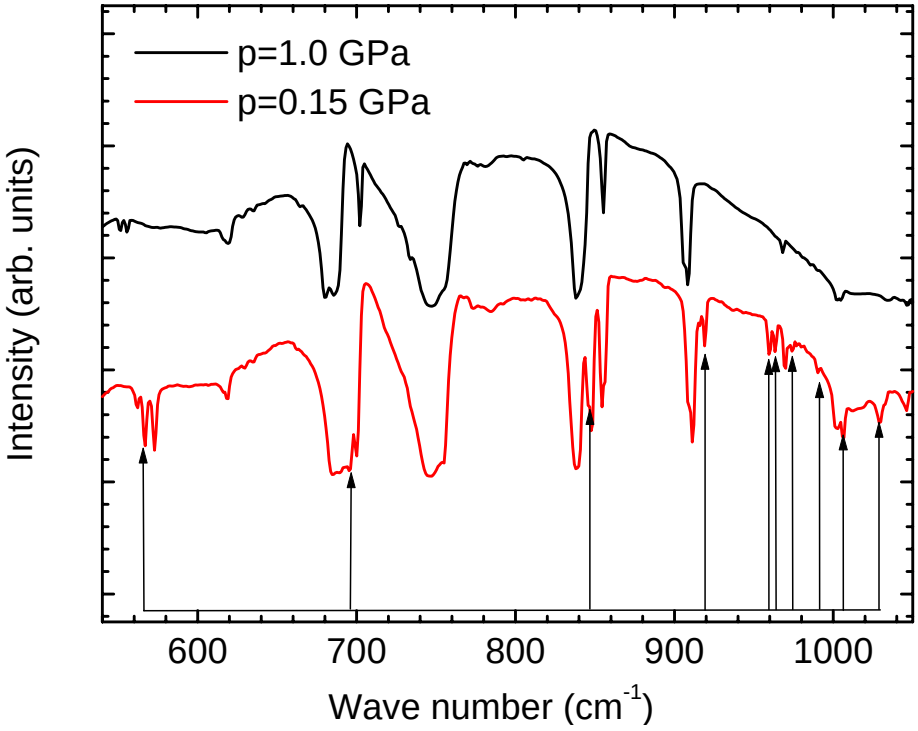

Figure 25. P-terphenyl spectra at pressures below and above phase transition.

IR-modes, that disappear upon transition, are indicated by arrows.

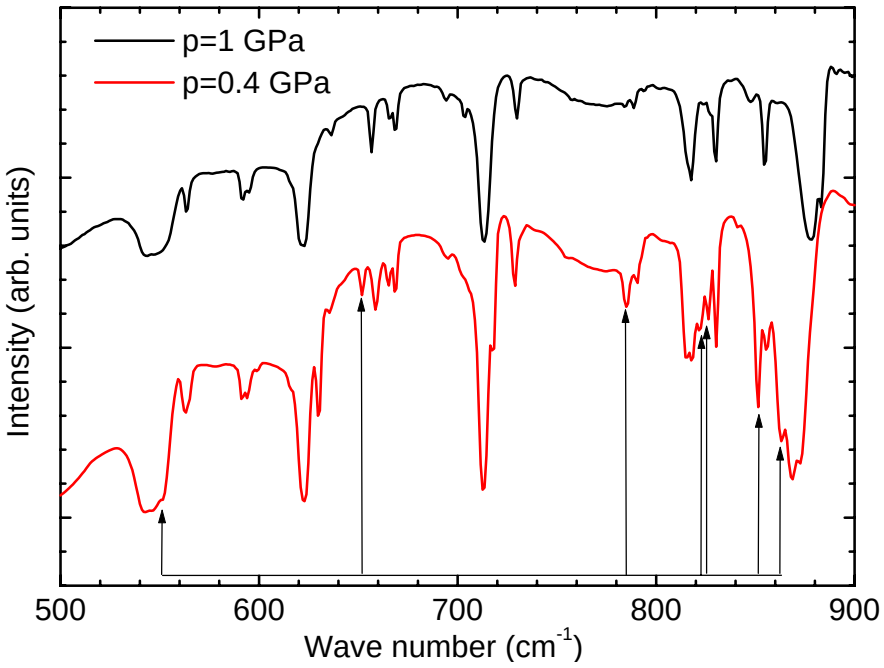

Figure 26. Deuterated p-terphenyl spectra at pressures below and above phase transition.

IR-modes, that disappear upon transition, are indicated by arrows.

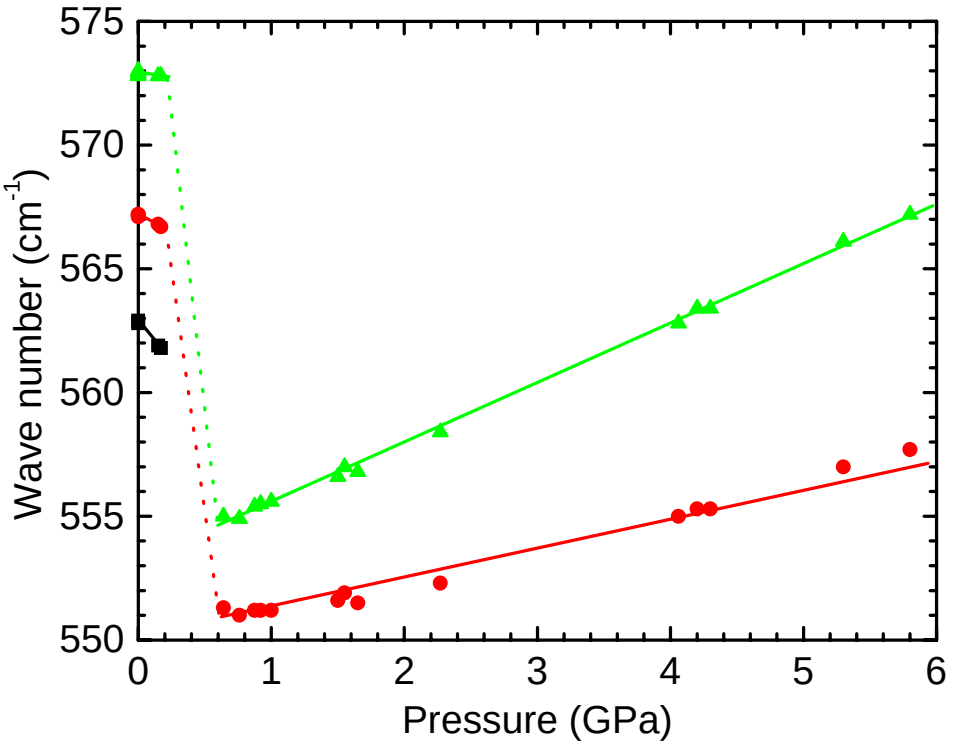

Figure 27. Frequency dependence of several IR-modes on the pressure for p-terphenyl.

Table V. Ground-state energies of p-terphenyl molecules in different conformations relative to the planar conformation.

Symmetry group	Energy, meV			
	Basis set			
	6-31+G(d)	6-311+G(d)	6-311++G(2d,p)	6-311++G(2df,2dp)
Planar, D_{2h}	0	0	0	0
Twisted, C_{2h}	-163.4	-175.6	-178.7	-146.6
Twisted, D_2	-162.4	-174.2	-176.2	-145.4

6.1.2.2. Numerical calculations.

Previous theoretical studies have investigated the conformation of the p-terphenyl molecule (Ref. 58, 91). We performed *ab initio* calculations of p-terphenyl using the Gaussian98 software package (Ref. 9). All calculations were done using the same method as in the case of biphenyl. We used two basis sets, 6-31+G(d) and 6-311+G(d), to obtain vibrational frequencies for the p-terphenyl molecule in different configurations. In addition, two higher basis sets, 6-311++G(2d,p) and 6-311++G(2df,2dp) were used to check the consistency of the ground-state energy calculations. A summary of the energy calculations is given in Table V. It is clear that the C_{2h} isomer is consistently more energetically favorable than the D_2 isomer. This result is consistent with previous x-ray diffraction experiments, which indicated that the molecules in a p-terphenyl crystal have C_{2h} symmetry at low temperatures (Ref. 47). The calculated energy difference, however, is only ~1 meV/molecule. Our results contradict those obtained in Ref. 58, where it was suggested that the D_2 isomer has a lower energy than the C_{2h} isomer. One possible reason for such a discrepancy is that in Ref. 58, a *semiempirical* method was used (CS-INDO), which is usually less accurate than *ab initio* methods. Finally, we note that the C_2 structure was unstable - during our calculations it relaxed to the C_2' conformation.

6.1.2.3. Group theory.

Similar to the analysis made for biphenyl, we applied group theory to analyze the normal modes of p-terphenyl. This analysis was performed for the three possible conformations shown in Fig. 24, as well as the planar conformation.

In the case of D_2 symmetry, the vibrational modes are classified as follows:

$$\Gamma = 22A \oplus 20B_1 \oplus 24B_2 \oplus 24B_3 \quad .$$

Modes belonging to the B_1, B_2, or B_3 irreducible representations are IR-active, for a total of 68 IR-active modes. For the C_{2h} group, the vibrational modes are classified as:

$$\Gamma = 21A_g \oplus 24B_g \oplus 21A_u \oplus 24B_u \quad .$$

Here, only modes belonging to either A_u or B_u representations are IR-active, yielding a total of 45 IR-active modes. For the molecule belonging to C_2 point group, the modes are given by:

$$\Gamma = 42A \oplus 48B \quad .$$

In this case, all modes are IR-active. For the planar configuration, p-terphenyl belongs to the D_{2h} point group. The vibrational modes are given by:

$$\Gamma = 16A_g \oplus 6A_u \oplus 5B_{1g} \oplus 15B_{2g} \oplus 9B_{3g} \oplus 15B_{1u} \oplus 9B_{2u} \oplus 15B_{3u} \quad .$$

Modes belonging to the B_{1u}, B_{2u}, or B_{3u} irreducible representations are IR-active, for a total of 39 IR-active modes.

Upon planarization, certain IR-active peaks become IR-forbidden. We would expect to see 6 modes disappear from the spectrum if p-terphenyl belongs to the C_{2h} group, 29 modes if it belongs to the D_2 group, and 51 modes if the molecule has C_2 symmetry. These “disappearing peaks” comprise a special subset of vibrational modes. In

the following discussion, we restrict the analysis to those modes that lose IR activity upon planarization.

6.1.2.4. Comparison between theory and experiment.

In Figure 28 we present all modes that are IR-inactive in the planar conformation, but become active in the C_{2h} and C_2' twisted conformations, along with the experimental results. The calculations showed that some modes, which are IR-active according to group theory, have essentially zero intensity. We then looked at the C_2' isomer, since it turned out it deviates from C_{2h} symmetry only slightly, as the difference in the twist angles of outer rings is only 0.03°. There is also a distortion of phenyl rings which makes them non-planar, but this distortion is also very small—the C-C-C-C dihedral angle is 0.04°. Results are also presented for the D_2 isomer. The results for C_2'' (not shown) are nearly identical to those for D_2.

In Fig. 28 it is apparent that the most intense calculated peak is at 710 cm^{-1}, consistent with experiment. For the D_2 calculations there is also an intense peak at 741 cm^{-1}. In the experimental spectrum, however, there is no disappearing peak near 741 cm^{-1}. This observation, along with the ground state energy calculations, allows us to conclude that the p-terphenyl structure is C_2'. Since the C_2' conformation deviates from the C_{2h} conformation only slightly, it is surprising that this small perturbation causes large increases in the intensities of certain IR peaks. In Fig. 28, for example, the IR mode at 710 cm^{-1} has zero intensity for the C_{2h} conformation, but it is very intense for the C_2' conformation.

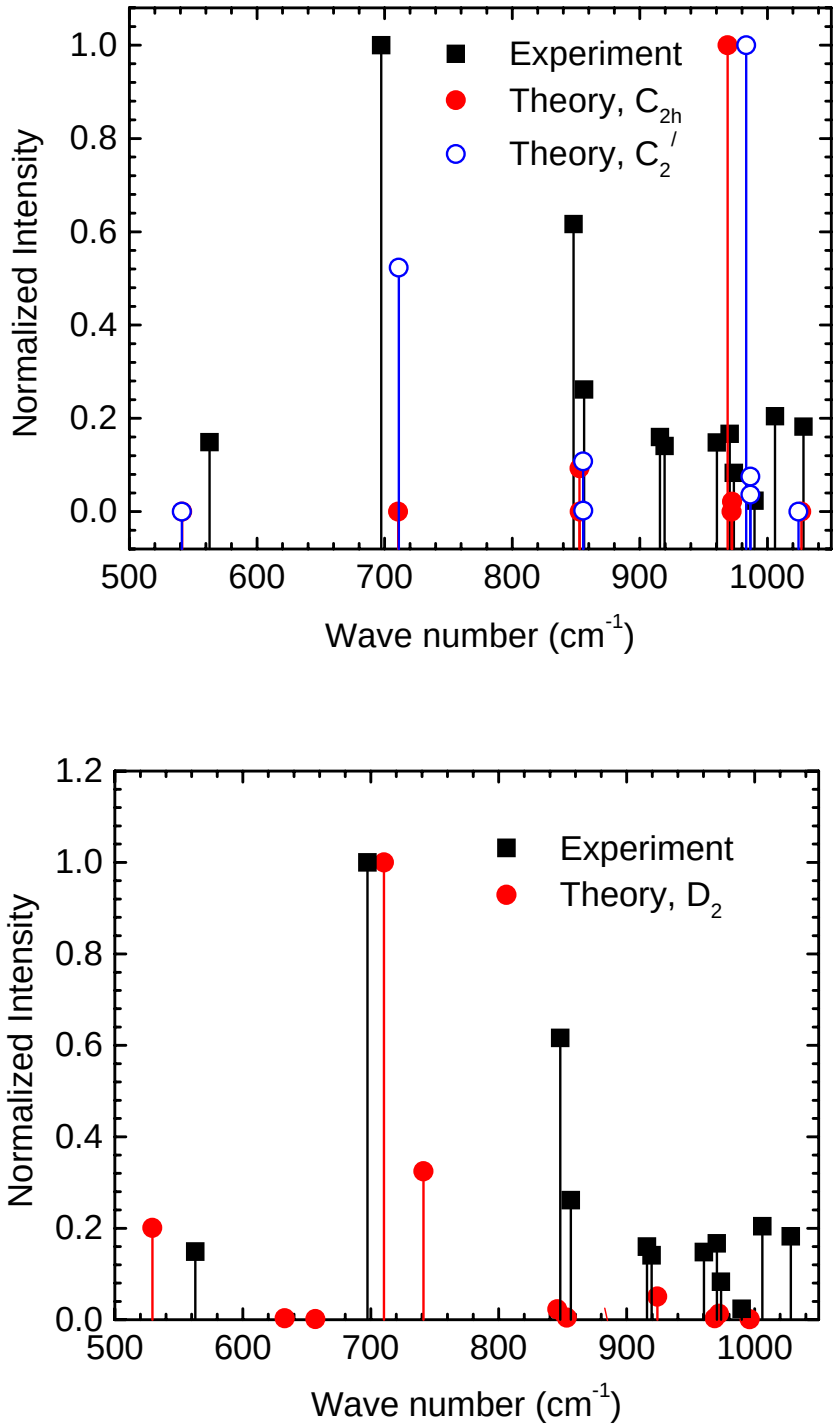

Figure 28 Comparison between experimental and calculated frequencies for p-terphenyl modes that become IR-inactive upon phase transition for different possible twisted conformations.

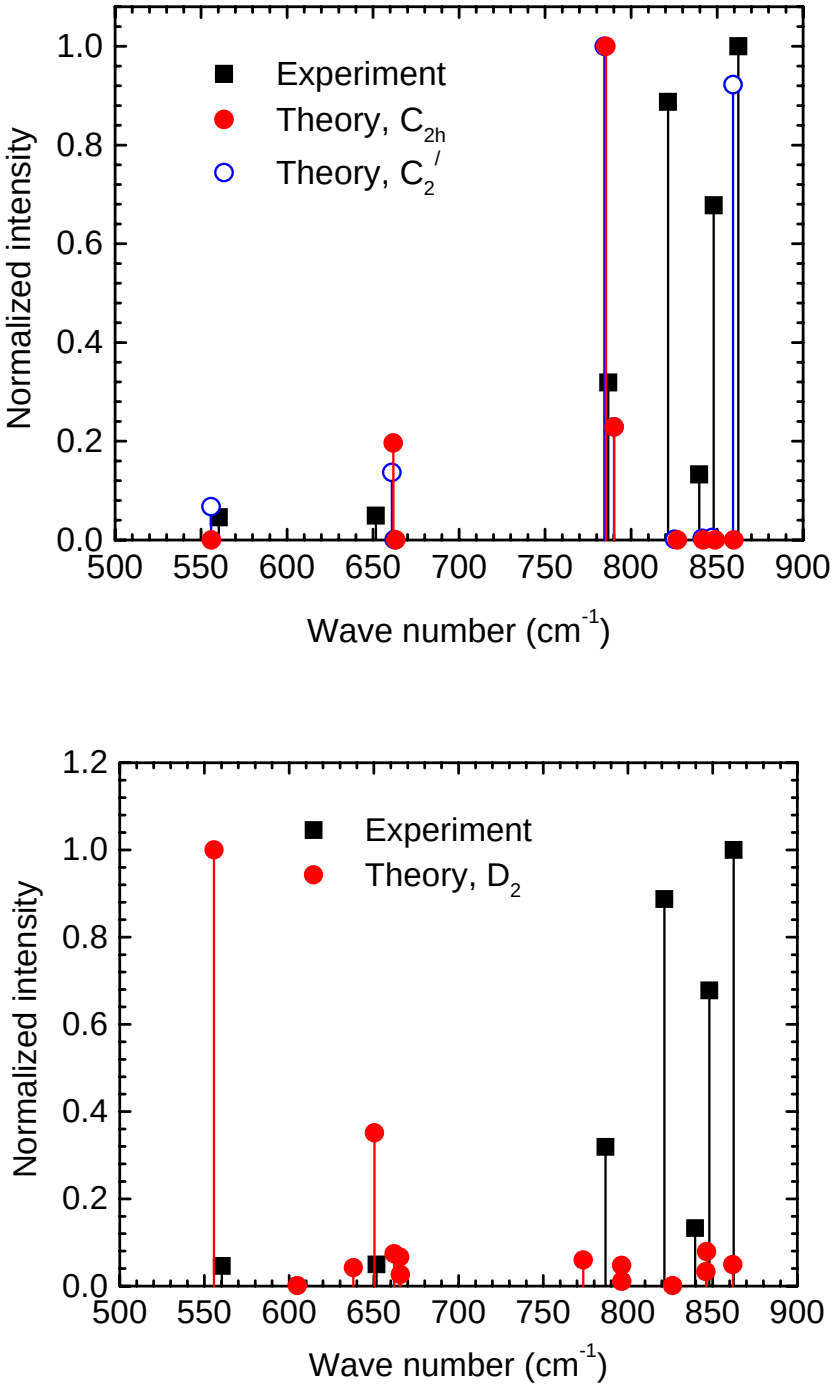

Figure 29 Comparison between experimental and calculated frequencies for deuterated p-terphenyl modes that become IR-inactive upon phase transition for different possible twisted conformations.

We have also performed calculations for deuterated p-terphenyl. The results for calculated and experimental IR modes are shown in Fig. 29. It is again seen that the C_2' conformation yields the best match between theory and experiment. For the D_2 conformation, however, there is an intense peak, calculated at a frequency of 550 cm^{-1}. Since experiments gave no evidence of such a strong peak in the spectrum, this calculation provides additional evidence that the D_2 configuration is incorrect.

It should be noted that the experimental peaks show fine structure that is not reproduced by the calculations. In 900-1000 cm^{-1} region (Fig. 28), for example, more peaks were observed in p-terphenyl than the calculations predicted. It is possible that this is due to Davydov splitting, which occurs when there is more than one molecule per unit cell. In p-terphenyl, there are two molecules per unit cell in the high-pressure phase and four molecules per unit cell in the low-pressure phase, where C_i is the site symmetry in both phases (Ref. 57). This causes the number of active modes to double. Of course, some modes may be very closely spaced and not resolved in our experiments.

6.1.2.5. Conclusions.

In conclusion, experiments on the vibrational properties of p-terphenyl showed that these molecules flatten under pressure, resulting in the disappearance of specific IR peaks. Using numerical calculations, we were able to evaluate the frequencies of the molecular vibrations and determine the structure of the molecule in its twisted conformation. The close correspondence between the calculated and experimental spectra indicates that in the twisted conformation, the central ring is rotated around C-C bond

relative to the plane of two other rings. This molecule has C_2 symmetry, as a result of a slight deviation from C_{2h} symmetry. Additional experiments and calculations on deuterated terphenyl support these conclusions.

6.1.3. P-quaterphenyl.

6.1.3.1. Experimental results

In this section, high-pressure IR spectroscopy experiments on biphenyl are discussed. Some of these results have been published in Ref. 95.

P-quaterphenyl is the next in the family of polyphenyl molecules. It has four phenyl rings and it is known to undergo a structural phase transition as well. Like biphenyl, p-quaterphenyl in its twisted conformation belongs to the D_2 point group of symmetry, i.e. the molecule loses its center of symmetry upon transition. It is known from x-ray diffraction studies[96] that in the twisted conformation the inner phenyl rings are at 23° to each other, and the angle between inner and outer rings is 17°. A picture of the molecule is shown in Fig. 30

Using the experimental setup described previously, we obtained the IR spectra of p-quaterphenyl at various pressure at liquid helium temperatures. Spectra were obtained with resolution 2 cm^{-1}. Two of those spectra, taken at pressures 0.7 and 1.9 GPa, are shown in Fig. 31. It is again evident, that certain IR modes disappear from the spectrum at high pressures. In Fig. 32(a) we plotted the frequency dependence for three peaks in the range 840-870 cm^{-1}. One mode disappears, while two other modes exhibit a

discontinuity in the slope of the frequency versus pressure plots. This is an indication of the phase transition. In Fig. 32(b) we provide further evidence for the presence of a phase transition. In this plot the area of the peak at 864 cm^{-1} was normalized with respect to the area of the peak at 860 cm^{-1} and plotted as a function of pressure. It is seen that the normalized area is zero within experimental uncertainty after the phase transition. The increase in the normalized area before the phase transition is due to the decrease in the area of the peak at 860 cm^{-1}.

6.1.3.2. Group theory.

Group-theoretical analysis of the vibrational modes of p-quaterphenyl yields the following results

$$\Gamma_{vibr} = 29A \oplus 27B_1 \oplus 32B_2 \oplus 32B_3$$

for the twisted conformation of the molecule. Modes that belong to B_1, B_2, and B_3 representations are IR-active. For the planar conformation we have:

$$\Gamma_{vibr} = 21A_g \oplus 8A_u \oplus 7B_{1g} \oplus 12B_{2g} \oplus 20B_{3g} \oplus 20B_{1u} \oplus 20B_{2u} \oplus 12B_{3u}$$

Here the modes belonging to B_{1u}, B_{2u}, and B_{3u} representations are IR-active. Thus in the planar conformation there are 52 IR-active modes and there are 91 IR-active modes in the twisted conformation. Therefore, some IR absorption peaks should disappear upon transition from the twisted to the planar conformation, in agreement with our observations.

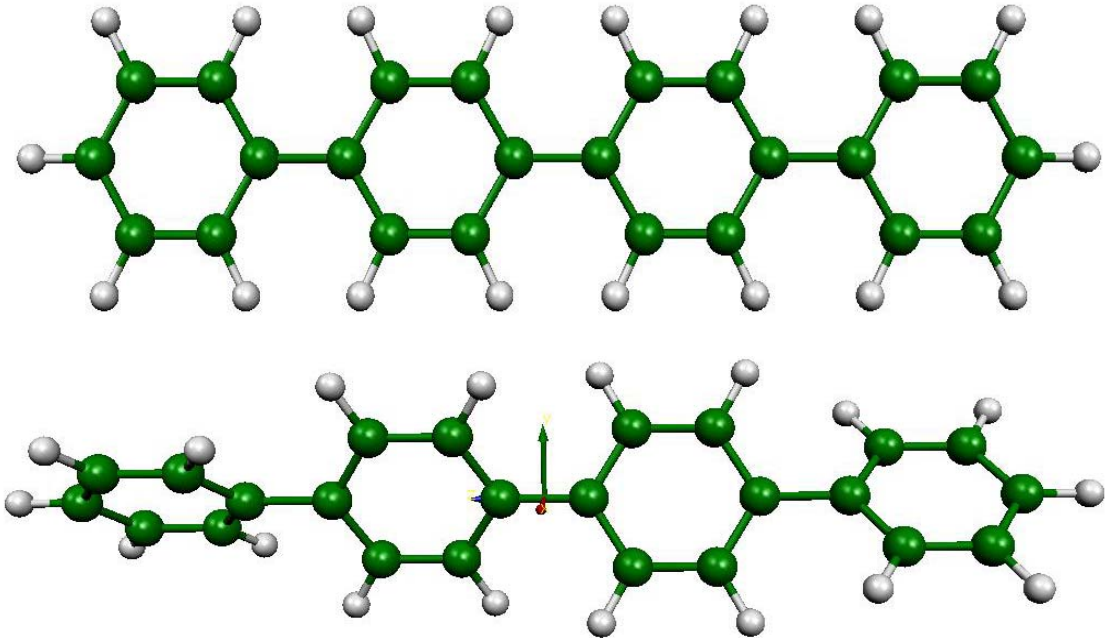

Figure 30. P-quaterphenyl molecule structure in the planar and twisted conformation.

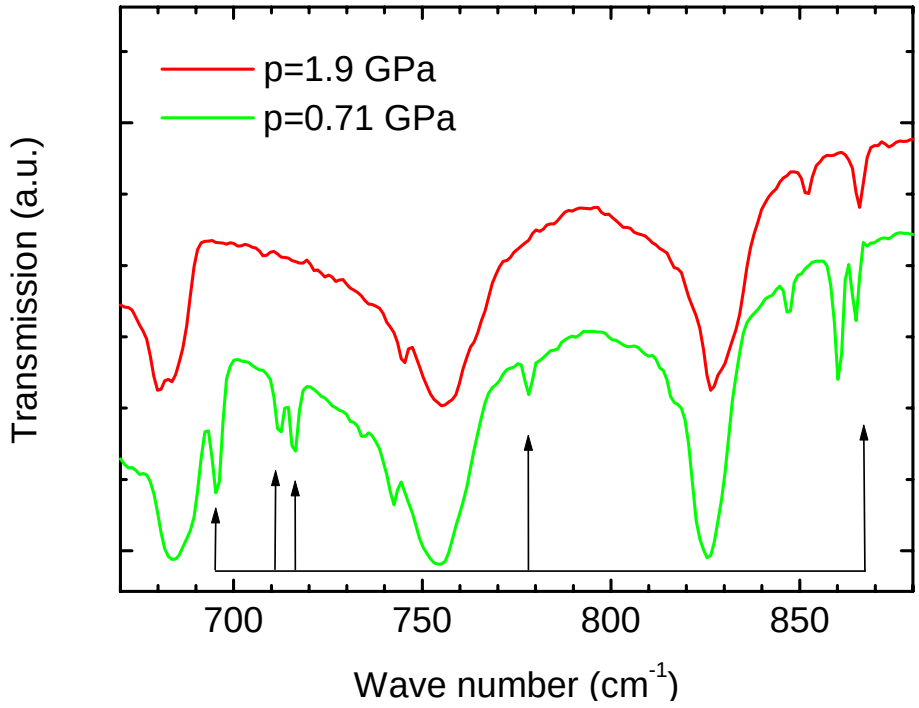

Figure 31. P-quaterphenyl spectra at pressures below and above phase transition.

IR-modes, that disappear upon transition, are indicated by arrows.

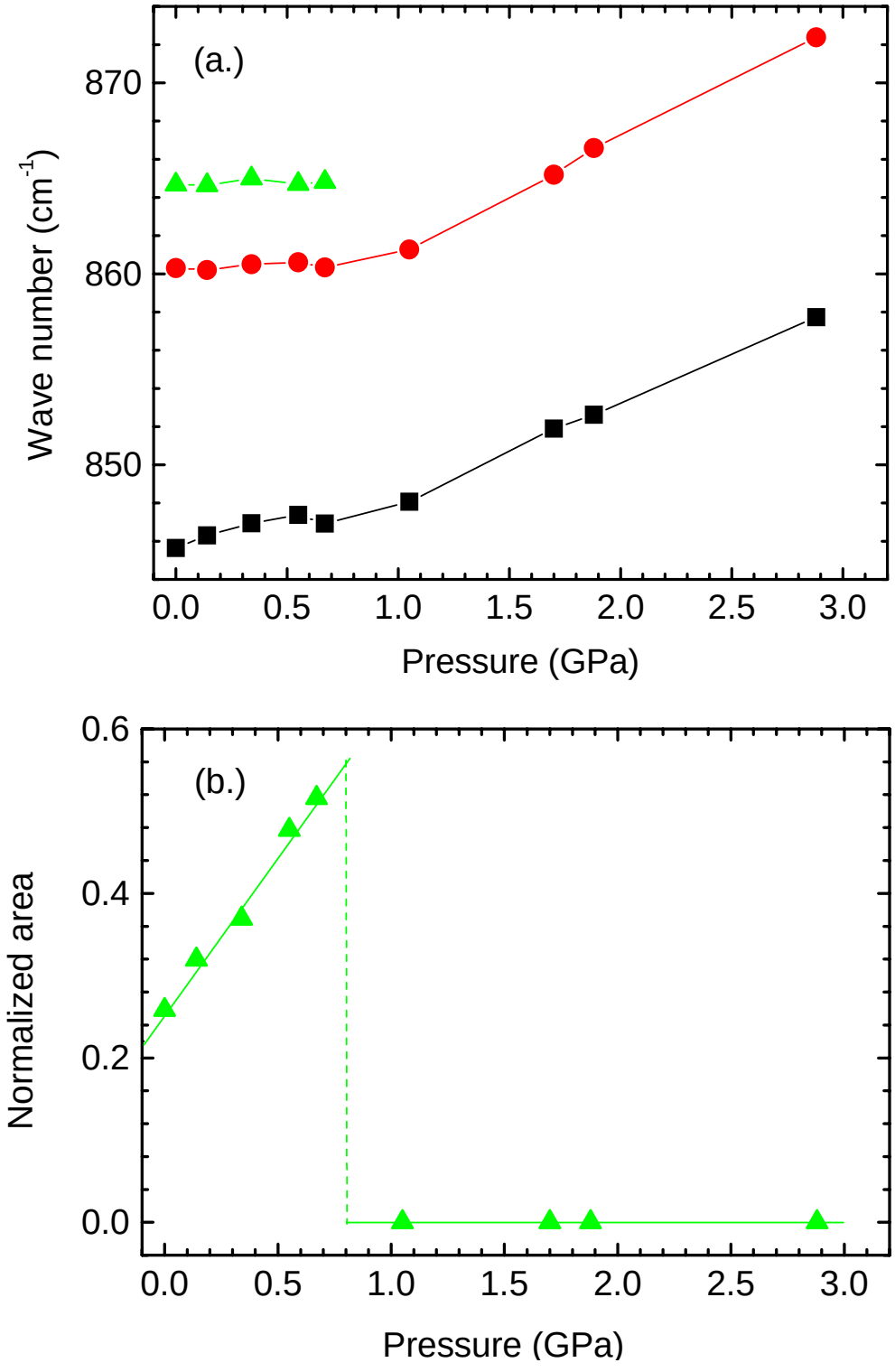

Fig. 32. Frequency dependence of several IR-modes on the pressure for p-quaterphenyl and normalized area dependence on the pressure for an IR-mode that become IR-inactive upon phase transition for p-quaterphenyl molecule.

The reason that we do not observe 39 disappearing peaks is probably due to the fact that some modes may be too weak to be observed, and others may be not resolved from neighboring peaks. In the 600-900 cm^{-1} region, which corresponds to the hydrogen out-of-plane bending modes, we observe five disappearing peaks. According to the group-theory analysis (not shown) there will be 9 IR modes, which disappear from the spectrum. But since four of them belong to B_1 representation and have the dipole moments induced to be very small, they may be too weak to be either resolved or detected. Thus we are left with five modes belonging to the B_3 representation, which become of B_{3g} representation and, therefore, lose IR-activity upon planarization of the molecule. In Fig. 34 we presented comparison between experimental and calculated frequencies of the modes that become IR-inactive upon the phase transition. The agreement is not as good as it was for biphenyl. It tends to become worse with the increase in the molecule size. The theory though also predicts five modes in the range from 600 to 900 cm^{-1} to disappear upon planarization of p-quaterphenyl molecule.

6.1.3.3. Conclusions.

In conclusion, the second-order phase transition was observed in p-quaterphenyl, as was for biphenyl and p-terphenyl. The critical pressure is about 0.9 GPa. The molecule becomes planar upon such a transition, which results in the disappearance of several IR peaks from the spectrum. Spectra are reproducible and no hysteresis behavior was found.

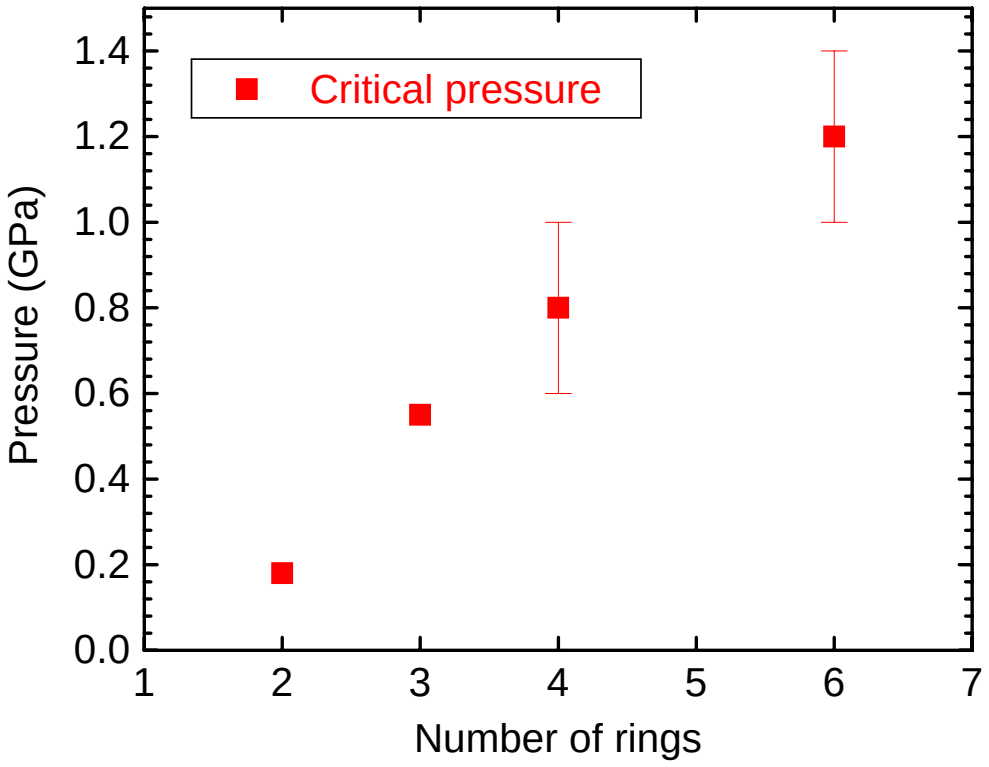

Figure 33. Critical pressure as a function of the number of phenyl rings.

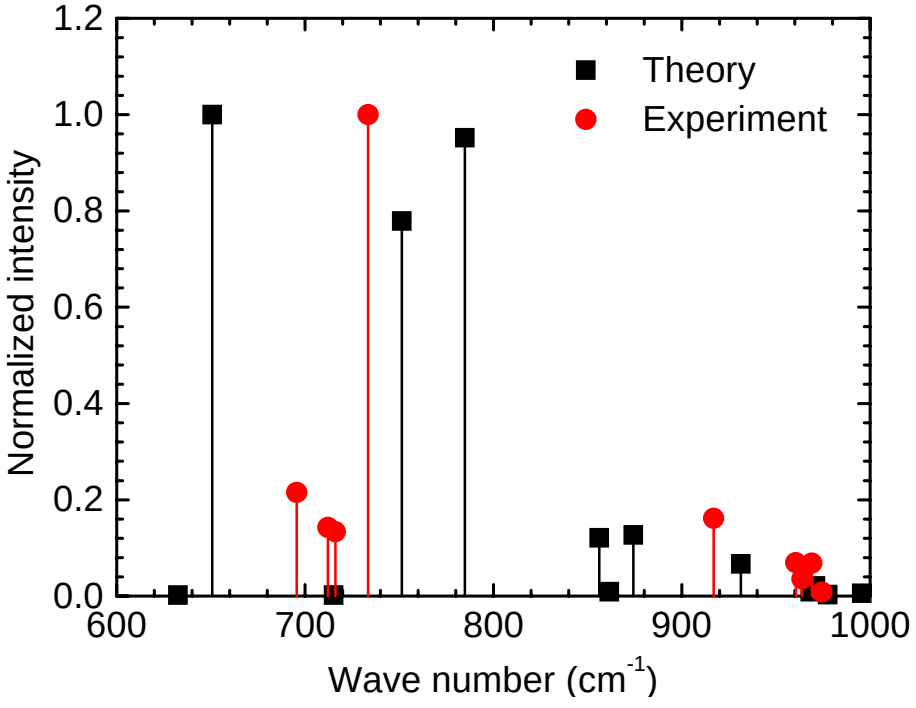

Figure 34. Comparison between experimental and calculated frequencies for p-quaterphenyl modes that become IR-inactive upon phase transition.

In Fig. 33 we give the critical pressure as a function of the number of phenyl rings in the conjugated molecule. The increase in critical pressure is explained by the increase in repulsion between hydrogen atoms, which tends to twist the molecule. Critical pressure values were taken from Ref. 36 and 89 for biphenyl, Ref. 65 for p-terphenyl, Ref. 95 for p-quaterphenyl, and Ref. 97 for p-hexaphenyl.

6.2. Surface-enhanced Infrared (SEIRS) and Raman (SERS) Spectroscopy.

In the previous chapters, high-pressure research on bulk solids was described. In order to investigate the effect of pressure on nanoscale systems, we have performed experiments on thin organic films. The eventual goal of this research is to systematically investigate pressure phenomena on materials, from a monolayer to bulk sizes.

To obtain sufficient IR absorption from nm-thick films, it is necessary to use surface-enhanced infrared absorption (SEIRA). In this chapter, previous work on SEIRA and self-assembled monolayers are described. Preliminary results on the high-pressure IR spectroscopy of nm-thick films are presented.

6.2.1. General description of the method.

The phenomenon of the enhancement of radiation absorption by molecules near metallic layers has been observed more than two decades ago[98]. This phenomenon was

called surface-enhanced infrared absorption (SEIRA) and has become a very powerful method for studying chemical contaminants and molecular monolayers. Substantial research effort has been made to study SEIRA. Among the organic chemical compounds the most studied include p-nitrothiophenol[99,100], disulfide and diselenide molecules[101], dichalogenide molecules[102], and p-nitrobenzoic acid[103,104,105]. Inorganic compound have also been studied by this technique[106,107]. In all these studies it has been found that the IR-absorption greatly (10^3-10^4 times) increases for certain IR-modes if the molecule is located near the metallic layer. The metals that show the most prominent enhancement are silver (Ag), lead (Pb), platinum (Pt), gold (Au), and copper (Cu). Not all modes are enhanced equally, which indicate the selective character of this process. A detailed review of the SEIRA can be found in Ref. 108.

It is now generally accepted that there are three major mechanisms that contribute to the total enhancement: electromagnetic, chemical, and orientational mechanisms. The orientational mechanism is the simplest and is due to the fact that the absorption of light is proportional to $\cos^2\theta$, where θ is the angle between the dipole moment derivative with respect to normal coordinate and the electric field of the incident radiation. Since the space average of $\cos^2\theta$ is 1/3, the orientational mechanism can provide an enhancement by a factor of three at most. The chemical mechanism of enhancement involves the chemical interaction between the molecule and the metal surface. It is known that chemisorbed molecules absorb stronger than physisorbed ones. It is believed that the charge transfer from the metal to the molecule contributes to enhancement, and some experiments seem to support this theory[109,110,111].

The electromagnetic mechanism of IR-absorption enhancement has been very extensively studied from both experimental and theoretical point of view[112,113,114,115,116,117,118,119,120]. It is now generally accepted that the excitation of plasmons in metal and their coupling with molecular vibrations is the main mechanism for the electromagnetic enhancement of IR- and Raman signal. The enhancement greatly depends on the metal surface morphology[121], which indicates that the surface structure is the important factor in achieving larger enhancements. Below we consider the electromagnetic mechanism in more detail, following the review given in Ref. 120.

6.2.2. Electromagnetic (EM) mechanism of surface-enhanced absorption.

If electromagnetic radiation impinges onto the metal surface, the local field near the surface is different from the field far away from it. In practice, the metal surface is usually rough and the roughness size varies from nanometers to microns. We are interested in the metals deposited from the vapor or by a sputtering process, where the size of the metal particles is 1-100 nm. In this case the particle size is much smaller than the wavelength of radiation. In this case the electric field can be assumed to be uniform, but varying in time. The retardation effects can all be neglected and the polarization of the spherical metal particle is determined by a well-known result:

$$\vec{\mathbf{P}} = 3\varepsilon \frac{\varepsilon_{\text{met}} - \varepsilon}{\varepsilon_{\text{met}} + 2\varepsilon} \vec{\mathbf{E}} \quad , \tag{113}$$

where ε and ε_{met} are dielectric constants of surrounding medium and the metal, respectively. The case of non-spherical particles will be addressed later.

The polarization given by Eq. (113) corresponds to the dipole moment $\vec{\mathbf{p}} = \frac{4}{3}\pi a^3 \vec{\mathbf{P}}$, where a is the radius of the sphere. The electric dipole field is then given by:

$$\vec{\mathbf{E}}_{\text{dip}} = 4\pi a^3 \varepsilon \frac{(\varepsilon_{\text{met}} - \varepsilon)e^{i(kr-\omega t)}}{(\varepsilon_{\text{met}} + 2\varepsilon)r} E_0 \left\{ k^2 (\hat{\mathbf{n}} \times \hat{\mathbf{e}}) \times \hat{\mathbf{n}} + [3\hat{\mathbf{n}}(\hat{\mathbf{n}} \cdot \hat{\mathbf{e}}) - \hat{\mathbf{e}}] \left(\frac{1}{r^2} - \frac{ik}{r} \right) \right\} \qquad (114)$$

Here $\hat{\mathbf{e}}$ is the unit polarization vector of the incident radiation (not to be confused with the polarization of the metal particle from Eq. (113)!), r is the radial distance from the center of the spherical particle, $\hat{\mathbf{n}} = \frac{\vec{\mathbf{r}}}{r}$ is the unit vector in the direction of $\vec{\mathbf{r}}$, and k is the wave vector of the incident radiation.

Eq. (114) already enables us to understand the mechanism of surface-enhancement. If the dielectric constant of the metal has small imaginary part and real part equal to -2ε, the electric field given by Eq. (114) becomes very large. The absorption and scattering intensities are proportional to the square of the electric field and thus become very large too. The total electric field is the sum of the incident and scattered fields and can be written as:

$$\vec{\mathbf{E}}_{\text{tot}} = \vec{\mathbf{E}}_{\text{inc}} + \vec{\mathbf{E}}_{\text{dip}} = \left(\hat{\mathbf{e}} + \eta \left\{ \frac{k^2}{r} (\hat{\mathbf{n}} \times \hat{\mathbf{e}}) \times \hat{\mathbf{n}} + [3\hat{\mathbf{n}}(\hat{\mathbf{n}} \cdot \hat{\mathbf{e}}) - \hat{\mathbf{e}}] \left(\frac{1}{r^3} - \frac{ik}{r^2} \right) \right\} \right) E_0 e^{i(kr-\omega t)} \qquad (115)$$

where $\eta = 4\pi a^3 \varepsilon \frac{\varepsilon_{\text{met}} - \varepsilon}{\varepsilon_{\text{met}} + 2\varepsilon}$ and E_0 is the amplitude of the incident electric field.

The more realistic model of the experiments on surface-enhanced spectroscopy is the collection of spheres coated with the layer of material under investigation. As the first-order approximation one can assume that all spheres are of the same radius and the spacing between spheres is much larger than the sphere radius. In this case each sphere can be considered independently and the problem reduces to the two-layered sphere in

the uniform electric field. The problem is exactly solvable and the final result gives the electric field outside the sphere in the form:

$$\vec{\mathbf{E}} = \mathrm{E}_0\left\{\hat{\mathbf{z}} + \left[\mathrm{R}_1^3\left(\frac{\bar{\varepsilon}-1}{\bar{\varepsilon}+2}\right)\right]\frac{3\hat{\mathbf{n}}(\hat{\mathbf{z}}\cdot\hat{\mathbf{n}})-\hat{\mathbf{z}}}{\mathrm{r}^3}\right\} \tag{116}$$

where R_1 is the radius of the outer coating layer surface, r is the radius-vector, and $\bar{\varepsilon}$ is the so-called *effective medium dielectric constant*. The value of $\bar{\varepsilon}$ is given by:

$$\bar{\varepsilon} = \varepsilon_1\left[1 + \frac{3\mathrm{f}(\varepsilon_2-\varepsilon_1)}{(\varepsilon_2+2\varepsilon_1)-\mathrm{f}(\varepsilon_2-\varepsilon_1)}\right] \tag{117}$$

where ε_1 and ε_2 are dielectric constants of the coating layer and the inner spherical particle, respectively, $\mathrm{f} = \mathrm{R}_2^3/\mathrm{R}_1^3 = \frac{\mathrm{V}_{\mathrm{sphere}}}{\mathrm{V}}$ is the filling factor, and R_2 is the inner sphere radius. The Eq. (117) coincides with the famous result of Maxwell-Garnett theory[122] (MGT) for small spherical particles with dielectric constant ε_2 embedded in the medium with dielectric constant ε_1. The condition in MGT that the spheres can be considered independently requires the filling factor to be small. In our case the spacing between spherical particles must be large compared to their size. In this case the influence of one sphere onto another can be neglected.

Since the composite medium was treated as the homogeneous medium with effective dielectric constant, the theory described is *effective medium theory* (EMT). Another EMT is the Bruggeman theory[123]. More detailed review can be found in Ref. 108, 114.

Alternative theories have also been developed[124,125,111,118]. In those theories the metal particles and the molecules are replaced by polarizable dipoles $\vec{\mathbf{p}}_i$ The magnitudes of the dipoles are determined via the following coupled dipoles (CD) equation:

$$\vec{\mathbf{p}}_i = \alpha_i \left(\vec{\mathbf{E}}_0 + \sum_{j \neq i} M_{ij} \vec{\mathbf{p}}_j \right) \quad . \tag{118}$$

Here α_i is the polarizability of the i^{th} dipole and M_{ij} describes the interaction between the i^{th} and j^{th} dipoles. The value of M_{ij} is given by the second term in parentheses in Eq. (115) where the vector $\vec{\mathbf{r}}$ must be replaced by $\vec{\mathbf{r}}_{ij}$, the vector from the i^{th} to j^{th} dipole position. The Eq. (118) must be solved self-consistently. Recent calculations showed good agreement between experimental and computed data, as well as consistency among different theories[126,118,119,120].

All models considered above have implicitly assumed that the particles are big enough to be treated as macroscopic medium with dielectric constant determined for such a medium. It is known, however, that the dielectric constant becomes size dependent for very small particles. In fact, the size dependence manifests itself when the size of the particle becomes comparable to the mean free path of conducting electrons. This changes the plasmon width and, for spherical particles, can be described by the following relation:

$$\gamma = \gamma_b + A \frac{v_F}{R} \quad , \tag{119}$$

where v_F is Fermi velocity and R is the radius of the sphere. Coefficient A in Eq. (119) is equal to 1 in classical theory and ranges from 0.76 to 1.16 in various quantum-mechanical models[127,128]. The detailed review on this subject can be found elsewhere.

6.3. Thin films of organic molecules under pressure.

Thin molecular and atomic films and self-assembled monolayers (SAM) have recently become a subject of intensive scientific research. They have been studied experimentally by atomic force microscopy[129,130,131] (AFM), scanning tunneling microscopy[132,133,134,135] (STM), X-ray diffraction[136,137,138,139], transmission electron microscopy, x-ray photoelectron spectroscopy[140,141] (XPS), sum-frequency generation[142] (SFG), surface second harmonic generation[143,144] (SSHG), Brewster angle microscopy[145], ellipsometry[146,140,141], Raman scattering[147], infrared (IR) spectroscopy[133,134,135,148,149,150,151,141], and theoretically by molecular dynamics simulations[152,153,154,155].

It is known that thiol molecules form layered structures on different substrates such as metal surfaces, silicon, and glasses. The most studied are alkenethiol, benzenethiol, thiophenol and some others. The most frequently used substrate is gold (Au). The alkenethiol molecules deposited on Au(111) can form $\left(\sqrt{3}\times\sqrt{3}\right)\mathrm{R}30^{\circ}$ or 1×1 structures. The application of surface pressure drives the transition and hysteresis was observed. The $\left(\sqrt{3}\times\sqrt{3}\right)\mathrm{R}30^{\circ}$ structure persists up to a load of 280 nN and then 1×1 structure appears. Upon decreasing the load the $\left(\sqrt{3}\times\sqrt{3}\right)\mathrm{R}30^{\circ}$ structure reappears only at a load about 100 nN. The global phase diagram of n-alkenethiol SAM has been investigated and two regimes have been found: long (n>14) and short ($n \le 12$) chain-length regimes. Different phases are characterized by the tilt direction and two-dimensional periodicity. The tilt angle was found to be about 30-35° from normal to the surface[136,148]. The molecular dynamics simulations showed that there are two phase

transitions in SAM of alkylthiol molecules: one is a change in tilt direction from nearest neighbor (NN) to next-nearest neighbor (NNN) and another is a transition from NNN tilt to an orientationally disordered state. A similar transition was found in the SAM of azobenzene derivative, 4-octyl-4′-(carboxytrimethyleneoxy)azobenzene (C_8AzoC_3). The low-pressure phase has the tilt toward NN whereas high-pressure phase has the tilt toward NNN. It was found that the tilt angle does not change much with pressure.

Pyridine molecules on Au(111) form various structures with flat-lying, tilted, and vertically standing molecules. In this case the tilt angle varies from 20 to 45° and increases as the applied surface potential or surface concentration increases. The same group of researchers studied 2,2′-bypyridine (bpy) SAM and found two phase transitions as applied potential increases. One transition is from flat to vertically oriented molecules and another one is from $3\times 4\sqrt{3}$ zigzag to $4\times 2\sqrt{3}$ commensurate structure.

Another large group of thiol molecules, which form SAMs, are aromatic molecules. The simplest molecule is benzenethiol. It forms a well-ordered monolayer with a $\left(\sqrt{13}\times\sqrt{13}\right)$R13.9° commensurate structure. As shown by STM and surface-enhanced infrared absorption (SEIRA), the phenyl ring is tilted about 30° from surface normal. Also p-biphenyl mercaptan (BPM) and p-terphenyl mercaptan (TPM) have been studied and it was determined that they form stable monolayers with reproducible contact angles. The structure of these monolayers is $\left(\sqrt{3}\times\sqrt{3}\right)$R30° and molecules are almost perpendicular to substrate surface.

The pressure effect on thin films has been also investigated. In Ref. 147 it was found that in the polydiacetylene the phonon frequencies increase, but the Raman frequencies shift to the red part of the spectrum. This behavior was attributed to the

increase of conjugation length with pressure. In 1,2-dipalmitoyl-*sn*-glycero-3-phosphocholine (DPPC) the surface pressure application leads to the increase in frequency of C-H vibrations and in the signal intensity. These findings, as will be seen below, are consistent with our own observations.

6.4. Current research.

6.4.1. Film preparation.

A silver film was deposited onto the culet surface of the diamonds in the DAC by the vapor deposition method. The scheme of the deposition system is shown on Fig. 35. The DAC was placed into the deposition chamber and the chamber was evacuated to about 10^{-7}-10^{-9} Torr. First, the roughing pump brought pressure down to 100 Torr. Then the cryopump was opened to the ambient atmosphere and heated up to 500° C. After several hours of heating it was isolated from the atmosphere and cooled down to liquid nitrogen temperature (77 K). When thermal equilibrium was reached, the valve, connecting the cryopump with the deposition chamber, was opened and the pressure decreased to a level of ~1 mTorr. The final stage involves the ion pump evacuating the whole chamber. The valve between the ion pump and the chamber was slowly opened and the pressure in the ion pump was monitored and not allowed to exceed 10^{-5} Torr. The filaments of the ion pump operated with ~50 A current in continuous or 2-5 minute cycle mode. It usually takes 1-2 hours for the ion pump to bring the pressure down to the values mentioned above. During the operation the ion pump must be cooled by a continuous

water flow. The deposition current can vary in the range 175-250 A and the rate of silver deposition varies in a wide range from 0.1 to 100 Å/s. A manually operated shutter allows one to control the deposition time and, thus, the film thickness. In order to monitor the thickness correctly the deposition rate should not exceed 5 Å/s. However, the higher the deposition rate, the rougher the film surface is, which is important for the surface enhanced spectroscopy.

For the purpose of SEIRA measurements the silver film thickness must be small enough in order not to block the infrared light passing through the diamonds. At the same time the film must provide sufficient enhancement of the IR absorption so that the IR detector receives sufficient signal. Usually the film thickness is about 10 nm for good enhancement, but we have used a 5 nm thick film to get a good signal to noise ratio. Since the enhancement is greater for a film with rougher surface profile, we chose a deposition rate of about 5 Å/s.

Thin film of p-NTP has been casted from the solution onto the silver layer covering diamond surface. This technique of organic thin film preparation has been described elsewhere. In order to protect the epoxy, which glues diamonds to the backing plates, from the chemical solution we put additional layer of epoxy after silver film deposition. The AFM images of p-NTP thin film have been taken after a series of high-pressure experiments (Appendix D). They showed a film of about 30 nm thick (Fig. 38, 39). Large white features in the image are dust particles and small ruby chunks, which are inevitably introduced in the loading process.

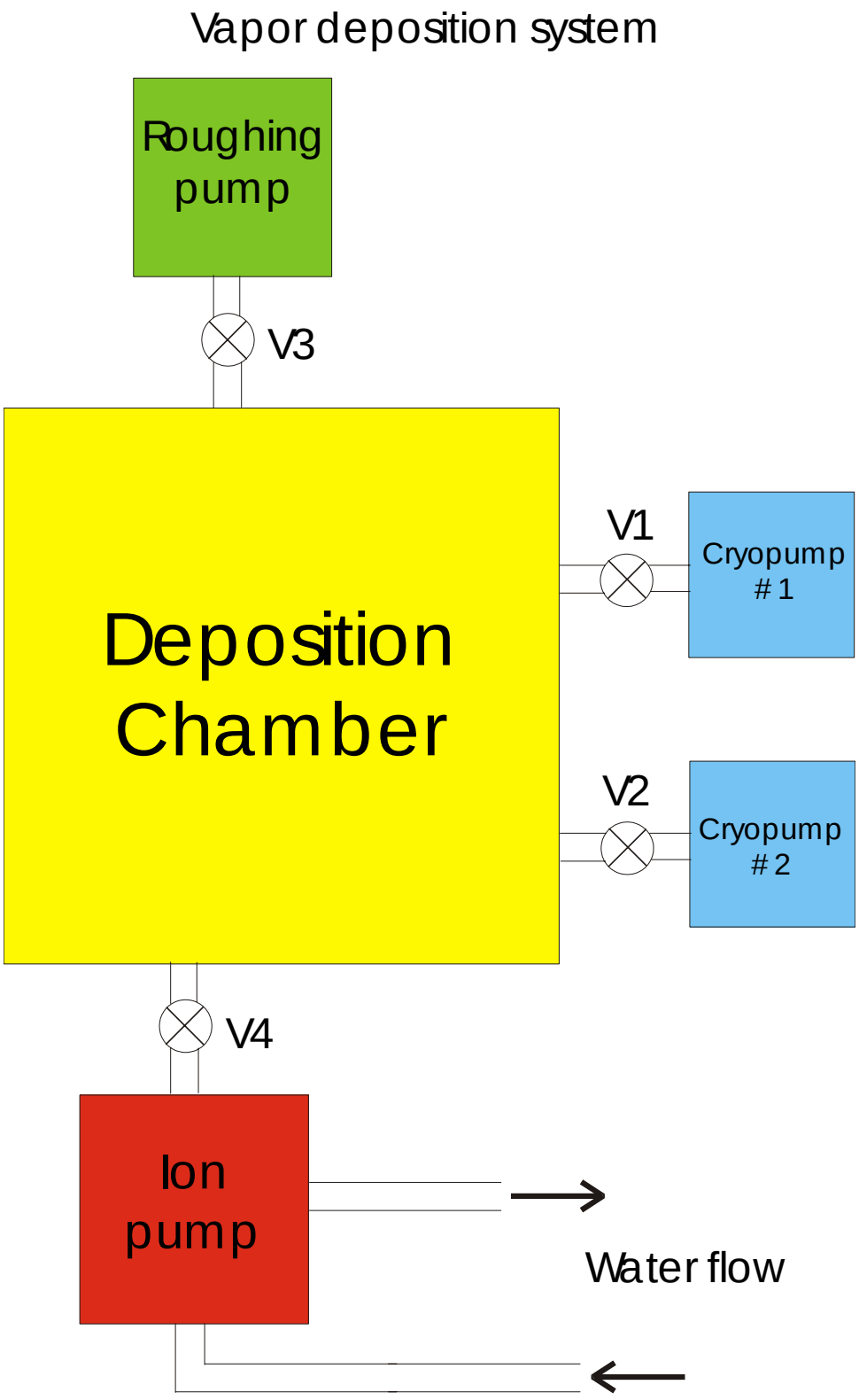

Figure 35. The schematic picture of the vapor deposition system used in depositing thin silver films onto diamond.

A more detailed structure could be possibly obtained by STM measurements, which we didn't perform. The deposited film has been loaded with liquid nitrogen in the DAC with type II diamonds and FT-IR spectra have been taken. The pressure was calibrated using ruby fluorescence method. For this purpose the tiny ruby chip was placed on top of the film. The introduction of the ruby chip inevitably damages the thin film. In our case, however, the size of the chip was negligible compared to the sample size. Thus no significant damage to the film has been done.

6.4.2. Results.

Typical spectra of the thin p-NTP film are shown in Fig. 36. The broad peak at 1340 cm^{-1} corresponds to a symmetric stretch of NO_2 group in the p-NTP molecule. Spectra have been obtained at the room temperature with an MCT detector. The spectral resolution was 8 cm^{-1}. In the Fig. 37 we present peak frequency as a function of pressure. The frequency shifts up with pressure, though the apparent shift is smaller than the resolution. Thus no certain conclusions can be drawn about its behavior now and a more sensitive technique is required. Nevertheless, the pressure seems to affect the film significantly enough so that IR-spectroscopy can serve as a probe of film behavior under high pressures. Upon decrease of the pressure the peak intensity went down, which made it hard to detect the peak at pressures between 1 and than 5 GPa. But then the intensity is increased at the pressures below 1 GPa. Whether it is due to a phase transition in the nitrogen, which occurs at 1.9 GPa, is currently not known.

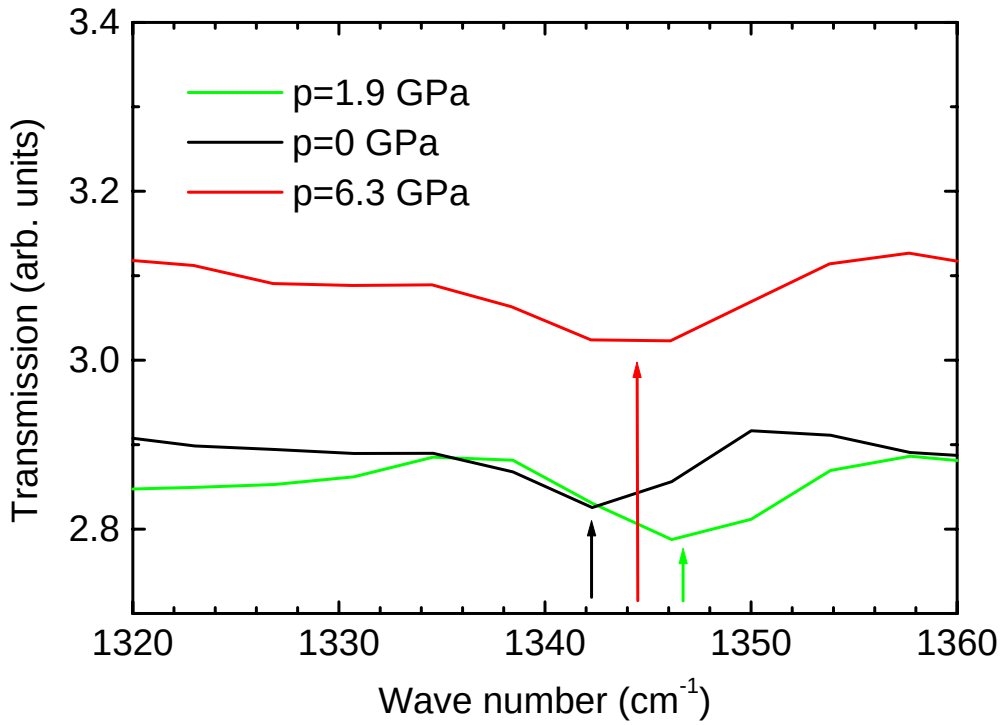

Figure 36. Typical IR spectra of p-NTP film at different pressures.

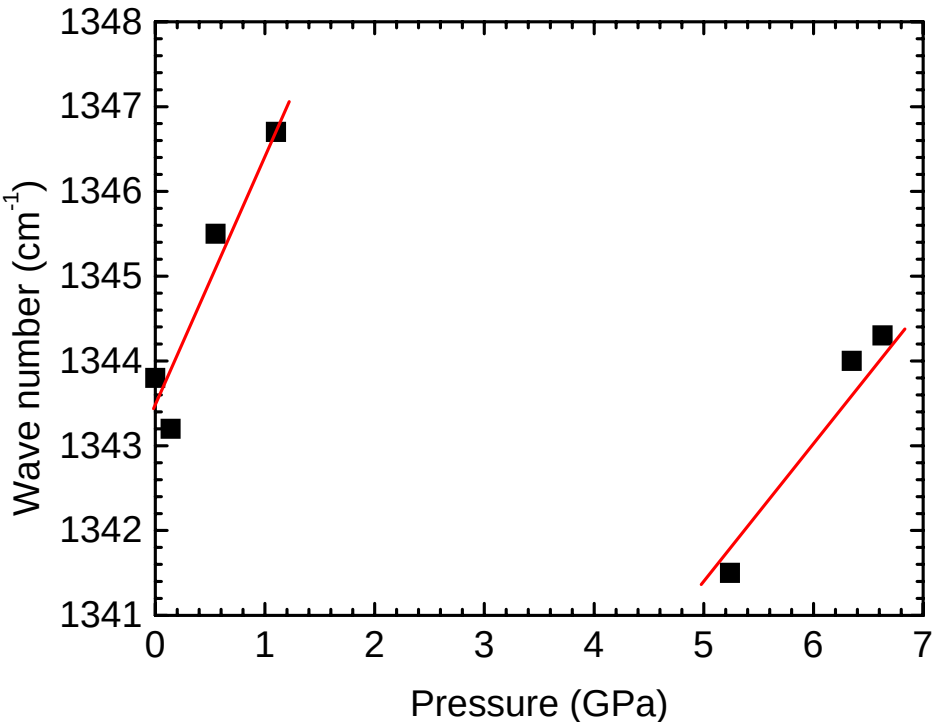

Figure 37. Pressure dependence of NO_2 symmetrical stretch mode frequency in p-NTP film.

Overall, application of the pressure to thin films seems to influence the vibrational frequencies of the molecules composing the film and can serve as a good probe of the film properties. Much of the research has to be done in this area and a lot of discoveries are still waiting to be made.

7. Summary of results

In this work the following results have been obtained:

- High pressure can be applied to the study of organic solids and thin films of organic materials;
- Biphenyl, p-terphenyl, and p-quaterphenyl all undergo structural phase transitions when pressure increases above certain critical value;
- Several IR modes become inactive upon this transition;
- The critical pressure increases with the number of phenyl rings;
- Among two possible twisted conformations of p-terphenyl, the conformation belonging to the C_{2h} symmetry is the most stable;
- Numerical *ab initio* calculations show very good agreement with experiment;
- Thin films of organic molecules can be successfully studied by means of surface-enhanced IR absorption method. High pressure affects the thin film properties;

Most of these results have been published in peer-reviewed journals and presented at various meetings.

8. Future work directions

A new branch of research in physics and chemistry is connected with the properties of self-assembled monolayers. A monolayer provides a model system to study materials properties on the nanometer length scale. Those materials should exhibit interesting mechanical, optical and other physical properties. Quasi-two-dimensional systems can lead to discoveries of new phenomena. Pressure-induced phase transitions in such systems might be a good test for existing theoretical models, such as Ising or Potts models, which have been successfully applied to various surface phenomena[156], and a way to develop new, more sophisticated models to describe behavior of two-dimensional systems. Pressure in this case can also be a very powerful tool to probe atomic interactions between monolayer molecules. I have been studying pressure effects on p-nitrothiophenol monolayers grown on metallic substrates by means of infrared (IR) spectroscopy. There exists several surface characterization techniques, such as scanning tunneling microscopy (STM), atomic force microscopy (AFM), and surface second harmonic generation (SSHG), to study the effects of high pressure.

High pressure can be a very useful characterization tool for the investigation of the thin films. By systematically increasing the thickness of the film, one can probe bulk vs. surface properties of a material. By monitoring changes in the material's response to applied pressure with increasing thickness, one can find out when this material starts exhibiting bulk behavior. IR spectroscopy can provide a direct indication to some changes within the material. The research in this area can lead to a deeper understanding of the structure of different substances and may result in discoveries of novel materials.

9. List of publications

Here is the list of all the publications resulted from the work. Those relevant to this thesis are underlined.

- McCluskey M. D., Zhuravlev K. K., Davidson B. R., and Newman R. C. Physical Review B, vol. 63, pp. (2001).
- Zhuravlev K. K. and McCluskey M. D. Journal of Chemical Physics, vol. 114, no. 13, pp.5465-5467 (2001).
- McCluskey M. D., Zhuravlev K. K., Davidson B. R., and Newman R. C. Physica B, vol. 308-310, pp. 780-783 (2001).
- McCluskey M. D. and Zhuravlev K. K. Journal of Chemical Physics, vol. 116, no. 4, pp. 1607-1611 (2002).
- McCluskey M. D., Zhuravlev K. K., Kneissl M., Wong W., Treat D., Limpijumnong S., Van de Walle C. G., and Johnson N. M. Mat. Res. Symp.Proc. Vol. 693, I2.4.1-I2.4.6 (2002).
- Zhuravlev K. K. and McCluskey M. D. Journal of Chemical Physics, vol. 117, no. 8, pp. 3748-3752 (2002).
- McCluskey M.D., Grover D.I., and Zhuravlev K.K. Chemistry Letters, pp. 1138-1139 (2002).
- McCluskey M.D., Jokela S.J., Zhuravlev K.K., Simpson P.J., and Lynn K.G. Applied Physics Letters, vol. 81, no. 20, pp. 3807-9 (2002).
- Zhuravlev K. K. and McCluskey M. D. Journal of Chemical Physics, vol. 120, no. 4, pp. 1841-1845 (2004).

APPENDIX A.

Absorption of light. Quantum-mechanical treatment.

Let us consider a quantum-mechanical system with an energy spectrum $E_n, n = 1, 2, \ldots$. If a perturbation $V(t)$ is acting on the system, then the probability for the system to go from the initial state $|i\rangle$ to some final state $|f\rangle$ is given by the expression[4]:

$$P_{fi} = \frac{1}{\hbar^2}\left|\int_{-\infty}^{+\infty}\langle f|V(t)|i\rangle e^{i\omega_{fi}t}\,dt\right|^2 \qquad (A1)$$

where $\omega_{fi} = \frac{E_f - E_i}{\hbar}$. The perturbation is assumed to be zero at $t \to \pm\infty$. If the perturbation is turned on at t=0 and is periodic with frequency ω, $V(t) = V_0 e^{-i\omega t}$, then the probability of the transition is given by:

$$P_{fi} = \frac{2\pi}{\hbar}\left|(V_0)_{fi}\right|^2 t\delta(E_f - E_i - \hbar\omega) \qquad (A2)$$

The probability is proportional to the time. But the transition rate, i.e. the probability per second, is independent of time and is equal to:

$$r_{fi} = \frac{2\pi}{\hbar}\left|(V_0)_{fi}\right|^2 \delta(E_f - E_i - \hbar\omega) \qquad (A3)$$

In the case of light absorption, the system is interacting with a plane electromagnetic wave. The Hamiltonian of the system contains the term $-\frac{1}{c}\vec{\mathbf{A}}\cdot\vec{\mathbf{p}}$, where $\vec{\mathbf{p}}$ is the momentum operator, as the perturbation.

If we take into account that $\vec{\mathbf{A}} = A_0\hat{\boldsymbol{\varepsilon}}e^{i\vec{k}\cdot\vec{x}}$, we obtain for the transition rate:

$$r_{fi} = \frac{2\pi}{\hbar c^2} A_o^2 \left| \left(e^{i(\omega/c)(\hat{\mathbf{n}}\cdot\vec{\mathbf{x}})}\, \hat{\boldsymbol{\varepsilon}} \cdot \vec{\mathbf{p}} \right)_{fi} \right|^2 \delta\left(E_f - E_i - \hbar\omega\right) \quad . \qquad \text{(A4)}$$

When the wavelength of the incident light is much greater than the size of the system, the exponential in Eq. (A4) can be replaced by 1. This is the so-called electric dipole (or E1) approximation. Assuming that the initial state is the ground state, and using the commutation relation $\vec{\mathbf{p}} = -i\left[\vec{\mathbf{r}} H_0\right]$, where H_0 is the unperturbed Hamiltonian, one obtains for the absorption rate from the ground state:

$$r_{fi} = \frac{2\pi\omega_{f0}^2}{\hbar^2 c^2} A_o^2 \left| \left(\hat{\boldsymbol{\varepsilon}} \cdot \vec{\mathbf{d}} \right)_{fi} \right|^2 \delta\left(\omega_{f0} - \omega\right) \quad , \qquad \text{(A5)}$$

where $\vec{\mathbf{d}}$ is the dipole moment of the system. Thus the absorption rate is proportional to the square of the matrix element of the dipole moment.

APPENDIX B.

Isotopic shift of the vibrational frequency of the molecule.

Let us consider the simplest case of a diatomic molecule consisting of two different atoms with masses $m_1^{(0)}$ and m_2, where superscript (0) is referred to the isotope type. The chemical bond between these atoms is described, in the harmonic approximation, by a force constant k. The vibrational frequency is given by:

$$\omega_0 = \sqrt{k/\mu}; \quad \mu^{-1} = \left(m_1^{(0)}\right)^{-1} + \left(m_2\right)^{-1} \tag{B1}$$

If one of the atoms is replaced by its isotope with the mass $m_1^{(1)}$, the vibrational frequency changes and becomes:

$$\omega_1 = \sqrt{k/\mu'}; \quad \mu'^{-1} = \left(m_1^{(1)}\right)^{-1} + \left(m_2\right)^{-1} \tag{B2}$$

The ratio of two frequencies is given by:

$$\frac{\omega_1}{\omega_0} = \sqrt{\frac{\mu}{\mu'}} = \sqrt{\frac{\left(m_1^{(1)}\right)^{-1} + \left(m_2\right)^{-1}}{\left(m_1^{(0)}\right)^{-1} + \left(m_2\right)^{-1}}} \tag{B3}$$

It is seen from B3 that if we replace the atom with its lighter isotope ($m_1^{(1)} < m_1^{(0)}$), the frequency is blue-shifted. If the isotope is heavier, the frequency will be red-shifted.

The most interesting case is when one of the atoms is hydrogen. The hydrogen atom is much more lighter that almost any other atom and in this case the ratio $m_1^{(0)}/m_2$ is small. In the case when hydrogen is replaced by deuterium, the ratio of the frequencies is approximately equal to:

$$\frac{\omega_1}{\omega_0} \approx \sqrt{\frac{m_1^{(0)}}{m_1^{(1)}}} = \frac{1}{\sqrt{2}} \qquad \text{(B4)}$$

The frequency is, therefore, red-shifted by a factor of $\sqrt{2}$. The real shift is smaller due to the fact that the second atom has finite mass (correction factor, up to linear terms, is $1 + \frac{1}{2m_2}$ and due to anharmonic effects.

APPENDIX C.

Frequency distribution for the system of oscillators

with nearest-neighbor interaction.

Let us consider a chain of identical harmonic oscillators with natural frequency ω_0, interacting with each other. We assume free boundary conditions. The interaction potential will be chosen as follows:

$$V_{ij} = \begin{cases} \alpha x_i x_j, \text{ if } |i-j| = 1 \\ 0, \quad \text{otherwise} \end{cases} \tag{C1}$$

Thus we consider nearest-neighbor interaction only. The total Hamiltonian for such a system is given by:

$$H = \sum_{i=1}^{N} \left(\frac{p_i^2}{2m} + \frac{m\omega_0^2 x_i^2}{2} \right) + \sum_{\langle ij \rangle} \alpha x_i x_j \tag{C2}$$

where symbol $\langle ij \rangle$ indicates the sum over nearest neighbors. Using Hamilton's equations of motion

$$\begin{cases} \dot{p}_i = -\dfrac{\partial H}{\partial x_i} \\ \dot{x}_i = \dfrac{\partial H}{\partial p_i} \end{cases} \tag{C3}$$

one can readily obtain:

$$\begin{cases} \dot{p}_i = -m\omega_0^2 x_i - \alpha x_{i-1} - \alpha x_{i+1} \\ \dot{x}_i = \dfrac{p_i}{m} \end{cases} \tag{C4}$$

Dot above the letter means differentiation with respect to time. From Eq. (C4) we can obtain N second-order coupled differential equations:

$$\begin{cases} m\ddot{x}_1 = -m\omega_0^2 x_1 - \alpha x_2 \\ m\ddot{x}_2 = -m\omega_0^2 x_2 - \alpha x_1 - \alpha x_3 \\ \ldots\ldots\ldots\ldots\ldots\ldots\ldots\ldots\ldots \\ m\ddot{x}_{N-1} = -m\omega_0^2 x_{N-1} - \alpha x_{N-2} - \alpha x_N \\ m\ddot{x}_N = -m\omega_0^2 x_N - \alpha x_{N-1} \end{cases} \tag{C5}$$

The standard way to solve this problem is to find all normal modes of the system. We assume the solution to have a form $x_i(t) = x_{i0} e^{-i\omega t}$ and, upon substitution in Eq. (C5), we get:

$$\begin{cases} \lambda x_1 + x_2 = 0 \\ \lambda x_2 + x_1 + x_3 = 0 \\ \ldots\ldots\ldots\ldots\ldots\ldots \\ \lambda x_{N-1} + x_N + x_{N-2} = 0 \\ \lambda x_N + x_{N-1} = 0 \end{cases} \tag{C6}$$

Here $\lambda = \dfrac{m(\omega_0^2 - \omega^2)}{\alpha}$. System (C6) has nontrivial solution if its determinant is zero. Therefore we obtain equation for λ:

$$\mathrm{Det}(\Lambda_N) = 0 \tag{C7}$$

where

$$\Lambda_N = \begin{bmatrix} \lambda & 1 & 0 & \cdot & \cdot & \cdot & 0 \\ 1 & \lambda & 1 & 0 & \cdot & \cdot & 0 \\ 0 & 1 & \lambda & 1 & 0 & \cdot & 0 \\ \cdot & \cdot & \cdot & \cdot & \cdot & \cdot & \cdot \\ 0 & \cdot & 0 & 1 & \lambda & 1 & 0 \\ 0 & \cdot & \cdot & 0 & 1 & \lambda & 1 \\ 0 & \cdot & \cdot & \cdot & 0 & 1 & \lambda \end{bmatrix} \tag{C8}$$

This determinant can be expanded over its first row (or column) as follows:

$$\mathrm{Det}(\Lambda_N) = \lambda \mathrm{Det}(\Lambda_{N-1}) - \mathrm{Det}(B_{N-1}) \tag{C9}$$

B_{N-1} is the following matrix:

$$B_{N-1} = \begin{bmatrix} 1 & 1 & 0 & . & . & . & 0 \\ 0 & \lambda & 1 & 0 & . & . & 0 \\ 0 & 1 & \lambda & 1 & 0 & . & 0 \\ . & . & . & . & . & . & . \\ 0 & . & 0 & 1 & \lambda & 1 & 0 \\ 0 & . & . & 0 & 1 & \lambda & 1 \\ 0 & . & . & . & 0 & 1 & \lambda \end{bmatrix} \tag{C10}$$

It is easy seen that determinant of B_{N-1} is equal to determinant of Λ_{N-2}. Thus we obtained the recurrency relation onto determinant of Λ_N:

$$\mathrm{Det}(\Lambda_N) = \lambda \mathrm{Det}(\Lambda_{N-1}) - \mathrm{Det}(\Lambda_{N-2}) \tag{C11}$$

The Eq. (C11) is satisfied by the Chebyshev polynomials of the second kind $U_N\left(\frac{\lambda}{2}\right)$. Therefore characteristic frequencies of the chain of N identical harmonic oscillators are given by roots of the appropriate Chebyshev polynomial.

$$U_N\left(\frac{\lambda}{2}\right) = 0 \tag{C12}$$

It is well known fact that these polynomials have simple real roots, lying in the interval $[-1;1]$. Thus our system has N distinct frequencies, ranging from $\sqrt{\omega_0^2 - \frac{2\alpha}{m}}$ to $\sqrt{\omega_0^2 + \frac{2\alpha}{m}}$. In fact, there is a short analytical form for frequencies of the normal modes of the system. Chebyshev polynomial U_N can be represented as follows:

$$U_N(\cos\theta) = \frac{\sin[(N+1)\theta]}{\sin\theta} \qquad \text{(C13)}$$

It is zero when the numerator is zero and denominator is not. One can easily obtain:

$$\theta_k = \frac{\pi k}{N+1}, k = 1...N \qquad \text{(C14)}$$

It follows from Eq. (C14) that

$$\lambda_k = 2\cos\left(\frac{\pi k}{N+1}\right) \qquad \text{(C15)}$$

Finally, for characteristic frequencies of the system we have:

$$\omega_k = \sqrt{\omega_0^2 - \frac{2\alpha}{m}\cos\left(\frac{\pi k}{N+1}\right)} \qquad \text{(C16)}$$

In the case of weak coupling the width of distribution of frequencies is of the order of $2\alpha/m\omega_0^2$.

If the coupling α is such that $2\alpha/m = \omega_0^2$, Eq. (C16) becomes:

$$\omega_k = \sqrt{2}\omega_0 \sin\left(\frac{\pi k}{2(N+1)}\right) \quad , \qquad \text{(C17)}$$

analogously to the dispersion relation for the phonons in crystal.

Appendix D.

AFM images of thin film of p-NTP.

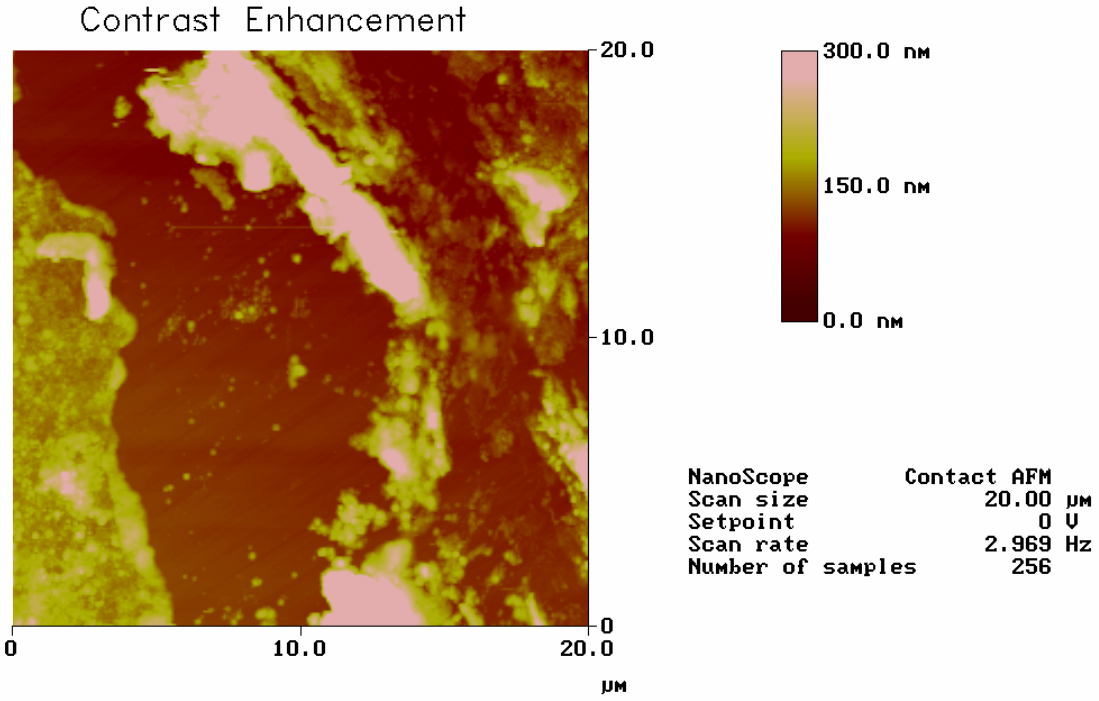

Figure 38. AFM image of p-NTP thin film.

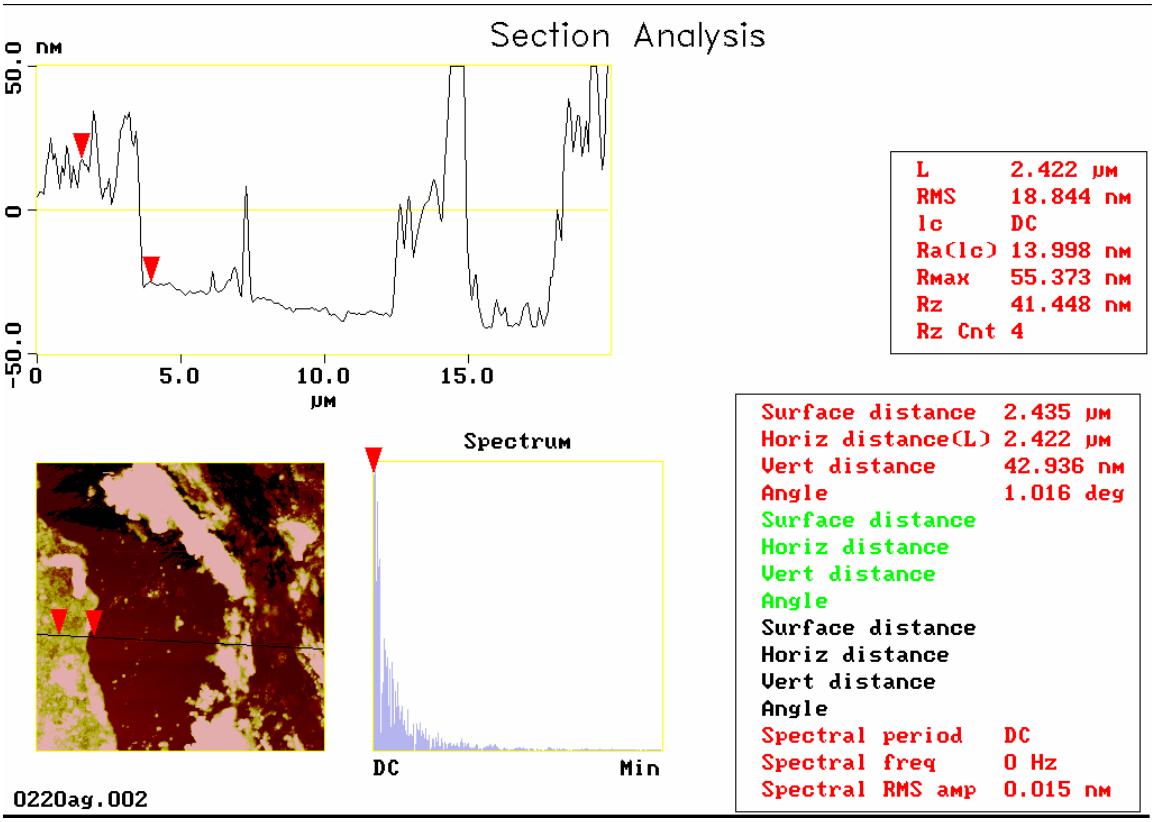

Figure 39. Section analysis of p-NTP thin film.

References:

[1]E. Schroedinger, Ann. D. Physik **79** 486 (1926).

[2] D. R. Hartree, Proc. Camb. Phil. Soc. **24** 89 (1928).

[3] V. Fock, Z. Phys. **61** 126 and *ibid* **62** 795 (1930).

[4] L. D. Landau and E. M. Lifshits, Quantum mechanics, Nonrelativistic theory, Pergamon Press, Oxford (1965).

[5] P. Hohenberg and W. Kohn, Phys.Rev. B **136** 864-870 (1964).

[6] W. Kohn and L. J. Sham, Phys. Rev. A **140** 1133-1138 (1965).

[7] W. Kohn, Rev. Mod. Phys. **71** 1253-1266 (1999).

[8] D. M. Bishop, Group theory and chemistry, Dover Publications, Inc. New York, 1993.

[9] M. J. Frisch *et al.*, GAUSSIAN 98, Revision A.9, Gaussian, Inc., Pittsburgh, Pennsylvania, 1998.

[10] L. D. Landau and E. M. Lifshitz, Statistical Physics, Pergamon Press Ltd., London-Paris, 1958.

[11] K. Huang, Statistical Mechanics, John Wiley & Sons Inc., New York, 1987.

[12] L. S. Ornstein and F. Zernike, Proc. Acad. Sci. (Amst.) **17** 793-806 (1915).

[13] L. P. Kadanoff, W. Götze, D. Hamblen, R. Hecht, E. A. S. Lewis, V. V. Palciauskas, M. Rayl, J. Swift, D. Aspens, and J. Kane, Rev. Mod. Phys. **39** 395-431 (1967).

[14] S. Ma, J. Math. Phys. **15** 1866-1891 (1974).

[15] V. M. Agranovich and A. A. Maradudin, Incommensurate phases in dielectrics, Elsevier Science Publishers B. V., Amsterdam, 1986.

[16] S. Aubry, Solitons and Condensed Matter Physics, eds. A. R. Bishop and T. Schneider (Springer, Berlin) 264-277 (1978).

[17] V. L. Pokrovsky, J. Phys. (France) **42** 761-766 (1981).

[18] E. Allroth and H. Müller-Krumbhaar, Phys. Rev.A **47** 1575-1586 (1983).

[19] A. Yariv, Quantum Electronics, 3rd ed., Wiley&Sons, New York, 1989.

[20] N. G. Greenham and R. H. Friend, Solid State Physics **49** 1-149 (1995) and references therein.

[21] J. M. Shaw and P. F. Seider, IBM J. of Res. & Dev. **45** 3-9 (2001).

[22] R. Friend, J. Burroughes, and T. Shimoda, Phys. World June, 35-40 (1999).

[23] I. H. Campbell and D. L. Smith, Solid State Physics, **55**, 1-117 (2001) and references therein.

[24] Grem et al., Adv. Mater. **4** 36 (1992).

[25] D. Cremer, Tetrahedron, **44** 7427 (1988).

[26] I. Fischer-Hjalmars, Tetrahedron, **19** 1805 (1963).

[27] O. Bastiansen, Acta Chem. Scand. **3**, 408 (1949).

[28] G-P. Charbonneau and Y. Delugeard, Acta Cryst. B **33** 1586-1588 (1977).

[29] H. Cailleau, J. L. Baudour, and C. M. E. Zeyen, Acta Cryst. B **35** 426-432 (1979).

[30] J. L. Baudour, Acta Cryst. B **47** 935-949 (1991).

[31] P. Launois, F. Moussa, M. H. Lemée-Cailleau, and H. Cailleau, Phys. Rev. B **40** 5042-5055 (1989).

[32] C. Ecolivet, M. Sanquer, J. Pellegrin, and J. DeWitte, J. Chem. Phys. **78** 6317-6324 (1983).

[33] G.-P. Charbonneau and Y. Delugeard, Acta Cryst. **B**33, 1586-1588 (1977).

[34] S. B. Liu and M. S. Conradi, Phys. Rev. Lett. **54** 1287 (1985).

[35] A. Veron, J. Emery, and F. Lari-Guillet, J. Phys. France and Chem. of solids **56** 51 (1995).

[36] M. H. Lemée-Cailleau, A. Girard, H. Cailleau, and Y. Délugeard, Phys. Rev. B **45** 12682-12690 (1992).

[37] A. Veron, J. Emery, and M. Spiesser, J. de Physique I France **6** 277-286 (1996).

[38] H. Cailleau, J. L. Baudour, J. Meinnel, A. Dworkin, F. Moussa, and C. M. E. Zeyen, Faraday Disc. Chem. Soc. **6** 7-18 (1980).

[39] N. M. Plakida, A. V. Belushkin, I. Natkaniec, and T. Wasiutynski, Phys. Stat. Sol. **118** 129-133 (1983).

[40] T. Wasiutyński and H. Cailleau, J. Phys.: Condens. Matter **4** 6241-6252 (1992).

[41] C. Benkert, V. Heine, and E. H. Simmons, J. Phys. C.: Solid State Phys. **20** 3337-3354 (1987).

[42] A. Baranya and T. R. Welberry, Mol. Phys. **73** 1317-1334 (1991).

[43] D. E. Williams and S. R. Cox, Acta Cryst. B **40** 404 (1984).

[44] A. Göller and U. W. Grummt, Chem. Phys. Lett. **321** 399-405 (2000).

[45] P. Puschnig, C. Amdrosch-Draxl, G. Heimel, E. Zojer, R. Resel, G. Leising, M. Kriechbaum, and W. Graupner, Synth. Metals **116** 327-331 (2001).

[46] S. Arulmozhiraja and T. Fujii, J. Chem. Phys. **115** 10589-10594 (2001).

[47] J. L. Baudour, Y. Delugeard, and H. Cailleau, Acta Cryst. B **32** 150-154 (1975).

[48] S. Ramdas and J. M. Thomas, ??? 1251-1258 (1976).

[49] D. E. Williams, J. Chem. Phys. **45** 3770 (1966).

[50] J. O. Williams, Chem. Phys. Lett. **42** 171-173 (1976).

[51] A. Girard, H. Cailleau, Y. Marqueton, and C. Ecolivet, Chem. Phys. Lett. **54** 479-482 (1978).

[52] B. A. Bolton and P. N. Prasad, Chem. Phys. **35** 331-344 (1978).

[53] A. M. Amorim da Costa, N. Karger, A. M. Amado, and M. Becucci, Solid State Ionics **97** 115-121 (1997).

[54] C. Ecolivet, B. Toudic, and M. Sanquer, J. Chem. Phys. **81** 599 (1984).

[55] T. Gullion, M. S. Conradi, and A. Rigamonti, Phys. Rev. B **31** 4338 (1985).

[56] M. C. Chen, A. S. Cullick, R. E. Gerkin, and A. P. Lundstedt, Chem. Phys. **46** 423 (1980).

[57] A. Ghanem, L. Bokobza, C. Noel, and B. Marchon, J. Mol. Struct. **159** 47-63 (1987).

[58] I. Baraldi and G. Ponterini, J. Mol. Struct. **122** 287-298 (1985).

[59] F. Momicchioli, I. Baradi, and M. C. Bruni, Chem. Phys. **70** 161 (1982).

[60] M. Akiyama, Spectrochimica Acta **40A** 367-371 (1984).

[61] T. Kobayashi, Bull. Chem. Soc. Jpn. **56** 3224-3229 (1983).

[62] S. Hino, K. Seki, and H. Inokuchi, Chem. Phys. Lett. **36** 335 (1975).

[63] A. Girard, Y. Delugeard, and H. Cailleau, J. Physique **48** 1751-1759 (1987).

[64] M. Kato and Y. Taniguchi, J. Chem. Phys. **92** 887-890 (1990).

[65] B. J. Baer and E. L. Chronister, J. Chem. Phys. **99** 3137-3138 (1993).

[66] A. Girard, Y. Delugeard, L. Pichon, and B. Toudic, J. de Phys. I **2** 1833 (1992).

[67] A. W. Lawson and T. Y. Tang, Rev. Sci. Instrum. **21** 815 (1950).

[68] J. C. Jamieson, A. W. Lawson, and N. D. Nachtrieb, Rev. Sci. Instrum. **30** 1016 (1959).

[69] C. E. Weir, E. R. Lippincott, A. Van Valkenburg, and E. N. Bunting, J. Res. Natl. Bur. Stand., Sec A **63** 55 (1959).

[70] A. Jayaraman, Rev. Mod. Phys. **55** 65-108 (1983).

[71] G. J. Piermarini and S. Block, Rev. Sci. Instrum. **46** 973 (1975).

[72] W. A. Bassett, T. Takahashi, and P. W. Stook, Rev. Sci. Instrum. **38** 37 (1967).

[73] H. K. Mao, P. M. Bell, K. J. Dunn, R. M. Chrenko, and R. C. Devries, Rev. Sci. Instrum. **50** 1002 (1979).

[74] K. R. Hirsh and W. B. Holzapfel, Rev. Sci. Instrum. **52** 52 (1981).

[75] R. Merrill and W. A. Bassett, Rev. Sci. Instrum. **45** 290 (1974).

[76] A. Van Valkenburg, Conference Internationale Sur-les-Hautes Pressions, LeCreusot, Saone-et-Loire, France. (1965).

[77] R. A. Forman, G. J. Piermarini, J. D. Barnett, and S. Block, Science **176** 284 (1972).

[78] J. D. Barnett, S. Block, and G. J. Piermarini, Rev. Sci. Instrum. **44** 1 (1973).

[79] G. J. Piermarini, S. Block, J. D. Barnett, and R. A. Forman, J. Appl. Phys. **46** 2774 (1975).

[80] H. K. Mao, P. M. Bell, J. W. Shaner, and D. J. Steinberg, J. Appl. Phys. **49** 3276 (1978).

[81] G. Yu. Machavariani, M. P. Pasternak, G. R. Hearne, and G. Kh. Rozenberg, Rev. Sci. Instrum. **69** 1423 (1998).

[82] M. D. McCluskey, L. Hsu, L. Wang, and E. E. Haller, Phys. Rev. B **54** 8962 (1996).

[83] P. R. Griffiths and J. A. de Haseth, Fourier Transform Infrared Spectrometry, John Wiley&Sons Inc., New York, 1986.

[84] J. K. Kauppinen, D. J. Moffatt, D. G. Cameron, and H. H. Mantsch, Appl. Op. **20** 1866 (1981).

[85] J. W. Cooley and J. W. Tuckey, Math. Comp. **19** 297 (1965).

[86] L. Mertz, Infrared Phys. **7** 17 (1967).

[87] M. L. Forman, W. H. Steele, and G. A. Vanasse, J. Opt. Soc. Am. **56** 59 (1966).

[88] P. R. Griffiths, H. J. Sloane, and R. W. Hannah, Appl. Spectrosc. **31** 485 (1977).

[89] K. K. Zhuravlev and M. D. McCluskey, J. Chem. Phys. **117** 3748 (2002).

[90] Aldrich Chemical Co., Milwaukee, WI 53201.

[91] M. Rubi and G. Zerbi, J. Chem. Phys. **242**, 123 (1999).

[92] K. Furuya, H. Torii, Y. Furukawa, and M. Tasumi, J. Mol. Struct. **424**, 225 (1998).

[93] A. D. Becke, J. Chem. Phys. **98**, 5648 (1993).

[94] K. K. Zhuravlev and M. D. McCluskey, J. Chem. Phys. **120** 1841 (2004) .

[95] K. K. Zhuravlev and M. D. McCluskey, J. Chem. Phys. **114** 5465 (2001).

[96] J.-L. Braudour, Y. Delugeard, and P. Rivet, Acta Crystallogr. B**34**, 625 (1978).

[97] S. Guha, W. Graupner, R. Resel, M. Chandrasekhar, H. R. Chandrasekhar, R. Glaser, and G. Leising, Phys. Rev. Lett. **82**, 3625 (1999).

[98] A. Hartstein, J. R. Kirtley, and J. C. Tsang, Phys. Rev. Lett. **45**, 201 (1980).

[99] N. Matsuda, K. Yoshii, K. Ataka, M. Osawa, T. Matsue, and I. Uchida, Chem. Lett., 1385-1388 (1992).

[100] G. T. Merklin, L.-T. He, and P. R. Griffiths, Appl. Spectrosc. **53**, 1448 (1999).

[101] K. Bandyopadhyay, K. Vijayamohanan, M. Venkataramanan, and T. Pradeep, Langmuir **15**, 5314, (1999).

[102] T. Shimizu, H. Isono, M. Yasui, F. Iwasaki, and N. Kamigata, Org. Lett. **3**, 3639 (2001).

[103] T. Yoshidome and S. Kamata, Anal. Sci. **13**, 351 (1997).

[104] R. Kellner, B. Mizaikoff, M. Jakusch, H. D. Wanzenböck, and N. Weissnbacher, Appl. Specrosc. **51**, 495 (1997).

[105] T. Yoshidome, T. Inoue, and S. Kamata, Chem. Lett., 533-534 (1997).

[106] A. E. Bjerke, P. R. Griffiths, and W. Theiss, Anal. Chem. **71**, 1967 (1999).

[107] S. Sato and T. Suzuki, Appl. Spectrosc. **51**, 1170 (1997).

[108] M. Osawa, Topics Appl. Phys. **81**, 163 (2001) and references therein.

[109] J. P. Devlin and K. Consani, J. Phys. Chem. **85**, 2597 (1981).

[110] T. Wadayama, T. Sakurai, S. Ichikawa, and W. Suëtaka, Surf. Sci. Lett. **198**, L359 (1988).

[111] B. N. J. Persson and R. Ryberg, Phys. Rev. B **24**, 6954 (1981).

[112] G. C. Papavassiliou, Prog. Solid St. Chem. **12** 185 (1979).

[113] C. F. Eagen, Appl. Optics **20**, 3035 (1981).

[114] G. A. Niklasson and C. G. Granqvist, J. Appl. Phys. **55** 3382 (1984).

[115] A. Wokaun, Solid State Physics **38**, 223 (1984).

[116] J. I. Gersten and A. Nitzan, Surf. Sci. **158** 165 (1985).

[117] M. Osawa and K.-ichi Ataka, Surf. Sci. Lett. **262**, L118 (1992).

[118] S. Corni and J. Tomasi, Chem. Phys. Lett. **342**, 135 (2001).

[119] S. Corni and J. Tomasi, J. Chem .Phys. **116**, 1156 (2002).

[120] G. C. Schatz and R. P. Van Duyne, Handbook of Vibrational Spectroscopy, ed. J. M. Chalmers and P. R. Griffiths, John Wiley & Sons Ltd, Chichester, 2002.

[121] Y. Nishikawa, T. Nagasawa, K. Fujiwara, and M. Osawa, Vibr. Spectr. **6**, 43 (1993).

[122] J. C. M. Garnett, Philos. Trans. R. Soc. London **205** 237 (1906).

[123] D. A. G. Bruggeman, Ann. Phys. (Leipzig) **24**, 636 (1935).

[124] C. A. Murray and S. Bodoff, Phys. Rev. B **32**, 671 (1985).

[125] E. J. Zeman, K. T. Carron, G. C. Schaltz, and R. P. Van Duyne, J. Chem. Phys. **87**, 4189 (1987).

[126] W.-H. Yang, G. C. Schaltz, and R. P. Van Duyne, J. Chem. Phys. **103**, 869 (1995).

[127] W. A. Kraus and G. C. Schaltz, J. Chem. Phys. **79**, 6130 (1983).

[128] A. Liebsch and W. L. Schaich, Phys. Rev. B **52**, 14219 (1995).

[129] G.-Y. Liu and M. B. Salmeron, Langmuir, **10**, 367-370 (1994).

[130] K. Sasaki, Y. Koike, H. Azehara, H. Hokari, and M. Fujihira, Appl. Phys. A, **66**, S1275-S1277 (1998).

[131] I. Doudevski and D. K. Schwartz, Phys. Rev. B **60**, 14-17 (1999).

[132] F. Cunha, Q. Jin, N. J. Tao, and C. Z. Li, Surf. Sci. **389**, 19-28 (1997).

[133] W.-B. Cai, L.-J. Wan, H. Noda, Y. Hibino, K. Ataka, and M. Osawa, Langmuir **14**, 6992-6998 (1998).

[134] H. Noda, T. Minoha, L.-J. Wan, and M. Osawa, J. Electroanal. Chem. **481**, 62-68 (2000).

[135] L.-J. Wan, M. Terashima, H. Noda, and M. Osawa, J. Phys. Chem. B **104**, 3563-3569 (2000).

[136] P. Fenter, P. Eisenberger, and K. S. Liang, Phys. Rev. Lett. **70**, 2447-2450 (1993).

[137] P. Kimkes, A. de Jong, G. T. Oostergetel, A. J. Schouten, and G. Ghalla, Thin Solid Films **244**, 705-709 (1994).

[138] E. Scalas, G. Brezesinski, H. Möhwald, V. M. Kaganer, W. G. Bouwman, and K. Kjaer, Thin Solid Films **284-285**, 56-61 (1996).

[139] M. K. Durbin, A. Malik, A. G. Richter, C.-J. Yu, R. Eisenhower, and P. Dutta, Langmuir **14**, 899-903 (1998).

[140] J. M. Tour, L. Jones II, D. L. Pearson, J. J. S. Lamba, T. P. Burgin, G. M. Whitesides, D. L. Allara, A. M. Parikh, and S. V. Atre, J. Am. Chem. Soc. **117**, 9529-9534 (1995).

[141] R. G. Nuzzo, L. H. Dubois, and D. L. Allara, J. Am. Chem. Soc. **112,** 558-569 (1990).

[142] M. S. Yeganeh, S. M. Dougal, R. S. Polizzotti, and P. Rabinowitz, Phys. Rev. Lett. **74**, 1811-1814 (1995).

[143] J.-G. Yoo, H. Hoshi, T. Sakai, B. Park, K. Ishikawa, H. Takezoe, and Y. S. Lee, J. Appl. Phys. **84**, 4079-4086 (1998).

[144] Y. Rao, Yi-song Tao, and H.-fei Wang, J. Chem. Phys. **119**, 5226-5236 (2003).

[145] G. A. Overbeck, D. Hönig, and D. Möbius, Langmuir **9**, 555-560 (1993).

[146] E. Sabatani, J. Cohen-Boulakia, M. Bruening, and I. Rubinstein, Langmuir **9**, 2974-2981 (1993).

[147] L. X. Zheng, B. C. Hess, R. E. Benner, Z. V. Vardeny, and G. L. Baker, Phys. Rev. B **47**, 3070-3077 (1993).

[148] R. G. Nuzzo, E. M. Korenic, and L. H. Dubois, J. Chem. Phys. **93**, 767-773 (1990).

[149] A. Gericke, D. J. Moore, R. K. Erukulla, R. Bittman, and R. Mendelsohn, J. Mol. Struct. **379**, 227-239 (1996).

[150] G. T. Merklin, L.-T. He, and P. R. Griffiths, Appl. Spectrosc. **53**, 1448-1453 (1999).

[151] D. L. Elmore and R. A. Dluhy, Appl. Spectrosc. **54**, 956-962 (2000).

[152] J. Hautman and M. L. Klein, J. Chem. Phys. **93**, 7483-7492 (1990).

[153] Z. Zhang, T. L. Beck, J. T. Young, and F. J. Boerio, Langmuir **12**, 1227-1234 (1996).

[154] J. Gao, W. D. Luedtke, and U. Landman, J. Chem. Phys. **106**, 4309-4318 (1997).

[155] R. Bhatia and B. J. Garrison, Langmuir **13**, 765-769 (1997).

[156] W. Selke Interfaces, Wetting Phenomena, Incommensurate Phases in *Topics in Applied Physics,* v.**71**, pp. 329-354 (1992).